Assessment of Using a Tesla Expander to Harvest Waste Heat from a Photovoltaic Panel for Residential Applications

by

Roozbeh Yousefnejad

B.A.Sc., University of Tehran, 2015

A THESIS SUBMITTED IN PARTIAL FULFILLMENT OF

THE REQUIREMENTS FOR THE DEGREE OF

MASTER OF APPLIED SCIENCE

in

THE FACULTY OF GRADUATE AND POSTDOCTORAL STUDIES

(Mechanical Engineering)

THE UNIVERSITY OF BRITISH COLUMBIA

(Vancouver)

August 2018

© Roozbeh Yousefnejad, 2018

The following individuals certify that they have read, and recommend to the Faculty of Graduate and Postdoctoral Studies for acceptance, a thesis/dissertation entitled:

Assessment of Using a Tesla Expander to Harvest Waste Heat from a Photovoltaic Panel for Residential Applications

submitted by Roozbeh Yousefnejad in partial fulfillment of the requirements for

the degree of Master of Applied Science

in Mechanical Engineering

Examining Committee:

Mu Chiao, Mechanical Engineering
Supervisor

Patrick Kirchen, Mechanical Engineering
Supervisory Committee Member

Dana Grecov, Mechanical Engineering
Supervisory Committee Member

Nima Atabaki, Mechanical Engineering
Additional Examiner

Additional Supervisory Committee Members:

Supervisory Committee Member

Supervisory Committee Member

Abstract

Solar energy is an abundant source of energy for generating electricity. The main challenge is that the solar photovoltaic (PV) panels are typically used in regions where solar radiation is high; consequently, the temperature of the panels will increase, and the efficiency of the panel will decrease. Water cooling systems are typical methods of cooling, and the resulting hot water can be used for space heating or other purposes. In regions that have high solar radiation; however, the demand for hot water is not high.

In this research, we investigated combinations of PV panel, an expander with a Rankin cycle, and a new working fluid to generate extra electrical power for residential applications. To achieve the goal, different working fluids were analyzed, and R-245-fa was found to be the ideal fluid for this purpose. To design the cooling system, a new algorithm was developed to find the optimal number, spacing, and diameter of the cooling tubes. The accuracy of the new model was determined by a CFD simulation, and for possible future industrial uses, a user-friendly application was developed using COMSOL® Multiphysics.

A Tesla expander was built and tested, and the torque was measured experimentally. The results were compared to typical methods of modeling the turbine to determine the accuracy of each model. Finally, for real data for a day in Egypt, the system was analyzed, and the cooling cycle was shown to yield an average improvement of 12% in terms of generated power.

Lay Summary

Solar energy is an abundant source of energy that can be used vastly to generate electricity. According to International Energy Agency (IEA) onshore wind turbine and solar photovoltaic panels are expected to provide most of the renewable energy capacity in the next five years.

The main challenge in using photovoltaic panels is that they tend to operate at higher temperatures, which decreases the efficiency of the panel. Consequently, different methods are being tested for their ability to cool the panel. Water cooling is a typical method where cold water absorbs heat from the panel. As a result, the efficiency of the system is kept constant and hot water is the inadvertent product. In this project, our aim is to assess the use of alternative working fluids to cool the panel and conserve what might otherwise be a precious source of water while generating extra power in a separate power cycle.

Preface

The research presented in this thesis was conducted by the author, Roozbeh Yousefnejad, under the guidance of Dr. Mu Chiao (supervisor) and Dr. Nima Atabaki (co-supervisor). The algorithm discussed in Chapter 4 was developed by the author. In addition, all of the CFD simulations were done with COMSOL® Multiphysics, which was provided by CMC.

The Tesla turbine used in the experiments described in Chapter 5 was completely built in UBC's MEMS Laboratory by the author and Minghua Wu. This chapter of the thesis has been submitted for publication as: **R. Yousefnejad**, M. Wu, N. Atabaki, M. Chiao, "*Assessment of a New 2D Model to Simulate Tesla Turbines for Low-Flow Rate Systems*"; submitted July 2018.

Moreover, part of Chapter 5 will be presented at the 12th European Fluid Mechanic Conference (EFMC12), in Vienna on September 9-13, 2018: **R. Yousefnejad**, M. Wu, N. Atabaki, M. Chiao, "*Comparison of different modelling methods of a Tesla turbine for low-grade energy applications*", page number: 266.

Table of Contents

Abstract iii

Lay Summary iv

Preface v

Table of Contents vi

List of Tables x

List of Figures xii

List of Symbols xvii

Acknowledgements xxi

Dedication xxii

Chapter 1: Introduction 1

1.1 Photovoltaic panel 3

1.2 Challenges in using PV cells 4

1.3 Cooling techniques 6

1.3.1 Heat pipe cooling 7

1.3.2 Liquid immersion cooling 7

1.3.3 Micro-channels 9

1.3.4 Heat exchanger 10

1.4 Purposes and objectives 12

Chapter 2: Thermodynamic Analysis of the Cycle 13

2.1 Rankine Cycle 13

2.1.1 Organic Rankine Cycle (ORC) 14

2.1.2 Cycle Calculation 15

2.2 Proper Fluid Criteria 16

2.2.1 Critical Temperature and Pressure 17

2.2.2 Environmental Effect 17

2.2.3 Stability and Compatibility with materials 17

2.2.4 Flow Rate 18

Chapter 3: Choosing Proper Fluids for the Solar Cycle 19

3.1 First and second law of thermodynamic analysis 23

Chapter 4: Modeling the Solar Panel Cooling System 25

4.1 Analytical Solution 25

4.2 CFD Simulation 46

4.3 Results 48

4.3.1 Analytical Solution 48

4.3.2 CFD Simulation 51

4.3.3 Analyzing the Performance of the System for Real Data 55

Chapter 5: Solar Cycle Expander (Turbine) 63

5.1 Tesla turbine 65

5.1.1 Literature review 65

5.1.2 Objectives 71

5.2 Mathematical modeling of Tesla turbine 71

5.2.1 Modified Carey's method 72

5.2.2 Rice's method 76

5.3 CFD Simulation 77

5.4 Experimental setup 80

5.5 Torque measurement 84

5.6 Results 86

5.7 Output power of the cycle 92

Chapter 6: Conclusion and Future Work 95

6.1 Limitations and Future Directions 97

Bibliography 99

Appendices 106

Appendix A (Uncertainty Analysis for Torque Measurements) 106

Appendix B (The COMSOL® application) 108

B.1 Control Options.....109

B.2 Inputs and Results.....110

B.3 Graphics 110

Appendix C (Working fluids properties in the cycle).....114

List of Tables

Table 3.1. Thermal properties of the suggested working fluids.....19

Table 3.2. Exergy destruction in each process of the cycle.....24

Table 4.1. Thermal properties of the different layers of the photovoltaic cells [27] 32

Table 4.2. Relevant settings used in COMSOL 5.2 48

Table 4.3. Thermal properties of the working fluid 49

Table 4.4. Minimum tube length (in meter) for different design parameters (m =0.00397 kg/s).....51

Table 4.5. Mesh independency analysis for the CFD model 53

Table 4.6. Total length of the tube for the assumed working parameters (m =0.00397 kg/s).....54

Table 4.7. Total length of the tube for the modified mass flow rate (m =0.003 kg/s) ...55

Table 4.8. Final value for PV temperature and heat loss coefficient for the specific ambient temperature and solar radiation 58

Table 4.9. Minimum length of the tube which is required to run the Rankin cycle 61

Table 5.1 Summary of relevant previous work on the Tesla turbine 66

Table 5.2. List of 2D axisymmetric models and their specifications. To show different models on one figure, we will name each model in the form of "INLET-OUTLET- HAS EXHAUST HOLE OR NOT (YES/NO)- SIZE OF EXHAUST HOLE.".....79

Table 5.3. Specification of the turbine.....80

Table 5.4. Moment of inertia for all rotating components.....85

Table 5.5. Results for the torque for 2.2 SCFM 90

Table 5.6. Results for the torque for 2.4 SCFM 91

Table 5.7. Properties of the working fluid and turbine for the power analysis of the cycle 93

List of Figures

Figure 1.1. Global solar radiation distribution [3] 2

Figure 1.2. Variation in efficiency by changing the cell temperature [10] 5

Figure 1.3. View of the optical concentrator for liquid immersion cooling [17] 8

Figure 1.4. Process flow for (a) copper heat spreader, (b) silicon substrate, and (c) micro-channel heat sink. [22] 9

Figure 2.1. Schematic view of the Rankin cycle and its main components 13

Figure 2.2. T-s diagram for a simple Rankine cycle [30] 14

Figure 2.3. Different isentropic expansions for (a) wet fluids (b) dry fluids and (c) isentropic fluids [31] 15

Figure 3.1. Energy needed to run the cycle with different working fluids and different working conditions 21

Figure 3.2. The mass flow rate for the working points that satisfy the constraints 22

Figure 4.1. Front view of the photovoltaic panel with glass cover and cooling tubes 26

Figure 4.2. Thermal resistance diagram of the system 27

Figure 4.3. Flow diagram for calculating the total heat loss coefficient 31

Figure 4.4. View of photovoltaic panel and the cooling tubes 32

Figure 4.5. Different mechanism for heat transfer to the working fluid 34

Figure 4.6. Entrance and fully developed region for the hydraulic and thermal boundary layers [36] 36

Figure 4.7. The Nusselt number variation for the entrance length and fully developed region [36] 39

Figure 4.8. Energy balance for the fluid element in the tube 40

Figure 4.9. The procedure to find the average heat transfer coefficient in the pipes 41

Figure 4.10. Algorithm to find the mean temperature of the panel 44

Figure 4.11. Complete iteration process to find PV and cover temperature and the length of the tube 45

Figure 4.12. 3D geometry of the panel with the cooling tube in COMSOL 46

Figure 4.13. Thermal boundary conditions for the front surface of the geometry 47

Figure 4.14. Proper boundary conditions for the fluid flow 47

Figure 4.15. Variation of the tube length with tube diameter and distance 50

Figure 4.16. Temperature profile of the insulation and the working fluid 52

Figure 4.17. Temperature profile of the outlet 52

Figure 4.18. Variation in solar radiation with time [39] 56

Figure 4.19. Variation in ambient temperature with time [39] 57

Figure 4.20. Efficiency graph for the PV panel with and without cooling. Top surface: with cooling tube; Bottom surface: without cooling 59

Figure 4.21. One-day power savings for one panel using a cooling tube.....60

Figure 4.22. Compression of the outlet temperature of the tube with the designed temperature.....62

Figure 5.1. working conditions for different types of turbine [40].....64

Figure 5.2. Schematic of the Tesla turbine and fluid flow between the disks.....65

Figure 5.3. Schematic view of the turbine with the defined axis direction 72

Figure 5.4. A 3D model showing inlet nozzle.....78

Figure 5.5. 2D simulation geometry 79

Figure 5.6. Schematic view of the experimental set up.....81

Figure 5.7. Different parts of the experimental set-up: (a) Close view of the encoder, couplings and ball bearing (b) Close picture of the housing shows the exhaust holes (c) Housing and connecting bolts (d) Picture of air compressor water filter.....82

Figure 5.8. Different parts of the experimental set-up: (a) Compressor (b) Arduino to read data from encoder (c) Flowmeter 83

Figure 5.9. Rotational speed of the rotor for 2.2 SCFM flow rate. 86

Figure 5.10. Rotational speed of the rotor for 2.4 SCFM flow rate 86

Figure 5.11. Zoomed view of the acceleration part of rotational speed graph for 2.2 SCFM....87

Figure 5.12. Zoomed view of the acceleration part of rotational speed graph for 2.4 SCFM....87

Figure 5.13. Torque-speed graph for 2.2 SCFM flow rate....88

Figure 5.14. Torque-speed graph with uncertainty bar for the 4th test with 2.2 SCFM 88

Figure 5.15. Torque-speed graph for 2.4 SCFM flow rate....89

Figure 5.16. Torque-speed graph with uncertainty bar for the 2nd test with 2.4 SCFM89

Figure 5.17. The streamline contour for the 2D simulation for AC-Y-10 model with 2.2 SCFM flow rate....92

Figure 5.18. Variation of the force acting on one disk as a function of radius....93

Figure 6.1. Comparison of the improvements in power generation in one panel from different methods....96

Figure B.1. View of the software interface....108

Figure B.2. View of the control option bar of the software....109

Figure B.3. View of the inputs and results sections of the software....110

Figure B.4. Geometry tab in the graphics section of the software....111

Figure B.5. Temperature tab in the graphics section of the software....112

Figure B.6. Slice temperature tab in the graphics section of the software.....112

Figure B.7. Surface temperature tab in the graphics section of the software 113

List of Symbols

α	Thermal diffusivity	[m^2/s]
β	Panel tilt angle	[rad]
β_{ref}	Reference constant for PV efficiency	[1/K]
β'	Volumetric coefficient of expansion	[1/K]
δ	Thickness of PV panel	[m]
ε_g	Glass emissivity	[-]
ε_p	Plate emissivity	[-]
ε_c	Cover emissivity	[-]
η_{ref}	Reference efficiency for PV	[-]
μ_f	Fluid dynamic viscosity	[Pa.s]
ν	Kinematic viscosity	[m^2/s]
σ	Stefan-Boltzmann Constant	[$W.m^{-2}.K^{-4}$]
ρ	Density	[kg/m^3]
τ_w	Wall shear stress	[Pa]
$\widetilde{v_r}$	Relative radial velocity	[m/s]
v_r	Fluid velocity in radial direction	[m/s]
v_θ	Fluid velocity in tangential direction	[m/s]
Ω	Rotational speed	[rad/s]
A_c	Surface area of the collector	[m^2]
A_w	Wetted area	[m^2]
b	Distance between disks	[m]

C_p	Heat capacity	[J.kg^{-1}.K^{-1}]
D	Tube outer diameter	[m]
D_h	Hydraulic diameter	[m]
D_i	Tube inner Diameter	[m]
$E_{electrical}$	Electricity generated by PV panel	[W/m^2]
f	Friction factor	[-]
f_r	Volumetric radial force	[N/m^3]
f_θ	Volumetric tangential force	[N/m^3]
g	Gravitational acceleration	[m/s^2]
Gz_D	Graetz number	[-]
$\mathbf{h}$	Enthalpy	[kJ/kg]
h	Convective heat transfer coefficient	[W.m^{-2}.K^{-1}]
h_{fi}	Convective heat transfer coefficient for fluid in the tube	[W.m^{-2}.K^{-1}]
h_w	Convective heat transfer for wind	[W.m^{-2}.K^{-1}]
$h_{c,c-a}$	Convective heat transfer coefficient between cover and ambient	[W.m^{-2}.K^{-1}]
$h_{c,p-c}$	Convective heat transfer coefficient between plate and cover	[W.m^{-2}.K^{-1}]
$h_{r,c-a}$	Radiative heat transfer coefficient between cover and ambient	[W.m^{-2}.K^{-1}]
$h_{r,p-c}$	Radiative heat transfer coefficient between plate and cover	[W.m^{-2}.K^{-1}]
I	Moment of inertia	[kg.m^2]
k	Thermal conductivity	[W.m^{-1}.K^{-1}]
L	Latent heat	[kJ/kg]
L_g	Glass cover distance	[m]

$l_{entrance-hydrolic}$	Hydraulic entrance length	[m]
$l_{entrance-thermal}$	Thermal entrance length	[m]
$\dot{m}$	Mass flowrate	[kg/s]
$\dot{m}_{tube}$	Mass flow rate for one tube	[kg/s]
N	Number of tube	[-]
Nu	Nusselt number	[-]
P	Pressure	[Pa]
P_{atm}	Ambient pressure	[Pa]
P_c	Critical pressure	[Pa]
Pr	Prandtl number	[-]
q_e	Electron charge	[C]
q''	Net available energy for heating	[W/m^2]
q_u	Useful energy per m^2	[W/m^2]
q_{edge}	Heat loss from edge of panel	[W/m^2]
Q	Volumetric flowrate	[m^3/s]
Q_c	Rejected heat	[W]
Q_h	Absorbed heat	[W]
Q_u	Useful energy	[W]
r	Radius	[m]
Re_D	Reynolds number	[-]
S	Solar radiation	[W/m^2]
T	Temperature	[K]
$\mathbf{T}$	Torque	[N.m]
T_a	Ambient temperature	[K]

T_b	Back Temperature	[K]
T_c	Critical temperature	[K]
T_p	Plate temperature	[K]
T_{pm}	Plate mean temperature	[K]
T_{bo}	Bonding Temperature	[K]
T_{ref}	Reference temperature for PV efficiency	[K]
T_{fi}	Fluid temperature at inlet	[K]
T_{fo}	Fluid temperature at outlet	[K]
T_f	Fluid temperature	[K]
$\mathbf{U}$	Uncertainty	[-]
U_l	Top surface lost coefficient of panel	[$W.m^{-2}.K^{-1}$]
U_t	Total lost coefficient of panel	[$W.m^{-2}.K^{-1}$]
V_f	Volume of the fluid	[m^3]
V_{OC}	Open circuit voltage	[V]
$\dot{W}$	Power	[W]
W	Center to center distance of the tubes	[m]

Acknowledgements

I would like to express my sincere appreciation to my advisor, Dr. Mu Chiao, for his support during my master's program. I have been extremely lucky to have a supervisor who cared so much about my research and helped me think more about my professional career. Also, I must thank my co-supervisor, Dr. Atabaki, for enlarging my vision of the project and helping me to finish this project.

I will forever be grateful to my friend Amin Arefi for his great suggestions and for his patience with my endless questions. I should also thank Munghua Wu for his great help with Chapter 5 of this thesis. Thank you so much to my friend, Ali Moallemi, for his fantastic support during crucial time of writing this thesis.

Family is not always blood; it is the people who support us by their heart. I want to say thank you to Homa, Behnam, Anoosh, Amir, Armina, Emad, and Mona who are like my family. they were definitely an inspiration for me, and my energy was driven by their help.

Finally, Special thanks are owed to my parents and my sister, whose have supported me throughout my years of education, both morally and financially.

Dedication

To my beloved sister, Niloofar. I am truly thankful to have you in my life.

Chapter 1: Introduction

Energy is at the heart of economic improvement, and it is an unavoidable prerequisite for technological advancement. In the last decade, with the rapid growth in world population, the need for more sustainable energy sources has increased dramatically. The rapid growth in energy demands has caused governments to not only rely on fossil fuels but to seek other sustainable energy sources. Among the various energy resources, renewable energy is proving to be a promising source for the future. Despite the large amount of research into sustainable energy in recent decades, further developments are necessary to enable large-scale production of low-cost renewable energy.

Solar energy is one of the possible sources of energy for industrial and residential applications. The large amount of solar energy that is available makes it a highly appealing source of electricity. One of the most important advantages of solar energy is that it is clean. Currently, the global emission from coal-based thermal power plants is 532 gCO_2/kWh [1] while the emission from solar photovoltaic panels is about 72 gCO_2/kWh, making solar energy a possible option for curtailing global emissions. Moreover, solar energy is the most abundant source of energy, which is available almost everywhere on earth. The sun emits energy at the rate of 3.8×10^{23} KW, and approximately 1.8×10^{14} kW is absorbed by the earth [2]. Figure 1.1 shows the distribution of solar radiation across the world:

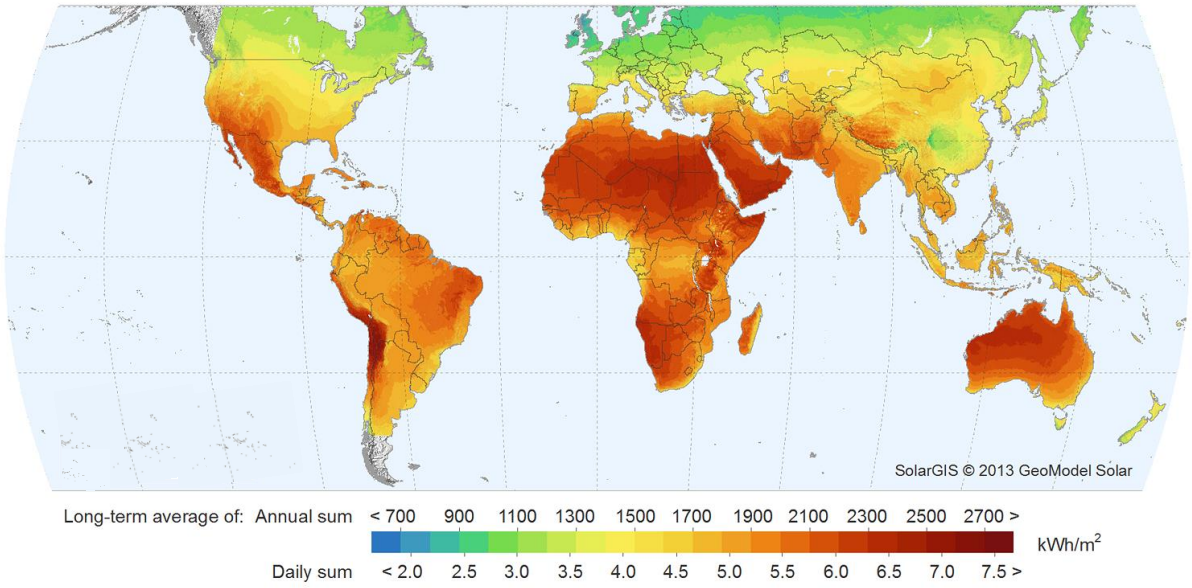

Figure 1.1. Global solar radiation distribution [3]

One of the possible applications for solar energy is for space or water heating. In countries with high levels of panel installation, solar thermal systems can be very cost-competitive compared to fossil fuel alternatives. Elsewhere, large installations can provide economies of scale. The world's largest solar thermal plant entered operation in Silkeborg, Denmark at the end of 2016, where it is expected to produce 80,000 MWh for the local heating network [4].

According to the International Energy Agency (IEA) report, onshore wind turbine and solar photovoltaic (PV) panels are expected to provide most of renewable energy capacity in the next five years. Moreover, by decreasing solar PV prices to below 100 USD/kW.hr in most countries in the next five years, the market is expected to become more motivated to use this technology. With the expected cost reduction and policies, electricity generation from solar PV is forecast to triple in the next decade. Thus, the future for renewable energy

appears to be determined by solar panel technologies, especially PV panels, so that more research on PV panels seems to be inevitable [4].

1.1 Photovoltaic panel

PV cells are devices that convert solar radiation to electricity. They can be connected either in series or in parallel to form photovoltaic generator systems. The technology used to produce these modules can vary for different companies, with some of the most common photovoltaic cells listed below:

- Crystalline PV modules

One of the best choices for industrial grid connection applications are the crystalline-based silicon PV panels. Their maximum efficiency is reported to be 20% [5]. In crystalline silicon, each atom has a predefined crystal position in the structure. The highest efficiency of these panels can be achieved by using mono-crystalline PV modules; however, due to the expensive manufacturing process, such modules are not yet economically feasible.

Two different types of crystalline PV modules are currently used for different applications. The first type is the opaque module, which usually has a white tedlar[1] at the back surface. The second type is the transparent module, which has a glass cover on top of the cells [6].

[1] Polyvinyl fluoride (PVF), a thermoplastic fluoropolymer material has high weather resistance and inherent strength, low permeability to moisture, vapor, and oil, and can be used in a wide temperature range.

- Thin-film PV modules

Thin-film modules are produced from amorphous silicon. The technology has become more popular since the process is cheaper than that for producing mono-crystalline silicon and it takes place at a lower temperature, which results in reducing the embodied energy[2] per watt-peak. In addition, thin layers of PV modules are flexible and can be used on different kinds of flexible surfaces. Nevertheless, these systems have a problem in that the amorphous silicon provides an efficiency of only 6-7%, which makes the technology unsuitable for some applications.

1.2 Challenges in using PV cells

One of the most important factors affecting the performance of a PV cell is temperature [7]. PV cell efficiency drops as a function of temperature, which makes thermal management of the solar energy system crucial for maintaining a higher efficiency. Typically, the efficiency of PV cells is around 15% [8] at room temperature. Part of the solar energy will be reflected from the panel and some will be absorbed by the panel as a heat, increasing the temperature of the cells.

Higher temperatures will decrease the open circuit voltage in the PV cells and decrease the efficiency of the panel, because of the electron energy gap in semiconductors. The electricity that is generated by the electrons is the difference between the energy states of electrons at rest and in excited states. By increasing the temperature, the energy state of the electrons will be increased, and the band gap of the semiconductors will be decreased. In such

[2] Embodied energy is the sum of all energy required to produce any good or service.

conditions, less energy is needed to break the bond, which results in less electrical energy being generated. This behavior can also be illustrated by equations. For semiconductors, the open circuit voltage can be calculated from the following: [9]

$$V_{oc} = \frac{kT}{q}\left(\ln I_{SC} - \ln B' - \gamma lnT + \frac{q_e V_{G0}}{kT}\right) \qquad 1.1$$

where B' is a temperature independent constant, γ is a constant number equal to 3, k is a constant number, q is the electron charge, V_{G0} is equal to E_{G0}/q_e, where E_{G0} is the band gap linearly extrapolated to absolute zero, T is temperature, and I_{SC} is the short circuit current. Assuming that I_{SC} is not a function of temperature, we can find the sensitivity of the open circuit voltage to temperature:

$$\frac{dV_{oc}}{dT} = \frac{V_{oc} - V_{G0}}{T} - \frac{\gamma k}{q_e} \qquad 1.2$$

For silicon, the sensitivity of the open circuit voltage to temperature is reported to be -2.2 mV/°C This temperature dependency of the efficiency of PV panels was experimentally investigated by Tiwari and Dubey [10] (Figure 1.2).

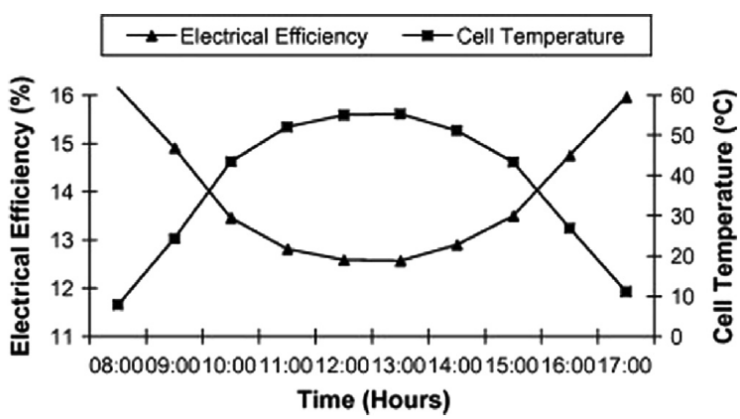

Figure 1.2. Variation in efficiency by changing the cell temperature [10]

In addition to the high temperature effects, a non-uniform temperature distribution or illumination can cause hot spots on PV panels. This can be especially significant when the cells are connected in series as the cell that gives the smallest output will limit the current. This situation is known as the "*current matching problem*" [11]. Since cell efficiency decreases with increasing temperature, the cell at the highest temperature will limit the efficiency of the group. The problem can be avoided by using a bypass diode [12]. An uneven temperature distribution will also impose thermal stresses on the panel, which can cause thermal fatigue due to thermal cycles, and decrease the reliability of the system [11].

Baig et al. [13] reviewed the causes and effects of the non-uniform illumination on concentrator solar cells for both single and multi-junction solar cells. Concentrator geometry, design, and manufacturing methods are key factors that can cause non-uniformity and ultimately increase the cost of using solar cells. In a review by Royne et al. [11] of concentrated photovoltaic cells, the heat flux was found to be higher at the center, requiring cooling in this part. With regards to densely packed cells at high concentrations, the authors also indicated that an active cooling system is necessary.

1.3 Cooling techniques

For the reasons mentioned above, cooling systems are necessary to cool PV panels. Such cooling processes must keep the temperature constant with minimal non-uniformity of cells [11]. In a review by Bahaidarah et al. [8], different methods for cooling panels were described, including jet implementation, heat exchangers, heat pipes, liquid immersion cooling, micro-channels, and phase change materials. Some of the most common methods are explained below:

1.3.1 Heat pipe cooling

Cooling the electrical system is a topic of interest to many researchers. Among the more common methods for rejecting heat, using heat pipes was promising, because of the high-performance heat transfer. In these systems, the heat is absorbed from hot surfaces and then transferred to the low heat flux sink. The behavior of heat pipes has been investigated numerically and experimentally in the literature [13] [14]. In a report [8] reviewing heat pipes, they were found to dispel heat at a rate of 110 W/cm^2 without any heat transfer restrictions. Akbarzadeh and Wadowski [16] investigated the idea of using a heat pipe to cool a photovoltaic cell in a concentrated system. They addressed two important problems with conventional systems and tried to solve the issues by designing a proper reflecting surface profile for the reflecting system and combining the solar cell with the heat pipe. The solar reflector was tested with the cooling system and the temperature did not rise above 46 °C. In contrast, in the simple system (without the heat pipe), the temperature rose to 84 °C.

1.3.2 Liquid immersion cooling

Liquid immersion is an innovative idea that uses liquid for cooling and the concentrator being applied from the front and back sides of the solar cells. Russell [17] patented the idea of putting the solar cells on the elongated tube filled with the fluid to cool the cell while using the fluid as an optical concentrator (Figure 1.3):

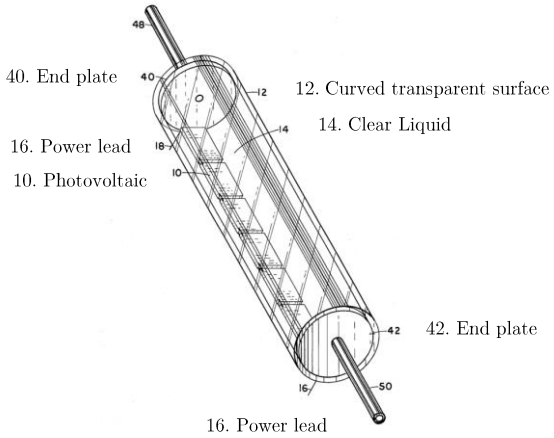

Figure 1.3. View of the optical concentrator for liquid immersion cooling [17]

Liu et al. [18] also proposed an idea where the solar cells are immersed directly in dielectric liquid. The advantage of this approach is to reduce the contact resistance for heat transfer in the cells, to dissipate more heat from the cells and keep the efficiency of cells at a constant value. The researchers tested the system under irradiances of 50 and 70 kW/m^2. The result for turbulent flow with a convection heat transfer of about 1,000 W/m^{2}K showed a uniform temperature with only about 3 °C of non-uniformity.

Han et al. [19] investigated the performance of immersed solar cells in the dielectric fluid. In their analysis, four different fluids (i.e., water, isopropyl alcohol (IPA), ethyl acetate, and dimethyl silicon oil) were tested as possible immersion liquids based on their optical transmittance measurements. The results showed an acceptable range of temperatures for solar cells. Haijun et al. [20] conducted a numerical simulation for heat transfer of the cylindrical liquid immersion system. A three-dimensional numerical simulation model was established to investigate the direct-contact heat transfer process, with the conclusion that the simulation was in good agreement with the experiment results. Thus, the simulation could be used to predict the performance of the system.

1.3.3 Micro-channels

Micro-channels have been extensively reviewed with regards to cooling processes for electronic devices. Xu et al. [21] conducted an experiment with a heat sink comprised of micro-channels and separated the whole flow field into several zones. The channels included several parallel, longitudinal, and transverse micro-channels. The authors reported an improvement of 26.4% in the Nusselt number, while the pressure drop decreased by 27%, in comparison to earlier designs. Wang and Ding [22] investigated a micro-channel that consisted of parallel longitudinal micro-channels etched in a silicon substrate and transverse micro-channels electroplated onto a copper heat spreader (Figure 1.4). De-ionized water was used as the working fluid in the channel. The results showed a uniform temperature distribution throughout the heated area.

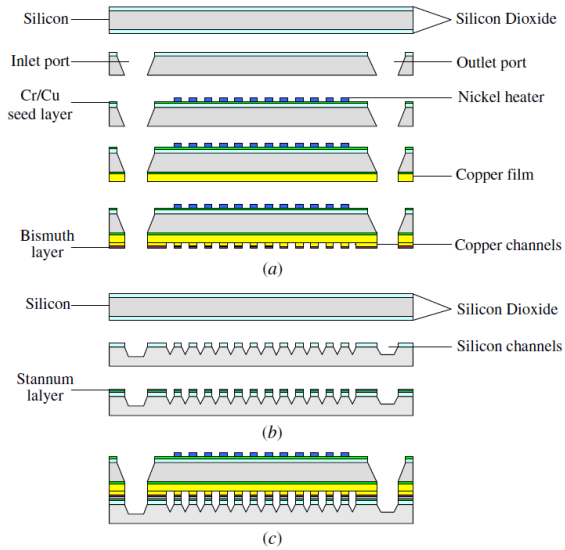

Figure 1.4. Process flow for (a) copper heat spreader, (b) silicon substrate, and (c) micro-channel heat sink. [22]

The authors found that the addition of the transverse micro-channels enhanced the cooling capability when compared to a conventional channel, and the method could be used for high heat flux applications like electronics and CPV systems. In other research, an energy and exergy analysis of PV panels combined with micro-channels was investigated by Agrawal and Tiwari [23]. Based on their numerical computations, overall annual thermal and exergy gains were increased by 70.62% and 60.19%, respectively, when compared to simple panels.

1.3.4 Heat exchanger

Heat exchangers can also be used to cool PV cells. In this process, a specific fluid, usually water, is used to cool down the panel. The output of the system is hot water, which leaves the panel and keeps the efficiency constant. The hot water can be used for different purposes like space heating or domestic usage. Kumar and Rosen [24] conducted a complete review of using air as the working fluid to cool the panel with the hot air being used for air heating. In their research, different channel orientations were combined with extended surfaces and investigated thoroughly. Nizetic et al. [25] investigated the impact of air profile on the cooling of conventional PV panels and used a numerical analysis for predicting the performance of the system. Two commonly used photovoltaic technologies (poly-Si and mono-Si) were tested to find the effect of the backside air convective thermal profile on PV panel performance. The flow separation that occurs at the PV panel's backside was found to play an important role in cooling the system. In fact, the separated layer acted as a kind of thermal insulation, causing a specific shape for the backside convective thermal profile. This effect ultimately increases the average PV panel temperature and increases the degradation rate for the panel electrical efficiency.

Mattia et al. [26] developed a dynamic model for predicting the performance of photovoltaic panels that are cooled with water. The authors used a dynamic numerical analysis with MATLAB® that was based on the lumped capacitance approach and coupled it with a thermo-electric analogy to reproduce the behavior of photovoltaic thermal panel systems. The results were compared to experimental findings. The working fluid used in the experiment was water, which was distributed with a pipeline on the back side of the panel.

Rossi et al. [27] conducted a numerical and experimental study on hybrid retrofitted panels. Water was used to cool the panel while the system was connected to a heat pump in another cycle that made use of the hot water. To connect the water pipeline to the PV panel, different materials were used, such as polyurethane, polyurethane wood, and wood rib. The simple system (i.e., the wood rib) was found to give the best results since it provides a good contact between the panel and cooling plate while allowing the back side of the panel to be easily cooled. A numerical analysis was also conducted to evaluate the possible benefits of using thermal paste. The results showed that the thermal resistance can be effectively decreased to improve the performance of the system.

Hussein et al. [28] investigated using nano particles to cool a photovoltaic panel with water. The authors reported that, without an active cooling system, the temperature of the panel reached 76 °C, but when using a water circulation line, the temperature dropped to 70 °C. Adding Zn-H_2O at a concentration of 0.3% decreased the temperature to 58 °C, which permitted a 7.8% increase in the electrical efficiency.

Freeman et al. [29] proposed using a small-scale combined solar heat and power (CSHP) system based on the ORC and investigated it numerically with an unknown expander. In the system, the new working fluid was specifically used to cool the panel while the resulting

hot fluid was re-used in a Rankine power generation cycle. The authors mentioned that the system can also be combined with a heat exchanger to provide hot water for domestic use.

1.4 Purposes and objectives

The methods reviewed above may be able to improve the performance of photovoltaic panels by cooling them, though they cannot add extra power to the system. In this project, we aim to assess whether or not a power cycle with a new turbine and a new working fluid can both cool the panel and generate extra electricity from the system.

As the first step, in Chapter 2 and 3, thermodynamic properties of different working fluid are investigated, also a complete thermodynamic analysis of the Rankin cycle with each of suggested working fluids are conducted and the best fluid for the future use in the cycle is introduced.

In Chapter 4, it is aimed to develop an analytical solution for designing the cooling system by using resistance analogy for modeling the photovoltaic panel. Finally, the results of the developed algorithm are compared with CFD simulation.

Chapter 5 aims to compare different approaches to model the turbine which is going to be used in the cycle. In this chapter different methods of modeling are reviewed, and the results are aimed to be compared with CFD simulation and experiment. Finally, Chapter 6 demonstrates the results of the assessment for using the power cycle combined with a cooling system for a sample data in Egypt.

Chapter 2: Thermodynamic Analysis of the Cycle

To analyze a solar system, a complete thermodynamic analysis is needed to examine the important parameters such as mass flow rate, temperature, and the working pressure of the cycle. To achieve this goal, the first step is to define the proper cycle for the power generation. In this thesis, a Rankine cycle is chosen for power generation for its simplicity and ease for use in future implementations. In this chapter, we review the Rankine cycle with regards to its temperature-entropy diagram. Then, a thermal analysis is conducted for different working fluids to determine the key parameters for choosing the fluid.

2.1 Rankine Cycle

A typical Rankine cycle consists of four processes. First, the working fluid is heated in the boiler, and the temperature is increased to the boiling temperature. The steam that is produced is sent to the expander (turbine) to generate the power in the vapor cycle. The low-pressure steam leaving the turbine is sent to the condenser, releasing heat into the ambient and turning into water. In the last step, the water is pumped back to the boiler, and the process is repeated (Figure 2.1):

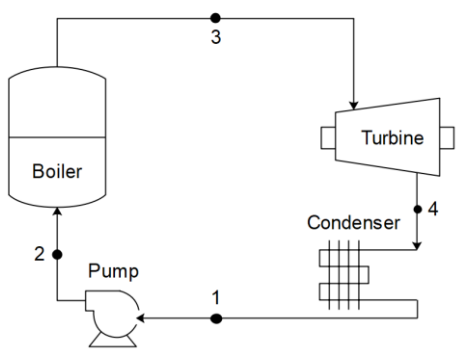

Figure 2.1. Schematic view of the Rankin cycle and its main components

It is also convenient to show the above process in common thermodynamic diagrams such as T-s (Temperature – Entropy), P-V (Pressure – Volume), or P-h (Pressure – Enthalpy) (Figure 2.2):

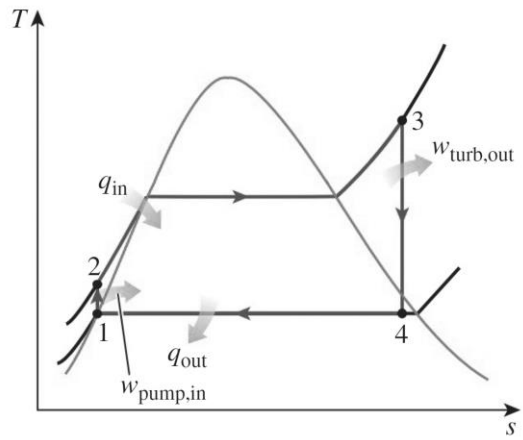

Figure 2.2. T-s diagram for a simple Rankine cycle [30]

From Figure 2.2, the process clearly consists of four important sub-processes. Since the diagram shows the ideal Rankine cycle, the compression and expansion processes are assumed to be isentropic, though in actual systems these lines are not vertical.

2.1.1 Organic Rankine Cycle (ORC)

The idea behind the Organic Rankine Cycle (ORC) is like that of the Rankine cycle, except for the working fluids that are used in the cycles. In a typical Rankine cycle, water is used as the working fluid, while in ORCs, the working fluid is chosen so as to have a low boiling temperature to make it suitable for use in systems with low-grade energy sources.

Different fluids show various behaviors when they are used in the cycle, and their specific behavior will make them a suitable option for specific applications. In the T-s diagram

(Figure 2.3), the slope of the saturated vapor line for fluids like water (wet fluids) is negative, for other fluids like pentane (dry fluids), it is positive, and for fluids like R-11 (isentropic fluids), it is a vertical line. As explained by Groniewsky et al. [31], these fluids can be more accurate defined based on their final state of fluid in a reversible adiabatic expansion. As shown in Figure 2.3, if the final state of the fluid is within the two-phase region, the fluid is called a "*wet fluid*". For "*dry fluids*" the end point will be in the dry vapor region, and for "*isentropic fluids,*" the final point is at the saturated line.

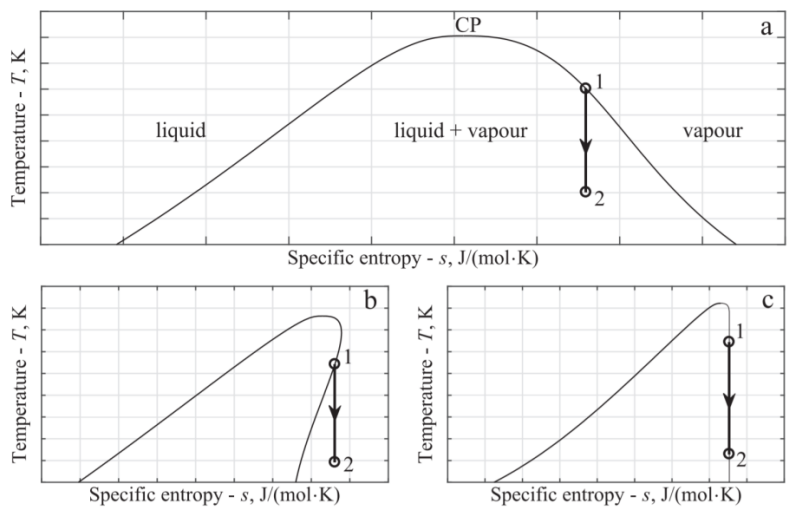

Figure 2.3. Different isentropic expansions for (a) wet fluids (b) dry fluids and (c) isentropic fluids [31]

2.1.2 Cycle Calculation

Some key parameters like mass flow rate, rejected heat, absorbed heat, etc. need to be defined for one cycle. The heat addition process occurs in the boiler or at the hot source of the system from point 2 to point 3 (Figure 2.2). The absorbed heat in this process can be calculated by the following equation:

$$Q_h = \dot{m}(\mathbf{h}_3 - \mathbf{h}_2) \quad \textbf{2.1}$$

where $\dot{m}$ is the mass flow rate of the cycle and $\mathbf{h}_3$ and $\mathbf{h}_2$ are the enthalpy of the working fluid at points 3 and 2, respectively. Using the same approach, the rejected heat can be calculated as follows:

$$Q_c = \dot{m}(\mathbf{h}_4 - \mathbf{h}_1) \quad \textbf{2.2}$$

If we consider a non-ideal expansion in the turbine, then the enthalpy of the fluid at the outlet of the turbine will change and will no longer be equal to $\mathbf{h}_4$. To find the enthalpy at point 4 for the non-ideal cycle, the isentropic efficiency can be defined in the following form:

$$\eta_s = \frac{\mathbf{h}_{4a} - \mathbf{h}_3}{\mathbf{h}_4 - \mathbf{h}_3} \quad \textbf{2.3}$$

where $\mathbf{h}_{4a}$ is the actual enthalpy at point 4 and $\mathbf{h}_4$ is the theoretical enthalpy at this point. To find the output power of the system, the energy equation can be solved for the turbine. If we assume that the mechanical efficiency of the turbine is η_m then the work generated by the turbine is:

$$W = \dot{m}(\mathbf{h}_3 - \mathbf{h}_4)\eta_m \quad \textbf{2.4}$$

2.2 Proper Fluid Criteria

Different fluids can be chosen to work in the ORC or in a simple Rankine cycle by first reviewing the fluid selection criteria, as described below:

2.2.1 Critical Temperature and Pressure

To design a simple Rankine cycle, we must consider that the temperature of the working fluid should not reach its critical temperature, which would hinder the prediction of fluid properties and the performance of the system. Also, for fluids that have a low critical temperature, the condensation process will be complicated. For all cycles, heat rejection occurs at the condenser and to have an efficient heat rejection, a 15-20 ℃ temperature difference with the ambient temperature will be needed. Thus, the operating temperature of the fluid should be about 40℃ during heat rejection. If the critical temperature of the fluid is below this temperature, the heat rejection process will become difficult due to the complex condensation. Consequently, fluids like methane that have a low critical temperature cannot be used in the cycle.

2.2.2 Environmental Effect

In any mechanical systems, a possibility exists that leakages may occur, so the working fluid must be environmentally-friendly. In particular, issues like the Ozone Depletion Potential (ODP) and Global Warming Potential (GWP) must be considered when choosing a working fluid. As reviewed by Chen et al. [32], some working fluids like R-11, R-22, and R-113 have been phased out, and other fluids like R-21, R-22, and R-124 will be phased out by 2030.

2.2.3 Stability and Compatibility with materials

For the simple Rankine cycle, water as the working fluid is compatible with most materials; however, for the ORC, other working fluids with different chemical behaviors may be used that are non-corrosive and compatible with all components of the cycle.

2.2.4 Flow Rate

One of the main challenges in dealing with a low-grade energy source, like solar energy, is the limited energy that is available for the cycle. In such conditions, using a fluid with a high latent heat will decrease the flow rate of the system. Since the operation of the expansion components (i.e., the turbine) is a function of the mass flow rate, fluids that produce higher flow rates should be used to yield a higher working efficiency.

Chapter 3: Choosing Proper Fluids for the Solar Cycle

The first step in choosing the proper fluid is to define the cycle and the basic underlying assumptions. In this project, the boiler in the Rankine cycle was replaced with a solar photovoltaic panel. The energy is absorbed by the panel and transferred to the working fluid. The resulting hot fluid is then used to run the turbine for power generation. Water, R-245-fa, R-134a, R-600, R-22, R-32, ethanol, and R-152-a were chosen as working fluids for this discussion. The thermal properties of these fluids are listed in Table 3.1:

Table 3.1. Thermal properties of the suggested working fluids

Fluid	Name	Molecular Weight	$T_c\ [K]$	$P_c\ [MPa]$	$C_p\ \left[\frac{J}{Kg\ K}\right]$	Latent Heat (L) [kJ/kg]
Water	-	18	647.1	22.06	1943.17	2391.8
R-245-fa	1,1,1,3,3-Pentafluoropropane	134.05	427.2	3.64	980.9	177.08
R-134a	1,1,1,2-Tetrafluoroethane	102.03	374.21	4.06	1211.5	155.42
R-600	Butane	58.12	425.13	3.8	1965.6	336.82
R-22	Chlorodifluoromethane	86.47	369.30	4.99	3884.02	89.69
R-32	Difluoromethane	52.02	351.26	5.78	2301.61	218.59
Ethanol	-	46.07	513.8	6.3	2460	846
R-152-a	1,1-Difluoroethane	66.05	386.41	4.52	1456.02	249.67

To analyze the cycle, the following assumptions are made:

1. The incident radiation is assumed to be 900 W/m^2.
2. Edge losses through the panels are assumed to be 5%.
3. The panel electrical efficiency is assumed to be 15%.
4. The condenser temperature is set to be 15 ℃ higher than the ambient temperature, which is 25 ℃.
5. The isentropic efficiency of the turbine is set to 50%.
6. One photovoltaic panel has an area of 2 m^2.
7. The maximum temperature for a panel is assumed to be 130 ℃, and the fluid temperature is assumed to reach 120 ℃ in the best case. This temperature can be limited by the critical temperature of some of the aforementioned fluids.
8. The ideal generated power for the Rankine cycle is assumed to be 50 W.

The maximum temperature for the fluid is assumed to be 120 ℃, so that for each fluid, the pressure corresponding to the maximum temperature can be found and set as the maximum pressure. With a known maximum pressure, the different working pressures can be defined for each fluid, and the mass flow rate needed to generate 50 Watts of power can be calculated. Finally, the amount of energy needed to be added to the collector can be calculated and the results are then compared to the maximum available energy for one photovoltaic panel, as shown below:

$$q'' = S - q_{edge} - E_{electrical} \qquad \textbf{3.1}$$

where S is the solar radiation, q_{edge} is the energy loss from the edge of the panel, and $E_{electrical}$ is the electrical energy generated by the photovoltaic panel. With the above

assumptions, the final available energy for one panel (2 m^2) will be 1440 Watt. The detailed properties for the fluids in the T-s diagram and at each critical point (Figure 2.2) for different working fluids are in Appendix C. Figure 3.1 shows the absorbed heat needed to run the cycle with different working fluids and different working pressures.

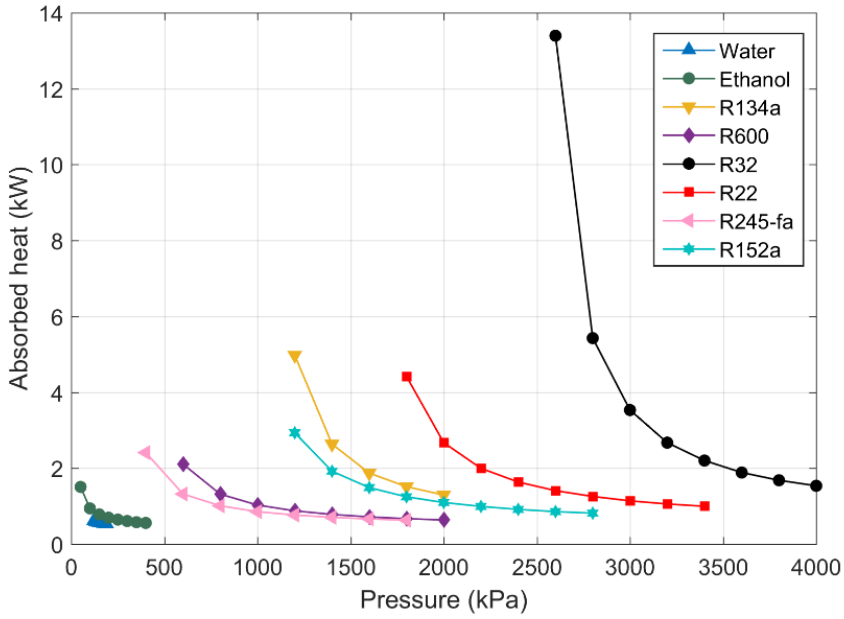

Figure 3.1. Energy needed to run the cycle with different working fluids and different working conditions

As stated above, the amount of energy for one panel is limited to 1.44 kW, so that all of the points above the 1.44 kW line in Figure 3.1 will be eliminated as operating points. Moreover, according to the literature [33], since most of these systems are used in residential applications, the maximum pressure would be limited to 13 bar, or in some cases 10 bar. In this research, we set the upper limit to 15 bar, and with these constraints, only a few working points could be used for the cycle.

Figure 3.2 shows the mass flow rate of only the working points that satisfy the above constraints.

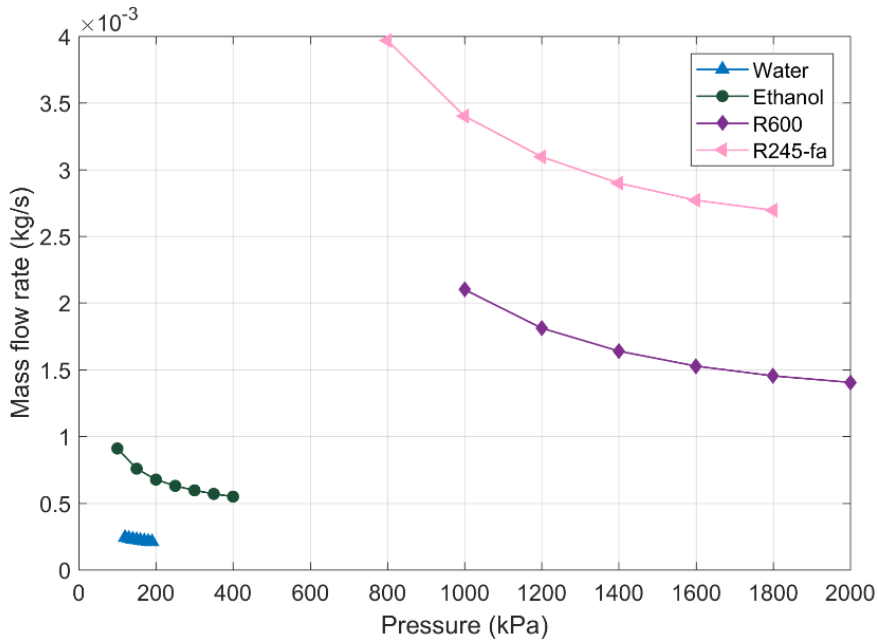

Figure 3.2. The mass flow rate for the working points that satisfy the constraints

From Figure 3.2, only four of the eight possible fluids can be used in the cycle. Moreover, from the discussion in Chapter 2, the performance of the expander is a function of the flow rate in the system. In most ORCs, since the system has a low-grade source of energy, the flow rate would be less than that of a typical cycle, which explains why new working fluids must be chosen for these cycles. From Figure 3.2, the flow rate for water is too low, which would not allow the turbine to run. From the different options, R-245-fa has the highest flow rate, making it a suitable option for the cycle. Thus, R-245-fa with 800 kPa pressure would be the proper working point to satisfy the pressure and available energy limits and to provide the highest flow rate for the system. In addition, since R-245-fa is an isentropic fluid, it would not be necessary to superheat the fluid in the Rankine cycle.

3.1 First and second law of thermodynamic analysis

For the defined working fluid and based on the thermodynamic analysis of the cycle, the first and second law efficiency of the cycle can be determined. The maximum temperature which can be achieved for R245-fa with 800 kPa is considered to be 120 ℃ and the minimum temperature is set to be 40 ℃, so the maximum first law efficiency can be determined from the following equation:

$$\eta_{I-max} = 1 - \left(\frac{T_C}{T_H}\right) \qquad \textbf{3.2}$$

where T_c is the cold temperature and T_H is the highest temperature of the cycle. Using equation 3.2, the maximum achievable first law efficiency for the cycle is 21%.

Also, for the cycle, by calculating the exergy destruction, the second law efficiency of the Rankine cycle with R245-fa as a working fluid can be determined:

$$\eta_{II} = 1 - \frac{x_{destroyed}}{x_{expanded}} \qquad \textbf{3.3}$$

where $x_{expanded}$ shows the useful available energy, which can be calculated from equation 3.4:

$$x_{expanded} = \left(1 - \frac{T_{amb}}{T_H}\right) q_{in} \qquad \textbf{3.4}$$

where T_{amb} is the ambient temperature, and q_{in} is the absorbed heat in the cycle. Equation 3.5 can also be used to calculate exergy destruction in a process:

$$x_{destroyed} = T_{amb}(\Delta s - \frac{q}{T_{source}}) \qquad \textbf{3.5}$$

where Δs shows changing in the entropy and T_{source} represents the source temperature of the process. Equation 3.5 can be used for each element in the cycle (pump, panel, turbine,

condenser) to find the exergy destruction. Using the numbers shown on Appendix C, the second law efficiency can be calculated as shown in the table below:

Table 3.2. Exergy destruction in each process of the cycle

	$\Delta s \left[\frac{kJ}{kg\ K}\right]$	T_{source}[°C]	$q \left[\frac{kj}{kg}\right]$	$x_{destruction} \left[\frac{kj}{kg}\right]$
Boiler (Collector)	0.723	120		22.94
Turbine	0.034	-	0	10.13
Condenser	-0.757	40		3.87

With the calculated exergy destruction on Table 3.2, the expected second law efficiency for the system is determined to be 42%.

Chapter 4: Modeling the Solar Panel Cooling System

One of the most important parts of the cycle is the solar collector. In the described system, the solar collector plays two roles:

1. Generating electricity with a photovoltaic cell
2. Transferring excess heat to the working fluid to generate electricity in the power cycle

Therefore, this part of the system must be modeled to predict the number of tubes needed to cool the panel. In this chapter, a resistance analogy is used to model the collector, as discussed by Duffie and Beckman [34], and the equations for the solar panel are combined with the equations for the flow in the tubes, to design the cooling system. Finally, the results of the modeling are compared with the results from a CFD simulation.

4.1 Analytical Solution

To describe the performance of the cooling system in the steady-state condition, the energy balance can be used to derive the governing equation. In the equation, incident solar energy is the useful energy that enters the system. Thermal losses also occur from different surfaces of the panel, and eventually, the energy is transferred to the working fluid at the bottom side of the panel.

Thermal energy leaves the system by way of three different mechanisms: conduction, convection, and radiation, which can be represented as the heat transfer coefficient (U_L) multiplied by the difference between the mean absorber plate temperature (T_{pm}) and the ambient temperature (T_a). In the steady-state condition, the useful energy output of the

collector of area A_c is the difference between the absorbed solar radiation and the thermal loss:

$$Q_u = A_c\left[S - U_l\left(T_{pm} - T_a\right)\right] \qquad 4.1$$

To model the system (Figure 4.1), a number of simplifying assumptions can be made to describe the performance of the system without obscuring the underlying physics. The assumptions are as follows:

1. The performance is at steady-state.
2. The solar radiation will cover the photovoltaic panel uniformly.
3. The solar energy is not absorbed by the cover.
4. The cover has a uniform temperature.
5. The heat flow through the back insulation is one-dimensional.
6. The temperature drop through the cover is negligible.

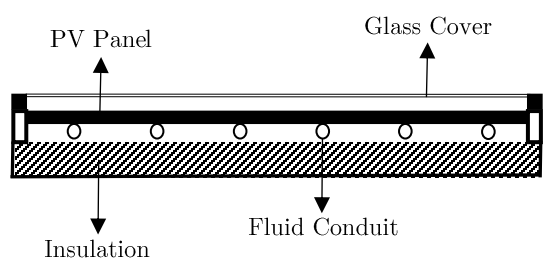

Figure 4.1. Front view of the photovoltaic panel with glass cover and cooling tubes

The first step in modeling the above system is to find different mechanisms that will result in the heat loss from the system. For the glass cover, two important mechanisms can dissipate the energy. One part of the energy will be lost by radiation to the ambient, while the other part will be dissipated by convection. Since the collector is in an atmospheric

condition and the thermal conductivity of air is relatively low, conduction can be neglected. For the air between the glass cover and the photovoltaic panel, the dominant mechanism for heat loss is natural convection. Furthermore, radiation can be another mechanism for the heat loss. Heat transfer in the photovoltaic panel occurs mainly by conduction, and the energy will then be transferred to the working fluid in the tubes. Heat loss may also occur through the back insulation due to conduction. By describing the possible mechanisms of heat loss from the panel, we can use the resistance analogy and define the following resistance circuit to model the system (Figure 4.2):

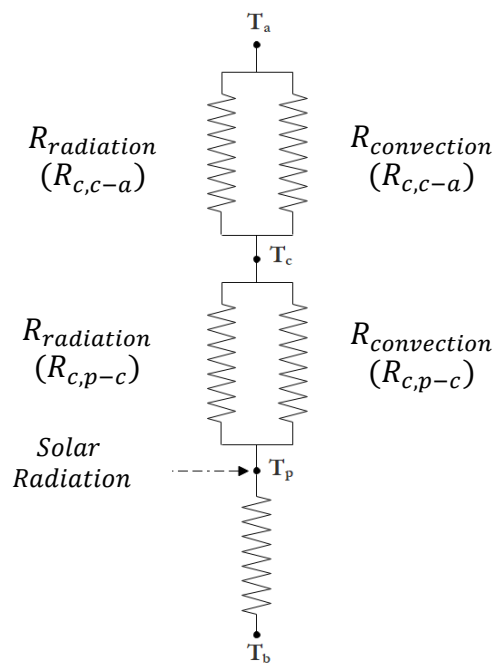

Figure 4.2. Thermal resistance diagram of the system

In Figure 4.2, T_a, T_c, T_p, and T_b are the ambient, cover, plate, and bottom temperature, respectively. The energy loss through the top is the result of convection and radiation between the plate and the glass cover. Equation 4.2 can be used to find the heat transfer with radiation between two plates:

$$q_{r,p-c} = \frac{\sigma\left(T_p^4 - T_c^4\right)}{\frac{1}{\varepsilon_p} + \frac{1}{\varepsilon_c} - 1} \qquad 4.2$$

The above equation can be rearranged and written in the form of a radiative heat transfer coefficient and temperature difference:

$$q_{r,p-c} = \frac{\sigma\left(T_p + T_c\right)\left(T_p^2 + T_c^2\right)}{\frac{1}{\varepsilon_p} + \frac{1}{\varepsilon_c} - 1} \times \left(T_p - T_c\right) = h_{r,p-c}\left(T_p - T_c\right) \qquad 4.3$$

The other mechanism for the heat transfer between the glass cover and the plate is natural convection. In order to calculate the heat transfer coefficient, we need to find the natural convection heat transfer coefficient between parallel plates. Natural convection between inclined parallel surfaces are usually described with three known dimensionless parameters. The Nusselt number (Nu), Rayleigh number (Ra), and the Prandtl number (Pr). These parameters and their definitions are listed below:

$$Nu = \frac{hL_g}{k} \qquad 4.4$$

$$Ra = \frac{g\beta'\Delta T\, L_g^3}{\nu\alpha} \qquad 4.5$$

$$Pr = \frac{\nu}{\alpha} \qquad 4.6$$

In the above equations, h is the convective heat transfer coefficient, L_g is the space between the parallel plates, k is the thermal conductivity, g is the gravitational constant, α is the thermal diffusivity, ν is the kinematic viscosity, and β' is the volumetric coefficient of

expansion, which for the ideal gas assumption, can be written in the form of $1/T$ where T is the temperature in Kelvin.

For air, Hollands et al. [35] give the equation for the Nusselt number and Rayleigh number for tilt angles (β) from 0 to 75° as:

$$Nu = 1 + 1.44\left[1 - \frac{1708(sin(1.8\beta))^{1.6}}{Ra\,cos\,(\beta)}\right]\left[1 - \frac{1708}{Ra\,cos(\beta)}\right]^{+} + \left[\left(\frac{Ra\,cos\,\beta}{5830}\right)^{\frac{1}{3}} - 1\right]^{+} \qquad 4.7$$

The positive sign in the above equations means that only the positive value is acceptable and for negative values, the expression is equal to zero. By combining the definition of the Nusselt number with the above equation, the convective heat transfer coefficient can be calculated:

$$h_{c,p-c} = \frac{k}{L_g}.\left(1 + 1.44\left[1 - \frac{1708(sin(1.8\beta))^{1.6}}{Ra\,cos(\beta)}\right]\left[1 - \frac{1708}{Ra\,cos(\beta)}\right]^{+} + \left[\left(\frac{Ra\,cos\,\beta}{5830}\right)^{\frac{1}{3}} - 1\right]^{+}\right) \qquad 4.8$$

And by defining the radiation and convection heat transfer coefficient, the total thermal resistance between the plate and the glass cover can be calculated:

$$R_{p-c}^{tot} = \left(\frac{1}{R_{r,p-c}} + \frac{1}{R_{c,p-c}}\right)^{-1} = \left(h_{r,p-c} + h_{c,p-c}\right)^{-1} \qquad 4.9$$

Where $R_{r,p-c}$ and $R_{c,p-c}$ are resistances as shown on Figure 4.2. With the same approach, one can see that convection and radiation heat transfers will also take place between the glass cover and the air. These two mechanisms are the most dominant heat transfer mechanisms for the glass cover. The important difference here is that the convection heat transfer is mainly caused by the wind and is a function of the wind speed. In addition, for

the radiation, we can use the typical radiation heat transfer equation between the plate and an infinite surface, which can be written as:

$$q_{r,c-a} = \sigma\varepsilon(T_a + T_c)(T_a^2 + T_c^2)(T_c - T_a) \qquad \mathbf{4.10}$$

Therefore, the total thermal resistance between the glass cover and the ambient can be calculated as follows:

$$R_{c-a}^{tot} = \left(\frac{1}{R_{r,c-a}} + \frac{1}{R_{c,c-a}}\right)^{-1} = \left(h_{r,c-a} + h_{c,c-a}\right)^{-1} \qquad \mathbf{4.11}$$

By combining equations (4.9) and (4.11), we can see that the total top heat loss coefficient can be expressed as:

$$U_t = \frac{1}{R_{c-a}^{tot} + R_{p-c}^{tot}} \qquad \mathbf{4.12}$$

Moreover, the natural convection heat transfer coefficient is a function of the Rayleigh number, which is a function of the temperature difference between the plate and the cover, when we have the temperature of the plate, we still need to find the temperature of the glass cover. This temperature is not discernible unless we start with an initial guess and do an iteration to find the final temperature. The iterative procedure is described in the notes for Figure 4.3.

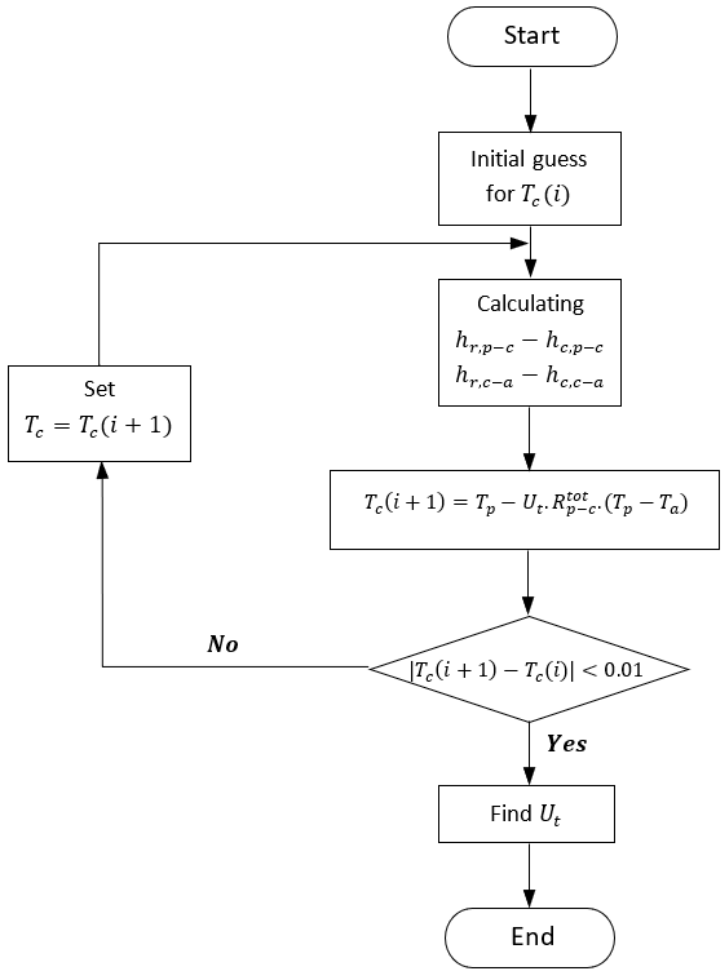

Figure 4.3. Flow diagram for calculating the total heat loss coefficient

By finding the final temperature for the glass cover, the total heat loss coefficient and the total heat loss from the top surface can be determined. In addition, from the properties of the back insulation, we can find the heat transfer coefficient form the bottom of the collector, and the net heat can be expressed as:

$$E_{net} = SA_c - U_l A\left(T_{pm} - T_a\right) \quad \textbf{4.13}$$

The net energy will be transferred to the photovoltaic panel and finally to the working fluid. As it stated in [34], a fin analogy can be used to find the temperature distribution in the photovoltaic panel. Figure 4.4 is a schematic view of the panel with the tubes:

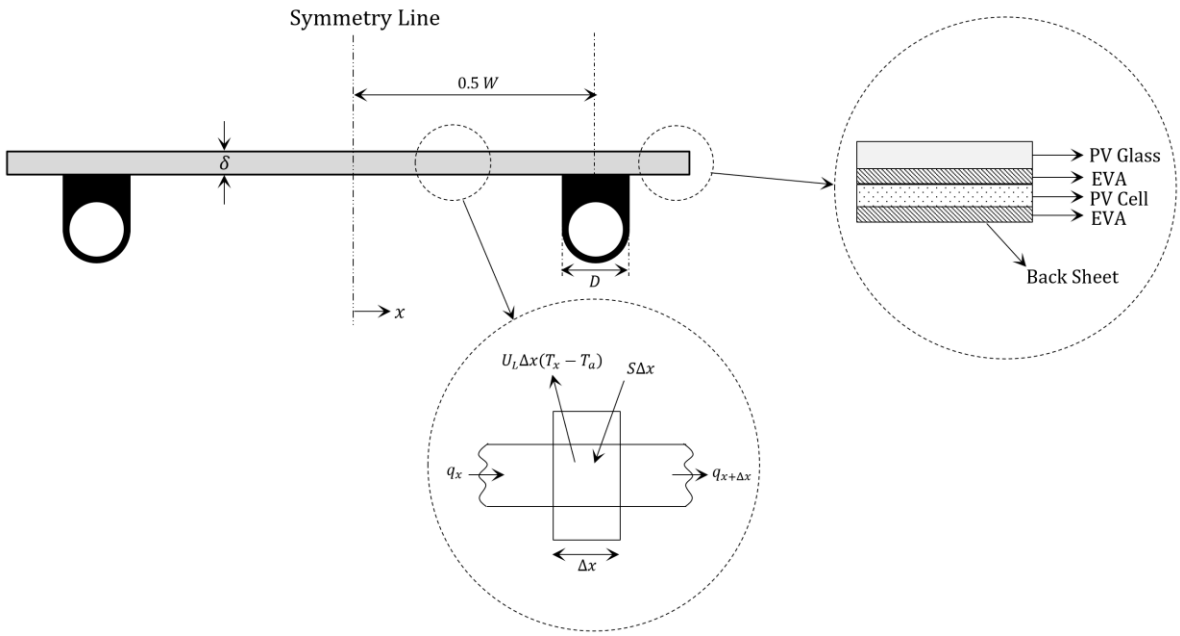

Figure 4.4. View of photovoltaic panel and the cooling tubes

In Figure 4.4, the photovoltaic panel is seen to consist of five different layers. The thermal properties of these layers are listed in Table 4.1.

Table 4.1. Thermal properties of the different layers of the photovoltaic cells [27]

Layer	Thickness [mm]	Thermal Conductivity [W/(m. K)]
PV Glass	2.8	1.8
EVA	0.5	0.35
PV Cell	0.3	148
EVA	0.5	0.35
Back sheet	0.1	0.2

Beginning with the first law analysis of the photovoltaic plate, the following balanced energy equation can be written for the panel:

$$E_{in} - E_{out} + E_{solar} - E_{heat\ loss} = 0 \qquad 4.14$$

Considering a small element with thickness Δx, equation 4.14 can be rewritten as:

$$\left(-k\delta \frac{dT}{dx}\right)_{|x} - \left(-k\delta \frac{dT}{dx}\right)_{|x+\Delta x} + S\Delta x - U_l \Delta x (T_x - T_a) = 0 \qquad 4.15$$

where δ is the thickness of the plate, k is the thermal conductivity of the plate, and S is the solar radiation. Dividing equation 4.15 by Δx and letting Δx approach zero, we arrive at the following equation:

$$\frac{d^2T}{dx^2} - \frac{U_l}{k\delta}\left(T - T_a - \frac{S}{U_l}\right) = 0 \qquad 4.16$$

To solve equation 4.16, two boundary conditions are needed. Since the geometry has a symmetry line, the insulated wall can be considered as the boundary condition at $x = 0$; and at the end of the plate, we can consider that the temperature is known. These two boundary conditions can be stated as:

$$\frac{dT}{dx}_{|@x=0} = 0\ (insulated\ wall) \qquad 4.17$$

$$T_{\left|@x=\frac{W-D}{2}\right.} = T_{bo}\ (known\ Temperature) \qquad 4.18$$

By solving equation 4.16 with proper boundary conditions, we end up with the following solution:

$$\frac{T - T_a - \frac{S}{U_l}}{T_{bo} - T_a - \frac{S}{U_l}} = \frac{cosh\left(\sqrt{\frac{U_l}{k\delta}}x\right)}{cosh\left(\sqrt{\frac{U_l}{k\delta}}\right)(W - D)/2} \qquad 4.19$$

Now, with a known temperature distribution, the heat transfer along the plate can be calculated as follows:

$$q'_{fin} = -k\delta \frac{dT}{dx}\Big|_{@x=\frac{W-D}{2}} = (W - D)F[S - U_l(T_{bo} - T_a)] \qquad 4.20$$

where F is defined as:

$$F = tanh\left[\left(\sqrt{U_l/k\delta}\right)(W - D)/2\right] / \frac{\left(\sqrt{U_l/k\delta}\right)(W - D)}{2} \qquad 4.21$$

The amount of energy calculated from equation 4.20 is only part of the energy that is conducted to the fluid through the plate. The top part of the tube can still absorb heat directly from the radiation, and thus needs to be considered in the total absorbed energy (Figure 4.5). This energy can be calculated from equation 4.22:

$$q_{tube-rad} = D[S - U_l(T_{bo} - T_a)] \qquad 4.22$$

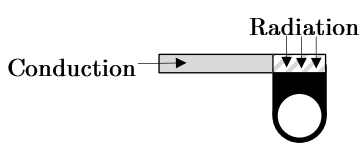

Figure 4.5. Different mechanism for heat transfer to the working fluid

The total energy can then be calculated by combining equations 4.20 and 4.22:

$$q_{tot} = \big((W - D)F + D\big)[S - U_l(T_{bo} - T_a)] \qquad \mathbf{4.23}$$

If we consider no thermal resistance for the tube bonding, then the resistance analogy will give us the following equation for the heat transfer to the tube:

$$q_{tot} = (T_{bo} - T_f)/\frac{1}{h_{fi}\pi D_i} \qquad \mathbf{4.24}$$

where h_{fi} is the heat transfer coefficient in the tube, which is a function of the length of the tube. In equation 4.24, D_i is the inside diameter of the tube, and T_f is the temperature of the fluid. Eliminating T_{bo} from equations 4.23 and 4.24, the final equation for the total heat transfer to the fluid becomes:

$$q_{tot} = WF'\big[S - U_l\big(T_f - T_a\big)\big] \qquad \mathbf{4.25}$$

where F' is defined as:

$$F' = \frac{1/U_l}{W[\frac{1}{U_l[D + (W - D)F]} + \frac{1}{\pi D_i h_{fi}}]} \qquad \mathbf{4.26}$$

In some cases, the convection heat transfer may be given, so F' can be found from equation 4.26. Nevertheless, in the design problems, h_{fi} is unknown and must be derived from other equations or experiments. For the fluid in the tubes, the heat addition process can be divided into two parts:

1. Adding heat to the working fluid in the sub-cooled phase (including increasing the temperature)
2. Adding heat to the working fluid in the saturated phase (constant temperature with heat addition)

For the first part (adding heat and increasing the temperature), a correlation with heat transfer can be used to find the heat transfer coefficient. After defining the fluid regime in the tube, the flow in the tube can be divided into two regions:

1. Entrance length
2. Fully developed region

These two regions can be seen in Figure 4.6:

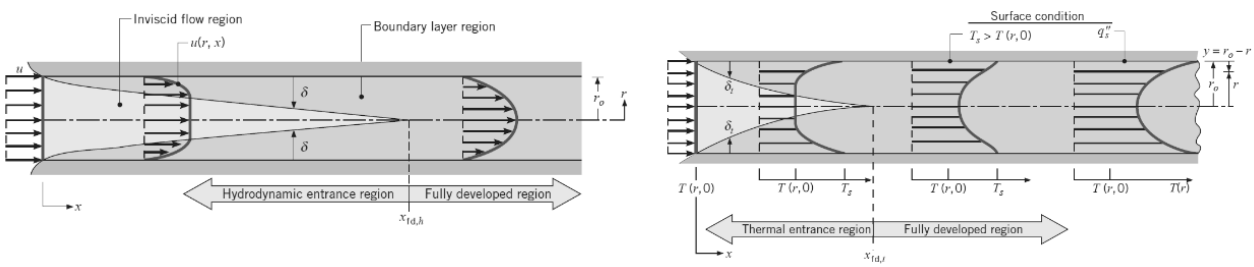

(a) (b)

Figure 4.6. Entrance and fully developed region for the hydraulic and thermal boundary layers [36]

The first region is the entrance region where either the hydraulic or the thermal boundary layers or both do not reach the fully developed condition. To find the length that is needed to reach the fully developed condition, the following equation can be used:

$$l_{entrance-hydrolic} = 0.05 \times D_i \times Re_D$$
$$l_{entrance-thermal} = 0.05 \times D_i \times Re_D \times Pr \qquad 4.27$$

where D_i is the inner diameter of the tube, Pr is the Prandtl number for the working fluid, and Re_D is the Reynolds number, which is defined by the following:

$$Re_D = \frac{4\dot{m}_{tube}}{\pi D_i \mu_f} \tag{4.28}$$

In equation 4.28, $\dot{m}_{tube}$ is the mass flow rate in the tube and μ_f is the fluid viscosity. Based on the fact that the flow is hydraulically or thermally fully developed, a different correlation is used to find the convection heat transfer coefficient. Here, we assume that if the thermal entrance length is 10-times longer than the hydraulic entrance length, then the flow is hydraulically fully developed and equation 4.29, which was presented by Kays [36], can be used for the laminar flow:

$$\overline{Nu}_D = 3.66 + \frac{0.0668\, Gz_D}{1 + 0.04\, Gz_D^{2/3}} \tag{4.29}$$

where Gz_D is the Graetz number, defined as:

$$Gz_D = \frac{D}{x}\, Re_D Pr \tag{4.30}$$

In equation 4.30, x is the distance from the inlet, and D, Re_D, Pr are the same parameters as stated earlier. If the thermal entrance length is not 10-times longer than the hydraulic entrance length, we have a combined entry condition. The following correlation, suggested by Baehr and Stephan [37], can be used to find the Nusselt number in the pipe for the combined entrance condition with constant surface temperature:

$$\overline{Nu}_D = \frac{\dfrac{3.66}{tanh\left[2.264\, Gz_D^{-\frac{1}{3}} + 1.7\, Gz_D^{-\frac{2}{3}}\right]} + 0.0499\, Gz_D\, tanh(Gz_D^{-1})}{tanh[2.432\, Pr^{\frac{1}{6}}\, Gz_D^{-\frac{1}{6}}]} \tag{4.31}$$

With the calculated Nusselt number from equations 4.29 or 4.31, the convective heat transfer coefficient can be found and inserted into equation 4.26.

As stated before, equations 4.29 and 4.31, are only for the condition when we do not have the two-phase flow. For the heat addition process in the saturated region, where the temperature is constant, and the flow phase is changing, the average number for the heat transfer coefficient can be used to prevent the need for complicated, two-phase flow equations. In addition, to use equations 4.29 and 4.31, the length of the tube must be known. Since, in design problems, this length should be determined during the design procedure, finding the heat transfer coefficient would be an iterative procedure. Moreover, during the iteration process, the length of the tube is more than the thermal and hydraulic entrance length, so that the flow will reach the fully developed region and the Nusselt number for the laminar flow in the tube with a constant wall temperature will eventually reach a constant value equal to 3.66 (Figure 4.7).

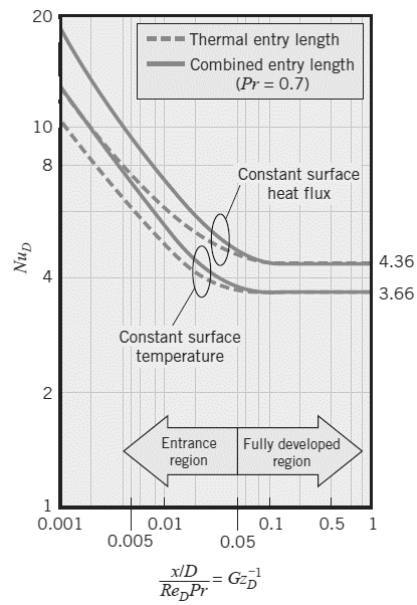

Figure 4.7. The Nusselt number variation for the entrance length and fully developed region [36]

For the above case, the heat transfer coefficient can be obtained by averaging the length of the tube both in the entrance length and the fully developed region, as follows:

$$\bar{h}_{tube} = \frac{\left[\left(l_{entrance} \times \bar{h}_{entrance}\right) + \left(l_{tube} - l_{entrance}\right) \times h_{fullydeveloped}\right]}{l_{tube}} \qquad \mathbf{4.32}$$

The energy that was calculated from equation 4.26 will finally be transferred to the working fluid. To find the fluid temperature distribution, an element of the fluid can be chosen as depicted in Figure 4.8:

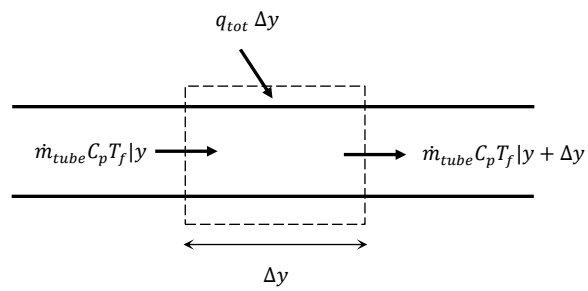

Figure 4.8. Energy balance for the fluid element in the tube

In Figure 4.8, $\dot{m}_{tube}$ is the mass flow rate of one tube, which can be found from the total mass flow rate and the total number of tubes in the system:

$$\dot{m}_{tube} = \dot{m}_{tot}/N \qquad \textbf{4.33}$$

where N is the total number of tubes and $\dot{m}_{tot}$ is the total mass flow rate. Writing the energy balance for the element, we arrive at the following equation:

$$\frac{\dot{m}_{tot}}{N} C_p \frac{dT_f}{dy} - WF'\left[S - U_l\left(T_f - T_a\right)\right] = 0 \qquad \textbf{4.34}$$

If we assume that U_l and F' are not a function of y, then we can integrate equation 4.34 and find the analytical answer for the temperature variation along the tube.

$$(T_f - T_a - \frac{S}{U_l})/(T_{f_i} - T_a - \frac{S}{U_l}) = e^{(-\frac{U_l NWF' y}{\dot{m}_{tot}})} \qquad \textbf{4.35}$$

where T_{fi} is the temperature of the fluid at the inlet. With a known length of tube and the properties of the fluid, the outlet temperature of the fluid can be defined. Furthermore, if the desired parameters of the cycle, like the outlet and inlet temperatures are known, equation 4.35 can be used to determine the length of the tube. The procedure to find the number and lengths of tubes is shown in Figure 4.9:

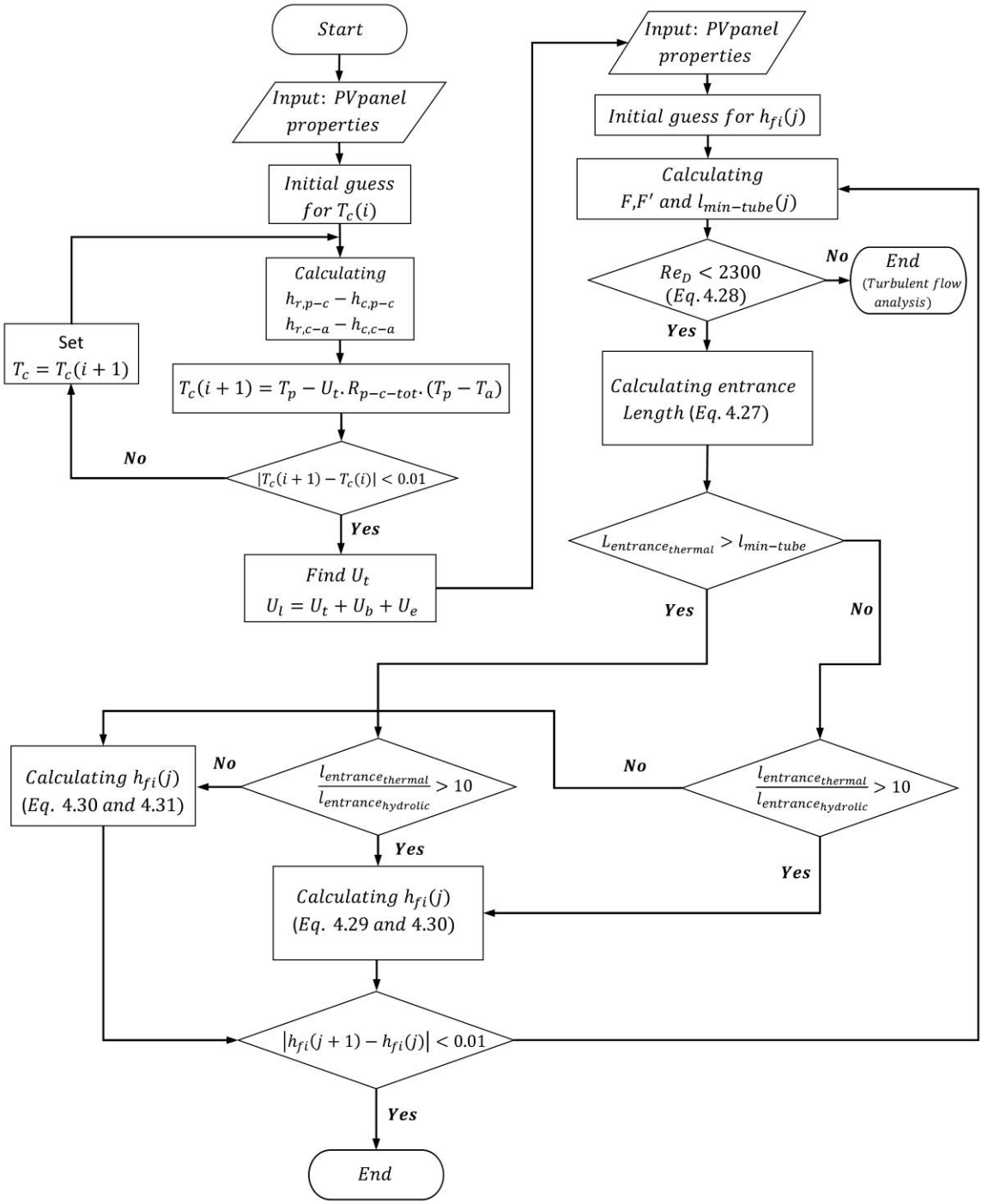

Figure 4.9. The procedure to find the average heat transfer coefficient in the pipes

The above method is valid for the part of the tube where the fluid has only one phase. For the rest of the tube, since we have a two-phase fluid, the correlation for the convective heat transfer coefficient is not valid. In this case, a typical value for the convective heat transfer coefficient for the boiling process would be chosen to be 400 W/m^2K. Equation 4.34 can be rewritten in the following form:

$$\frac{\dot{m}_{tot}}{N}\Delta h_{fluid} l - WF'\left[S - U_l\left(T_f - T_a\right)\right] = 0 \qquad \textbf{4.36}$$

In the above equation, since the working fluid is in the two-phase region or the saturated region, the temperature of the fluid is constant, so that a control volume analysis can be used.

In the method indicated in Figure 4.9, the temperature of the PV panel is set based on the experiment or previous data for the surface of the collector. To have a more accurate estimation of this temperature for a different radiation, another iteration of the plate temperature can be done to find the plate temperature [38]. Using this method, we first need to define the collector heat removal factor. If we consider a collector as a heat exchanger system, the useful gain of the heat exchanger can be defined as follows:

$$F_R = \frac{\dot{m}C_p(T_{fo} - T_{fi})}{A_c\left[S - U_L\left(T_{fi} - T_a\right)\right]} \qquad \textbf{4.37}$$

In equation 4.37, the denominator defines the maximum heat transfer that can occur in the heat exchanger, and the nominator defines the real heat transfer that will increase the fluid temperature. With a simple manipulation, equation 4.37 can be rewritten as:

$$F_R = \frac{\dot{m}C_p}{A_c U_L}\left[1 - \frac{\frac{S}{U_l} - (T_{fo} - T_a)}{\frac{S}{U_l} - (T_{fi} - T_a)}\right] \quad \textbf{4.38}$$

By combining equations 4.37 and 4.35, we arrive at the following equation:

$$F_R = \frac{\dot{m}C_p}{A_c U_l}\left[1 - \exp(-\frac{A_c U_l F'}{\dot{m}C_P})\right] \quad \textbf{4.39}$$

Thus, the collector's useful energy can be written in the following form:

$$q_u = \frac{Q_u}{A_c} = F_R[S - U_l(T_i - T_a)] \quad \textbf{4.40}$$

In addition to equation 4.40, the following equation can be used to express the useful energy of the collector:

$$q_u = [S - U_l(T_{Pm} - T_a)] \quad \textbf{4.41}$$

where T_{Pm} is the average temperature of the photovoltaic panel. Using equations 4.41 and 4.40, q_u can be eliminated and the following equation can be derived to express the average plate temperature:

$$T_{Pm} = T_{fi} + \frac{q_u}{F_R U_l}[1 - F_R] \quad \textbf{4.42}$$

Equation 4.42 refers to the function U_l, which as discussed before can be found after setting T_{pm} and doing an iteration to find T_c. Thus, finding T_{Pm} is necessarily for the iterative solution, as described in Figure 4.10:

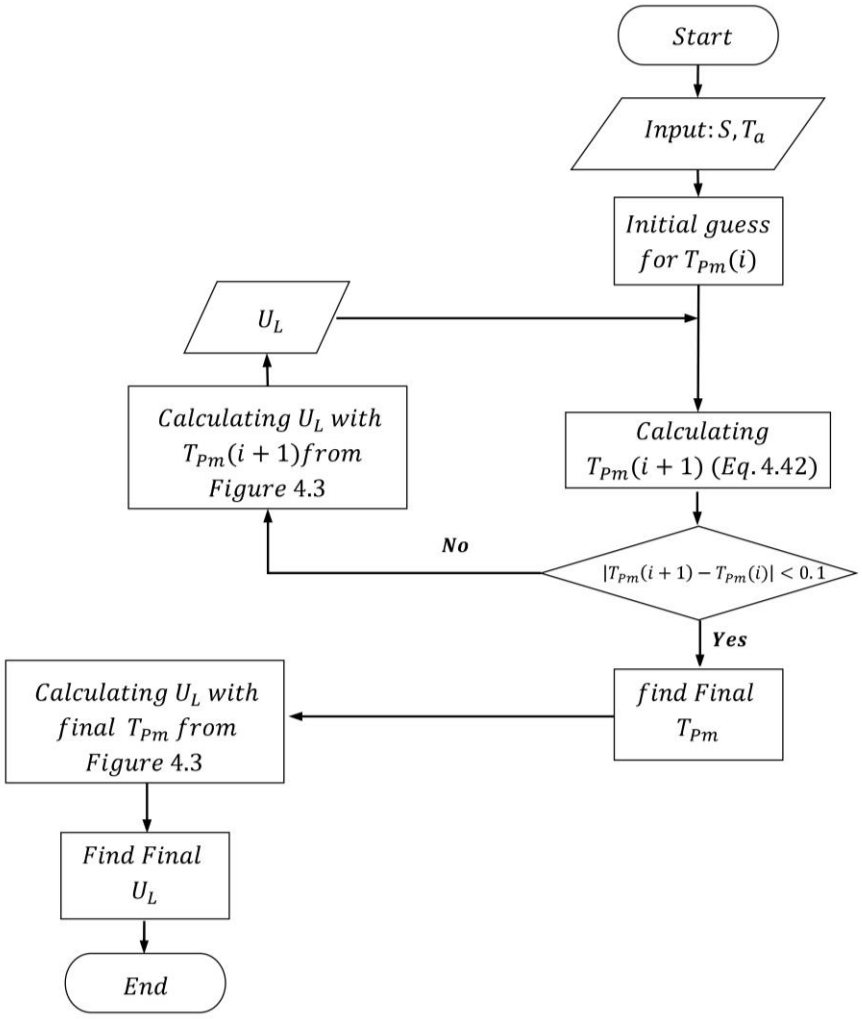

Figure 4.10. Algorithm to find the mean temperature of the panel

The overall iteration that needs to be done is shown in Figure 4.11:

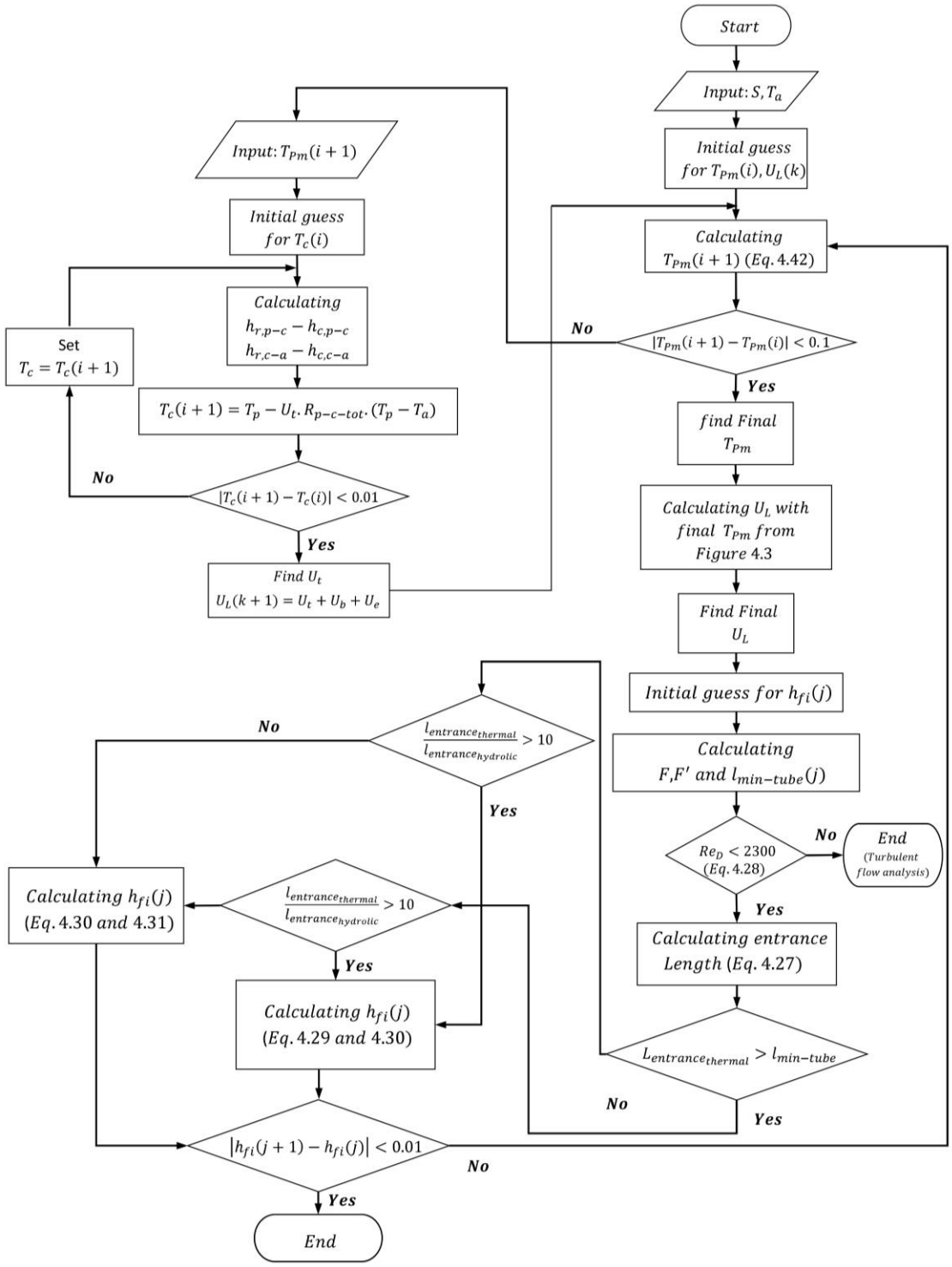

Figure 4.11. Complete iteration process to find PV and cover temperature and the length of the tube

4.2 CFD Simulation

To check if the output length from the analytical modeling (Figure 4.11) can satisfy the temperature at the outlet of the tubes, a CFD simulation was conducted for the photovoltaic panel. Since the panel consists of the same tube configurations that are distributed symmetrically, only the part of the panel with the tube under it was simulated. The model is depicted in Figure 4.12:

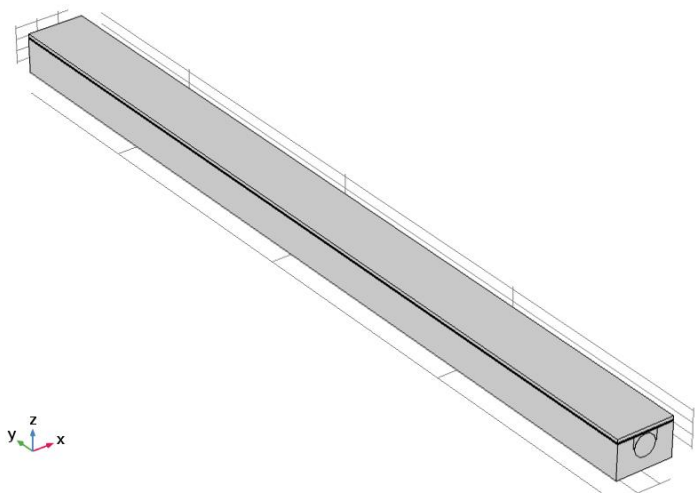

Figure 4.12. 3D geometry of the panel with the cooling tube in COMSOL

A detailed view of the above geometry with the proper thermal boundary conditions is shown in Figure 4.13:

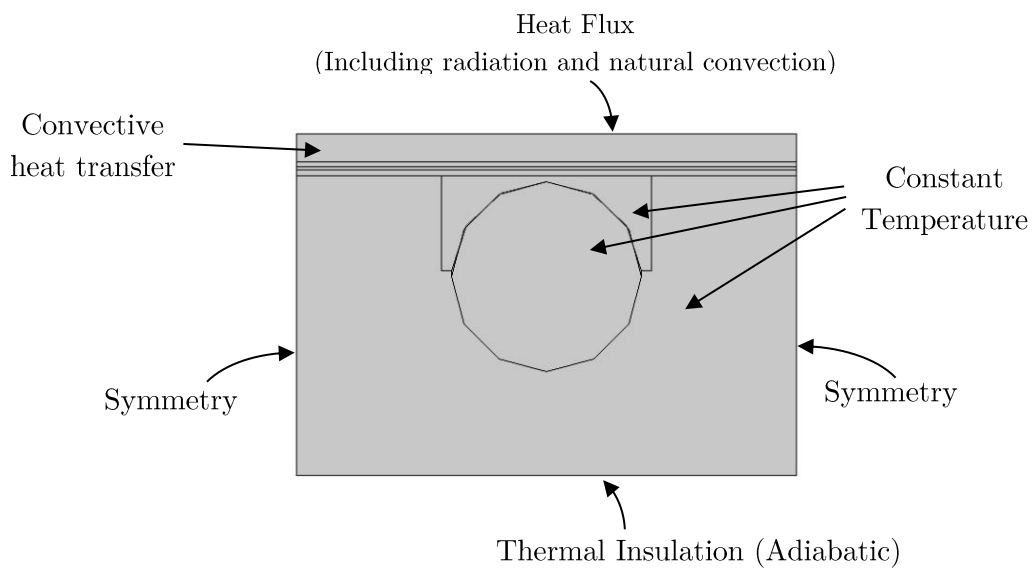

Figure 4.13. Thermal boundary conditions for the front surface of the geometry

For the back surface of the geometry, the thermal boundary conditions are the same except that the "*constant temperature*" is replaced with the "*outflow* "boundary condition.

Since the simulation also includes the working fluid that passes through the tube (conjugate heat transfer), the proper boundary conditions must be defined for the fluid domain.

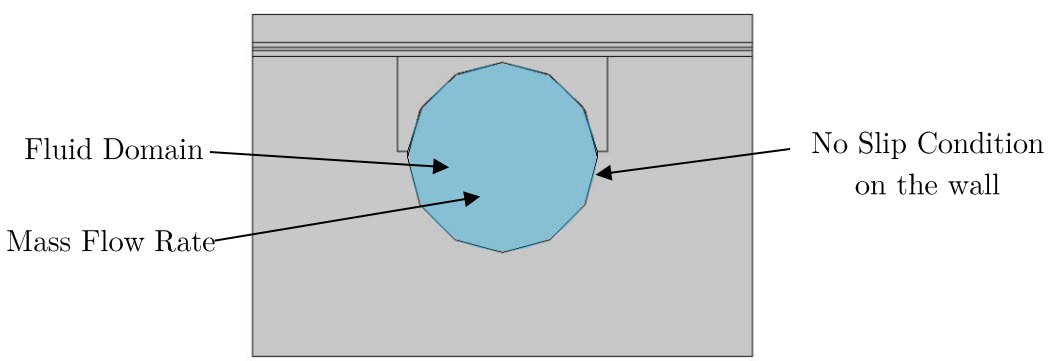

Figure 4.14. Proper boundary conditions for the fluid flow

Other settings for the simulation are listed below:

Table 4.2. Relevant settings used in COMSOL 5.2

Mesh Type	Free Tetrahedral
Element size	Maximum: 4 cm Minimum: 0.1 cm Maximum Groth Rate: 1.5
Model	Steady State - Conjugate Heat Transfer
Fluid Model	Laminar Flow

4.3 Results

4.3.1 Analytical Solution

As discussed in Chapter 3, the working fluid was chosen to be R-245-fa. The constant parameters for the collector (Table 4.3) and the properties of the fluid (Table 4.4) are listed below. For the solar radiation, for example, a maximum of 900 W/m^2 or an available energy of 765 W/m^2 was considered.

Table 4.3. Constant parameters for the collector

$\boldsymbol{L_g}$ (Distance between glass-cover)	0.025 [m]
ε_g (glass emissivity)	0.88
ε_p (PV emissivity)	0.95
h_w(Wind convective heat transfer coefficient)	5 [W/m^{2}K]

P_{atm} (ambient pressure)	101.3 [kPa]
T_p (PV Temperature)	393 [K]
β (Panel angle)	45 [degree]
Thickness of collector	0.06 [m]
g (Gravitational acceleration)	9.81 [m/s^2]
σ (Stefan-Boltzmann Constant)	5.67×10^{-8} [Wm^{-2}K^{-4}]
Panel width	1 [m]
Panel height	2 [m]
k (Thermal conductivity of photovoltaic part)	1.5 [Wm^{-1}K^{-1}]
Thermal conductivity of back insulation	0.04 [Wm^{-1}K^{-1}]
Thickness of back insulation	0.05 [m]
Thickness of edge insulation	0.04 [m]

Table 4.3. Thermal properties of the working fluid

Mass flow rate	0.00397 [kg/s]
Effective solar radiation	765 [W/m^2]
μ (Viscosity of the fluid)	3.342×10^{-4}
Pr (Prandtl number of the fluid)	5.69
Thermal conductivity of the fluid	0.0724 [Wm^{-1}K^{-1}]
Thermal heat capacity	1400 [J/kgK]
Inlet temperature	40.22 [C]
Desired outlet temperature	80.46 [C]

For the values mentioned above, different standard tube diameters (1/8, 1/4, 3/8, 1/2, 5/8, 3/4, 1, 5/4, 3/2, 2, 5/2, 3 inches) and different tube distances (5, 10, 15, 20, 25, and 30 centimeter) were considered. Due to geometric constraints, all combinations of the numbers mentioned here were not possible. The geometric constraint is presented below:

$$W - D > 0 \qquad \textbf{4.43}$$

A MATLAB® function was used to run the algorithm mentioned in Figure 4.9. Figure 4.13 shows how the minimum length of the tube changes with the tube diameter and distance.

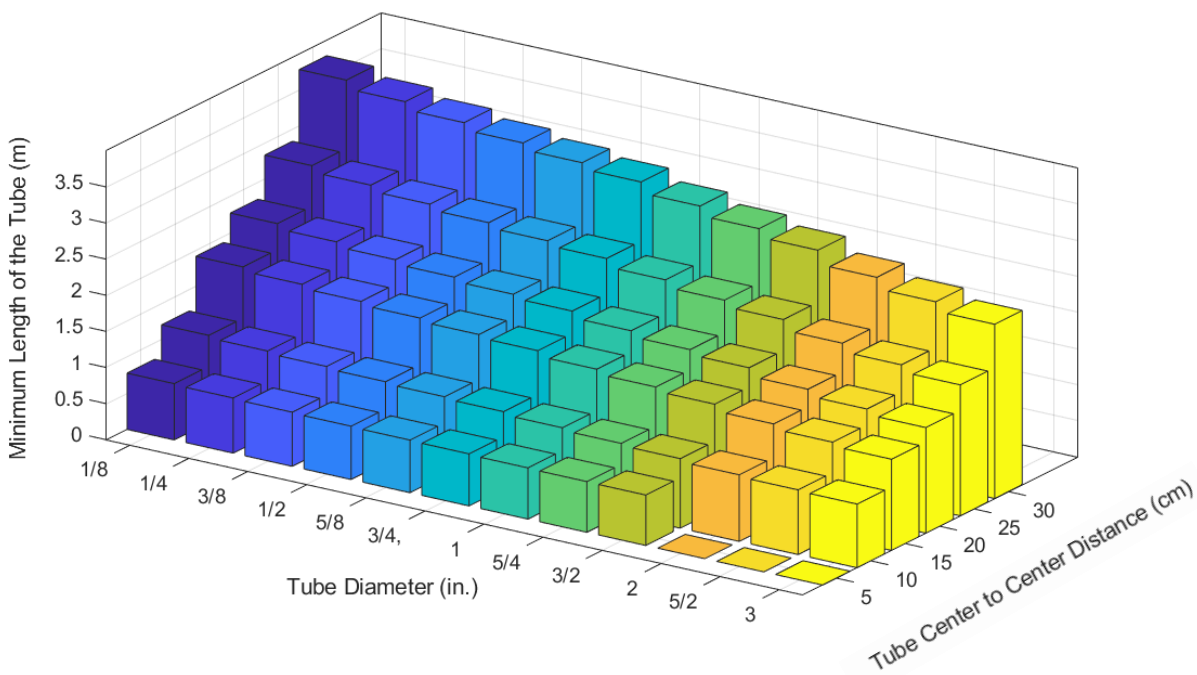

Figure 4.15. Variation of the tube length with tube diameter and distance

The numerical results for the minimum tube length for Figure 4.15 are shown in Table 4.5:

Table 4.4. Minimum tube length (in meter) for different design parameters ($\dot{m}$ =0.00397 kg/s)

		Tube Diameter (in.)											
		1/8	**1/4**	**3/8**	**1/2**	**5/8**	**3/4**	**1**	**5/4**	**3/2**	**2**	**5/2**	**3**
Tube Distance (cm)	**5**	0.77	0.75	0.74	0.73	0.72	0.71	0.70	0.69	0.69	0.00	0.00	0.00
	10	1.19	1.15	1.12	1.09	1.07	1.05	1.01	0.97	0.95	0.90	0.88	0.87
	15	1.88	1.82	1.77	1.72	1.68	1.64	1.56	1.50	1.45	1.36	1.29	1.24
	20	2.23	2.16	2.10	2.04	1.99	1.94	1.85	1.77	1.71	1.59	1.50	1.43
	25	2.78	2.69	2.62	2.54	2.48	2.42	2.31	2.21	2.12	1.98	1.87	1.77
	30	3.71	3.59	3.49	3.39	3.30	3.22	3.07	2.94	2.83	2.64	2.49	2.36

As shown in Table 4.5, a 1.5-inch tube with a center-to-center distance of 5 cm will satisfy the tube minimum length. Ultimately; however, when we consider the total length of the tube with the specified design parameters listed in Tables 4.3 and 4.4, this length can satisfy the desired outlet temperature of the working fluid.

4.3.2 CFD Simulation

To verify the values derived from the analytical solution, a CFD analysis was used for the photovoltaic cell and the tubes. The result of the simulation is presented in Figure 4.16:

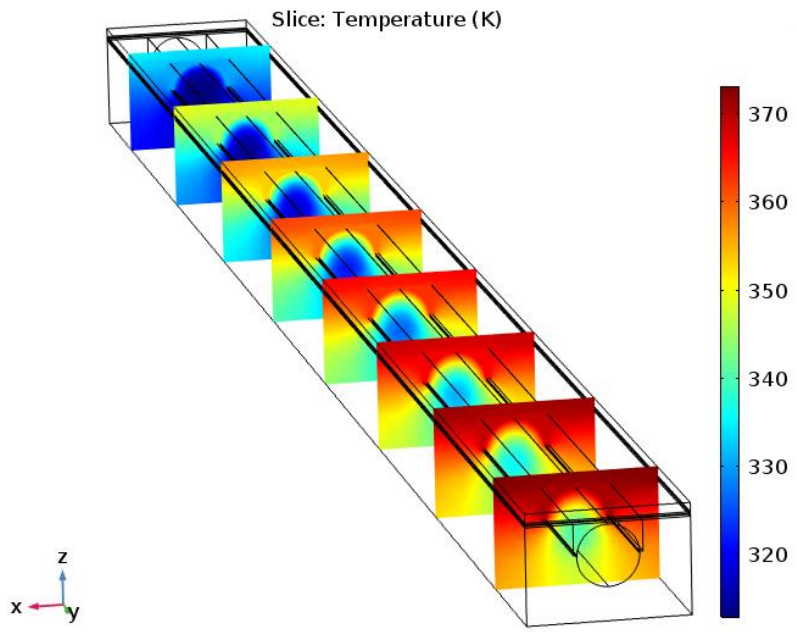

Figure 4.16. Temperature profile of the insulation and the working fluid

In addition, Figure 4.17 shows a detailed temperature profile of the tube outlet:

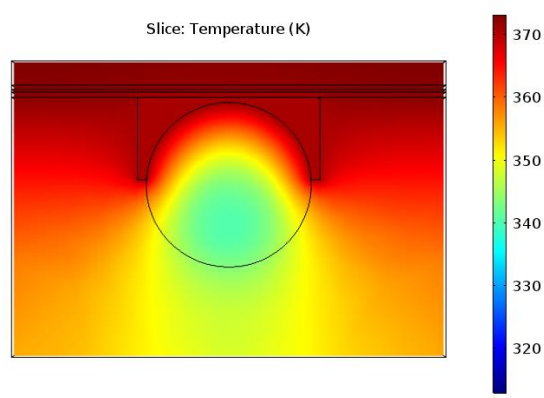

Figure 4.17. Temperature profile of the outlet

As shown in Figure 4.17, we do not have an even temperature distribution at the tube outlet. Thus, we calculate the average temperature at the tube outlet to be 353.35 K. The expected temperature at the outlet was set to be 80.46 °C (or 353.61 K), which is close to the temperature of the simulation. In order to verify the CFD solution, a mesh independency analysis is done on described model and the results are shown in the table below:

Table 4.5. Mesh independency analysis for the CFD model

Number of mesh	Quality	Average outlet temperature [K]
1,847,632	Normal	353.67
2,454,828	Fine	353.43
3,699,079	Finer	353.35
4,897,920	Extra Fine	353.15
5,239,261	Extremely Fine	353.16

We conclude that the analytical solution is accurate and can predict the minimum length of the tube for the one phase region (subcooled region). The application, based on COMSOL® Multiphysics, is built to help others set the desired parameters and find temperatures without needing to explore the setting details. Some pictures of the application interface are provided in the Appendix B. The application can help anyone, even those without knowledge of CFD simulations, to choose the properties for the insulation, tube, and working fluid, and determine the temperature distribution of the fluid and panel.

Using the same approach, as explained in equation 4.36, the length of the tube for the saturated region can be calculated. The data in Table 4.6 shows the total length of the tube needed to convert all the working fluid to the saturated vapor:

Table 4.6. Total length of the tube for the assumed working parameters ($\dot{m}$ =0.00397 kg/s)

		Tube Diameter (in.)											
		1/8	**1/4**	**3/8**	**1/2**	**5/8**	**3/4**	**1**	**5/4**	**1/8**	**3/2**	**5/2**	**3**
Tube Distance (cm)	**5**	3.03	2.88	2.79	2.73	2.68	2.64	2.58	2.54	2.52	0.00	0.00	0.00
	10	4.46	4.14	3.95	3.80	3.67	3.55	3.36	3.21	3.08	2.89	2.77	2.71
	15	6.97	6.44	6.12	5.86	5.63	5.44	5.09	4.80	4.55	4.14	3.84	3.60
	20	8.26	7.62	7.23	6.92	6.65	6.40	5.98	5.62	5.32	4.80	4.40	4.08
	25	10.29	9.50	9.01	8.61	8.28	7.97	7.44	7.00	6.61	5.96	5.45	5.03
	30	13.72	12.65	12.00	11.48	11.03	10.62	9.92	9.32	8.80	7.94	7.25	6.69

As shown in Table 4.6, the minimum length of the tube is more than 2 m, the length of the photovoltaic panel, so a decision must be made for reaching the desired temperature in the space that is available in one panel. Although another panel may be added in series with the first panel, this method will decrease the efficiency of the panel since the flow in the second panel will have a higher temperature and will absorb less energy from the second panel. In other words, the cooling efficiency of the panel will be dramatically decreased because of the higher fluid temperature.

To address this issue, the mass flow rate must be modified to ensure that the two-meter length of tube is sufficient to increase the temperature. The lower total mass flow rate can be compensated by adding more panels.

Considering that R-245-fa is an isentropic fluid and superheating is not needed, we can find the proper mass flow rate from the algorithm mentioned in Figure 4.9. By considering a 0.003 kg/s mass flow rate instead of the initial mass flow rate (0.00397 kg/s), the minimum tube length would be 1.98 m, which is less than the length of the panel. The complete results with the new length are shown in Table 4.7:

Table 4.7. Total length of the tube for the modified mass flow rate ($\dot{m}$ =0.003 kg/s)

		Tube Diameter (in.)											
		1/8	**1/4**	**3/8**	**1/2**	**5/8**	**3/4**	**1**	**5/4**	**3/2**	**2**	**5/2**	**3**
Tube Distance (cm)	**5**	2.29	2.18	2.11	2.06	2.02	1.99	1.95	1.92	1.91	0.00	0.00	0.00
	10	3.37	3.13	2.98	2.87	2.77	2.69	2.54	2.42	2.33	2.18	2.10	2.05
	15	5.27	4.87	4.62	4.43	4.26	4.11	3.85	3.63	3.44	3.13	2.90	2.72
	20	6.24	5.76	5.46	5.23	5.02	4.84	4.52	4.25	4.02	3.63	3.33	3.08
	25	7.78	7.18	6.81	6.51	6.25	6.02	5.63	5.29	4.99	4.51	4.12	3.80
	30	10.37	9.56	9.07	8.67	8.33	8.03	7.49	7.04	6.65	6.00	5.48	5.05

Based on the results from the algorithm, different options may be used in the system. Here, we decided to choose a 3/4 in tube for the thickness since this is less than the others, and the possible thermal resistance of the tube will be less. The other diameters greater than 3/4 could also have been chosen for the system.

4.3.3 Analyzing the Performance of the System for Real Data

With the design parameters defined in the previous section to analyze the performance of the system, real data for Egypt, which had been experimentally measured [39], was used in the present work. The variation in solar radiation is shown in Figure 4.18:

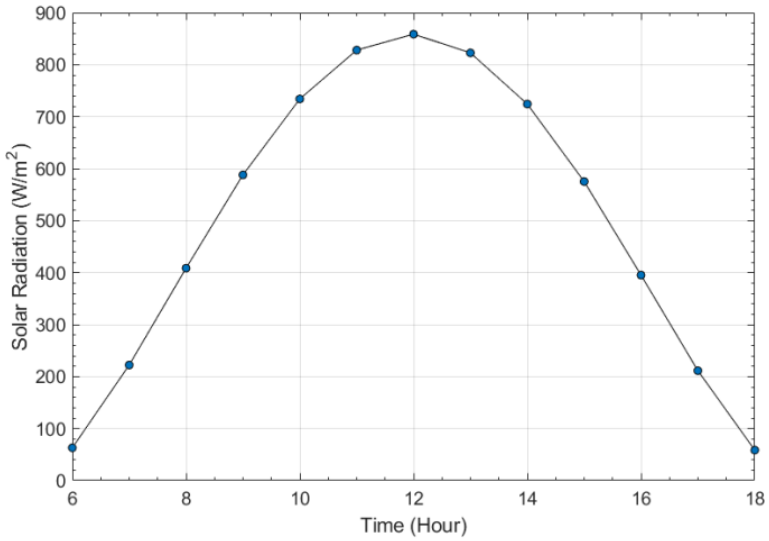

Figure 4.18. Variation in solar radiation with time [39]

Because the ambient temperature changes throughout the day, the variation in ambient temperature was also considered in the present study (Figure 4.19):

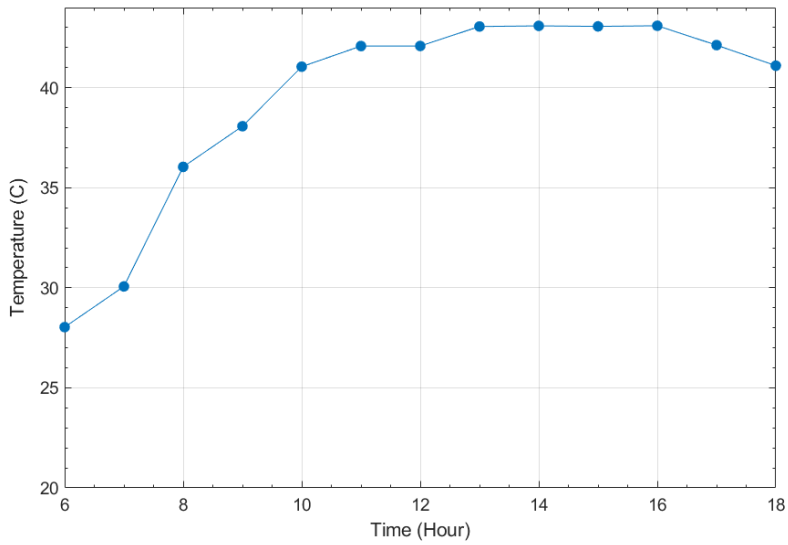

Figure 4.19. Variation in ambient temperature with time [39]

The algorithm in Figure 4.10 was used for the variations in temperature and solar radiation, and the final temperature for the photovoltaic panel and the heat loss coefficient was determined. The results of the different iterations are shown in Table 4.8:

Table 4.8. Final value for PV temperature and heat loss coefficient for the specific ambient temperature and solar radiation

			First Iteration		2nd Iteration		3rd Iteration		Final Temperature	Final Heat loss coefficient
$Hour$	T_a[°C]	$S[\frac{W}{m^2}]$	T_P[°C]	$U_L[\frac{W}{m^2K}]$	T_P[°C]	$U_L[\frac{W}{m^2K}]$	T_P[°C]	$U_L[\frac{W}{m^2K}]$	T_P[°C]	$U_L[\frac{W}{m^2K}]$
8	36.04	408.6	55	5.93	77.95	6.49	75.36	6.39	**75.80**	**6.39**
9	38.07	588.0	85	6.66	92.57	6.83	91.59	6.81	**91.70**	**6.81**
10	41.05	734.1	105	7.14	104.83	7.13	104.90	7.14	**104.83**	**7.14**
11	42.08	828.0	110	7.26	112.93	7.33	112.43	7.31	**112.57**	**7.31**
12	42.08	858.7	120	7.48	113.99	7.35	114.92	7.37	**114.78**	**7.37**
13	43.05	822.7	130	7.72	110.11	7.27	113.12	7.34	**112.63**	**7.34**
14	43.09	724.3	120	7.49	103.34	7.12	105.60	7.16	**105.35**	**7.16**
15	43.06	575.2	110	7.27	91.80	6.86	93.89	6.91	**93.63**	**6.91**
16	43.09	395.2	80	6.6	78.71	5.48	83.68	6.68	**78.41**	**6.68**

With the defined heat loss coefficient and the plate temperature, for different ambient temperatures and solar radiations, the simulation was conducted on the collector to see the effect of cooling on the performance of the photovoltaic panel. For the panel, equation 4.44 was used to determine the efficiency [6]:

$$\eta_c = \eta_{ref}\left[1 - \beta_{ref}\left(T_P - T_{ref}\right)\right] \qquad 4.44$$

where η_{ref} is the reference efficiency and equal to 0.178, β_{ref} is 0.00375, and the reference temperature is 25℃. The results of these simulations were compared to the efficiency of the panel without cooling (Figure 4.20):

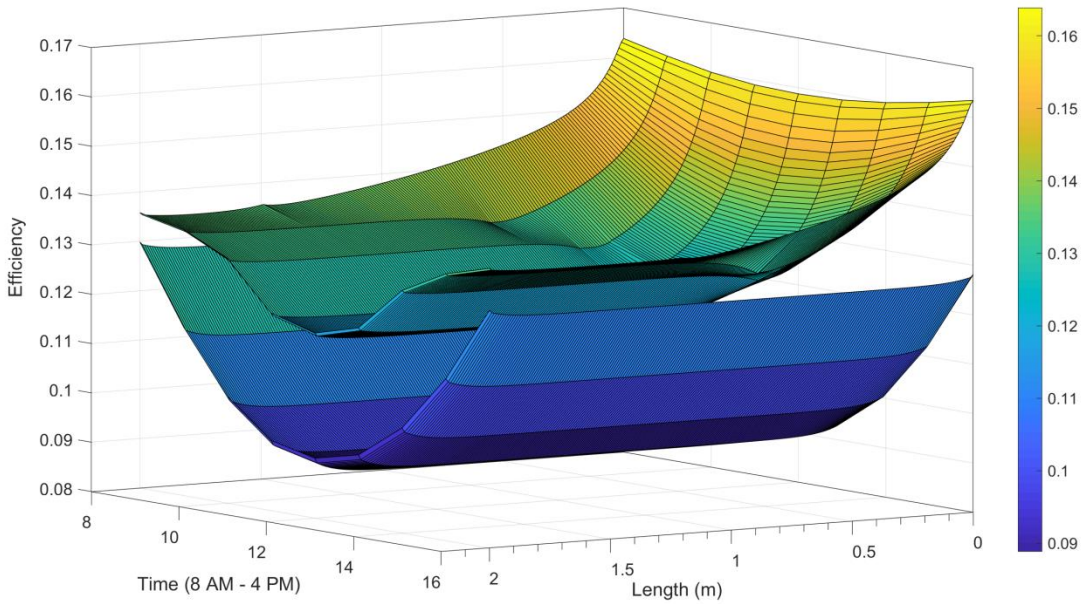

Figure 4.20. Efficiency graph for the PV panel with and without cooling. Top surface: with cooling tube; Bottom surface: without cooling

As shown in Figure 4.20, at the inlet side, where the temperature of the fluid is low, the maximum cooling is applied, which keeps the efficiency at about 16%. As the fluid passes through the tube, it gradually absorbs the heat and the temperature of the fluid increases, so less heat can be absorbed, and the efficiency drops to 13%. Although this part of the panel has a lower efficiency, compared to the system without a cooling tube, it still has a higher efficiency. The total power saved by using the cooling tubes can be calculated from equation 4.45:

$$P_{saved} = \sum_{i=8}^{16} \sum_{j=1}^{200} (\eta_{tube,ij} - \eta_{w/o\ tube,ij}) \times S_i \times 0.01 \times 1 \qquad 4.45$$

where i indicates the time interval, j indicates the length interval at the panel, which is set to be 1 cm here, η_{tube} and $\eta_{w/o\,tube}$ are the efficiencies of the panel with and without the added tube, S_i is the solar radiation, and A is the surface area of the panel, which is assumed to be 2 $m^2(2 \times 1\,m)$. The total power that can be saved for the specific data presented here would be 323.3 W for one day for one panel. For example, for 10 panels over 100 efficient working days, the total saved power would be 323 kW, which is significantly high. Detailed data for the power saving for different time intervals is presented in Figure 4.21:

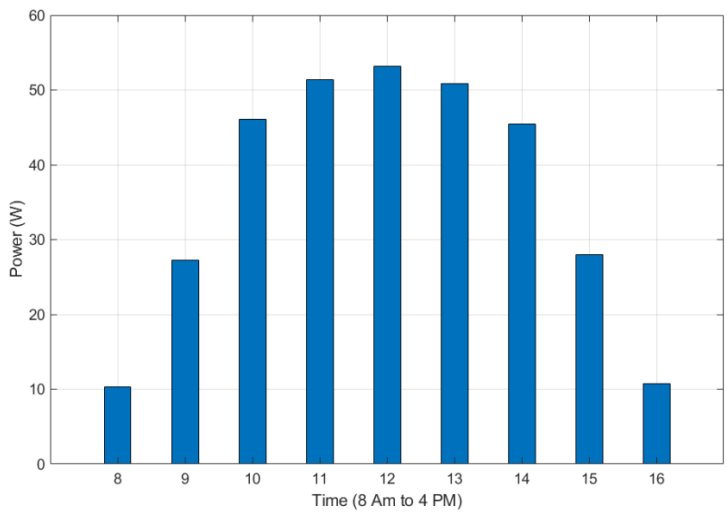

Figure 4.21. One-day power savings for one panel using a cooling tube

It must be noted that for the radiation and the ambient temperature mentioned in Table 4.7, the algorithm in Figure 4.11 can be used in order to find the minimum length of the tube which is necessary to have in order to reach the designed temperature of the cycle. Table 4.8 shows the minimum length required to increase the temperature of the working fluid:

Table 4.9. Minimum length of the tube which is required to run the Rankin cycle

			4th iteration (from Table 4.7)		Minimum length in the sub-cooled region	Minimum length in the saturated region	Total minimum length required length
$Hour$	T_a[°C]	$S[\frac{W}{m^2}]$	T_P[°C]	$U_L[\frac{W}{m^2K}]$	$L1_{min}$ $[cm]$	$L2_{min}$ $[cm]$	$L_{tot-min}$ $[cm]$
8	36.04	408.6	75.80	6.39	148.00	746.00	894.00
9	38.07	588.0	91.70	6.81	70.00	218.00	288.00
10	41.05	734.1	104.83	7.14	50.00	134.00	184.00
11	42.08	828.0	112.57	7.31	42.00	109.00	151.00
12	42.08	858.7	114.78	7.37	40.00	103.00	143.00
13	43.05	822.7	112.63	7.34	42.00	108.00	150.00
14	43.09	724.3	105.35	7.16	50.00	132.00	182.00
15	43.06	575.2	93.63	6.91	70.00	199.00	269.00
16	43.09	395.2	78.41	6.68	120.00	507.00	627.00

As it is shown in Table 4.8, only in the time between 10 Am to 2 PM the minimum length of the tube is less than 2 meter (the length of PV panel), so the final designed temperature for the Rankin cycle can be achieved. Thus, it is concluded that the cycle can be run only in this period.

In order to check the accuracy of the algorithm discussed in Figure 4.11, for all the radiation and the ambient temperature from 10 AM to 2 Pm showed in Table 4.8, a CFD simulation was conducted. The results are shown in Figure 4.22:

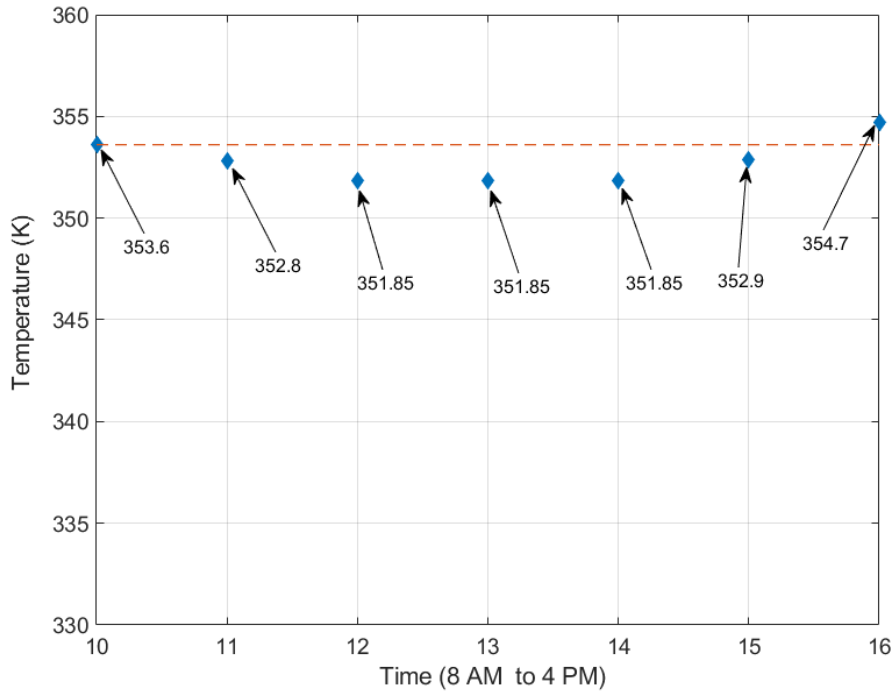

Figure 4.22. Compression of the outlet temperature of the tube with the designed temperature

As it is shown in Figure 4.22, the maximum temperature of 1.7 K divergence from the designed temperature is achieved from the algorithm which proves that the algorithm is working accurate enough for different solar radiation and ambient temperature and can be used for future designing purposes.

Chapter 5: Solar Cycle Expander (Turbine)

One of the main components of all the power generating cycle is the turbine. In the turbine, the momentum of the fluid will be transferred to the mechanical system and by using a generator, finally this energy will be converted into electricity. In the solar system that we are analyzing here, like all other Rankine cycle, it is necessary to choose the proper turbine. Freeman et al. [29] analyzed the organic Rankine cycle for the solar thermal collector; however, they have not mentioned anything about the type of the turbine they are going to use. The main challenge for choosing the turbine for the aforementioned cycle is the low flow rate. As it is mentioned in table 4.6, the flow rate which can be achieved by one panel is around 0.003 kg/s which is relatively low. In many cases, more panels are used on the roof of the houses and the number of the panels may vary between 8 to 10 panels. Even if we consider 10 panels for this cycle, the flow rate will reach to 0.03 kg/s, so a decision must be made to choose the proper system which is suitable for the low flow rate application.

Currently, there are two different types of turbine which are used in industry. The first type is "reaction turbine". Reaction turbines use the fluid pressure pushing on the turbine blades to produce motion. Kaplan and Francis turbine are two well-known reaction turbines. The other type of the turbine is "*Impulse turbine*" where in this system the fluids hit the blades causing it to turn as well as changing the fluid direction. Pelton turbine is one of the most famous impulse turbines.

Figure 5.1 shown below depicts different range of working condition for the typical turbines:

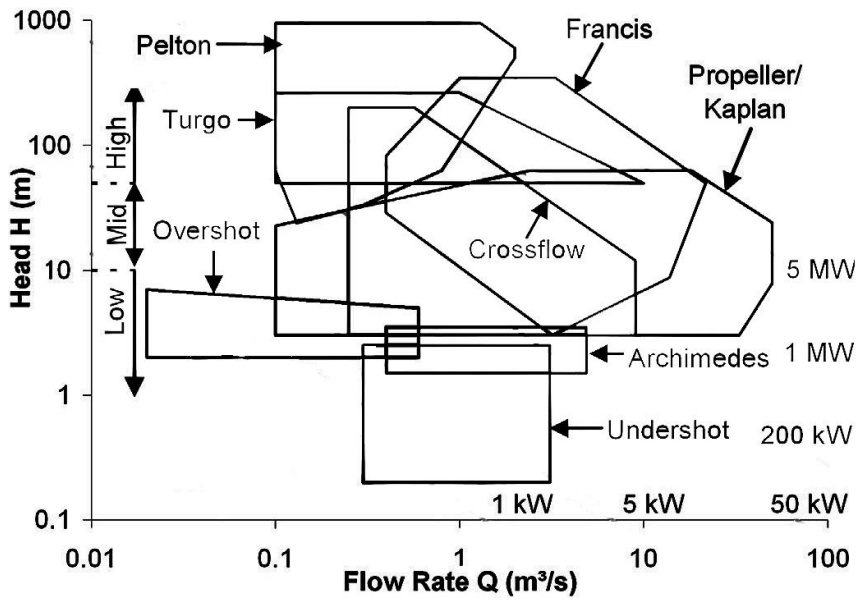

Figure 5.1. working conditions for different types of turbine [40]

As it is clear from the above figure, there is no turbine to cover the low flow rate region. One possible solution for this problem is to increase the number of panels, so the flow rate will increase, and it may then be in the range of the most common turbines' working condition; however, as it was mentioned before, the main purpose of this project is to generate more electricity for the residential purposes and with the minimum number of the panels. As a result, a complete literature review was conducted to find a suitable power generation device which can work under low flow rate condition. The answer to this question was found to be "*Tesla turbine*".

5.1 Tesla turbine

The Tesla turbine was patented in 1913 by Nikola Tesla [41]. Tesla argued in his patent that for high efficiency devices, changes in velocity and direction should be gradual. Tesla sought to design a device where the fluid was allowed to follow its natural path with minimal disturbance, both to increase efficiency and to reduce cost and complexity in the device. In this system, as shown in the Figure 5.2, the rotor of the turbine is consisted of several disks mounted on the shaft with a small gap in between. Close to the shaft, several exhaust holes are placed for the fluid flow. The fluid is injected to the space between the disk with a nozzle and will continue its way toward the inner part of the disk and will turn the shaft, finally.

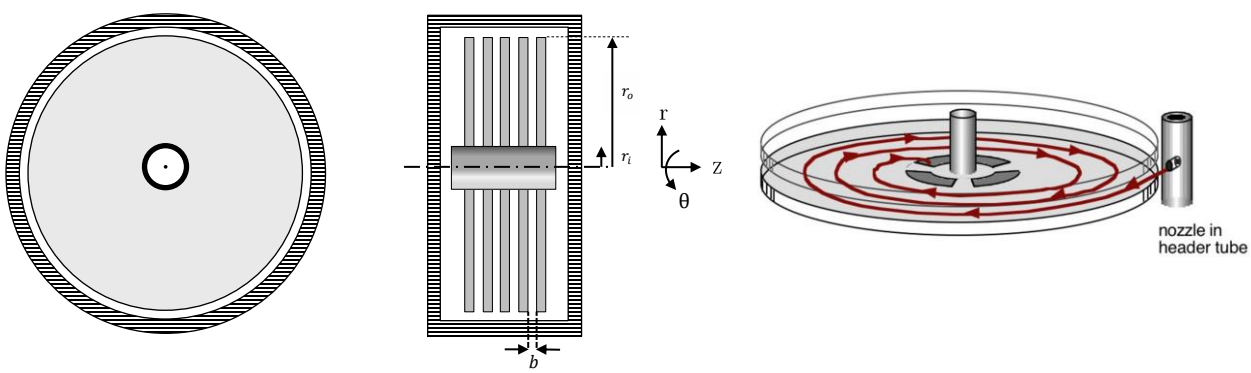

Figure 5.2. Schematic of the Tesla turbine and fluid flow between the disks

5.1.1 Literature review

In industry, typical turbines work on the principle of changing the momentum of the fluid with the turbine blades. Because of the complexity, designing blades for conventional

turbines is time-consuming and costly. The "Tesla" turbine can be used for slurry flow, such as the flow produced from biomass systems. It has also been suggested for use in geothermal power generation cycles [42]. Sun [43] investigated the idea of using Tesla turbine for low flow rate application. In her research, she investigated using the Tesla expander in the solar thermal power system which is using a mirror to focus the light on the copper tube and evaporate the water to generate power. The possible use of this turbine for micro-dimension applications such as micro-powerplants, has been reviewed [44], [45]. A summary of the most relevant previous research is listed in Table 5.1:

Table 5.1 Summary of relevant previous work on the Tesla turbine

Author(s)	Year	Approach	Key notes
Batchelor	1951	Numerical	• Navier-Stokes equation reduced to ordinary differential equation • Solution was derived for the fluid in an infinite area
Stewarston	1953	Experimental-Numerical	• Flow between two coaxial rotating disks was solved
Rice	1965	Experimental-Numerical	• Start working on Tesla turbine • The efficiency of the turbine was measured • One-dimensional analysis was conducted on Navier-Stokes equation
Beans	1966	Experimental-Numerical	• Different tests were conducted on Tesla turbine with different spacing and working pressure • Parabolic velocity profile was considered for the flow between disks • Qualitative agreement between the calculated and experimental performance was achieved.
Boyak and Rice	1971	Numerical	• An integral method was adapted for three dimensional, radially incompressible inward through-flow • It was concluded that by using polynomial of order 8, the results are close to what was obtained by finite difference method

Garrison et al.	1976	Numerical	• Using an integral solution for compressible and laminar flow
Lemma et al.	2008	Experimental -Numerical	• Three-dimensional simulation of the complete rotating parts of Tesla turbine was conducted
Hoya and Guha	2009	Experimental	• Working on "acceleration method" to measure the torque of the Tesla turbine
Carey	2010	Numerical	• One dimensional model was developed for the flow between the disks • An analytical solution was derived for the proposed model • The possibility of using Tesla turbines for solar cycles was reviewed
Podergajs	2011	Numerical	• Quadratic terms for radial and tangential velocities in Navier-stokes equation were ignored with no experimental validation in order to find analytical solution
Lampart and Jędrzejewski	2011	Numerical	• Using ANSYS FLUENT® for 2D and 3D simulation of the disk
Romanin	2012	Experimental-numerical	• Using integral solution scheme and developing a dimensionless perturbation series solution • Simulation was also conducted for two-dimensional laminar flow assumption using ANSYS FLUENT®
Sengupta and Guha	2012	Numerical	• Systematic order of magnitude analysis was conducted to neglect some terms in Navier-stokes equation • Analytical solution was derived • Results were compared with previous experiments done by other researchers
Schosser, et al.	2017	Analytical-Numerical	• Flow equation was solved for rotating disks with parabolic profile for the flow between the disks • CFD simulation was conducted for one rotating disk

The performance and nature of the fluid in Tesla turbines has motivated many researchers to work in this field. Analyzing the dynamics of the flow between disks in an infinite area filled with a fluid has been a research topic of interest for several decades [38], [46]. Although the analytical solutions have provided insight into how the fluid flows over the

disks, they have not accurately described fluid fields in Tesla turbines, which are comprised of disks with a finite radius.

Rice built a mathematic model specifically for a Tesla turbine. Six turbines were built, and two of them were thoroughly discussed in the paper. Various nozzle angles were tested, but the performance was found to be similar. The conclusion was that the operating parameters were not close to those indicated by the analyses to achieve optimum turbine efficiency. The model was a compromise between an accurate description of the problem and manageable results [47]. In another modeling, a theoretical and experimental investigation were carried out on the Tesla turbine. For the fluid flow analysis, a parabolic velocity profile for the flow between the disks was assumed. The theoretical approach implied a linear relationship between torque and angular velocity for incompressible laminar flow. Compressed air was used as the working fluid. Various disc spacings (0.500, 0.237, 0.105, 0.061, 0.037, and 0.026 in.) and supply pressures (10, 20, 30, 40 psig) were tested, with the other dimensions kept the same. The calculated and experimental curve showed general agreement but the calculated results in most cases were less than the experimental results [48].

Other mathematical solutions, such as an integral series, were also implemented to predict the performance of the Tesla turbine. Using a polynomial of the order 8, the results of the solution were found to be close enough to the previous solutions from the finite difference methods [49]. In other research, this approach was combined with the compressible flow assumption for the flow between rotating disks [50].

Podergajs implemented a purely mathematical method to solve Navier-Stokes equations for Tesla turbines. In this research, quadratic terms for radial and tangential velocities were

ignored with no experimental validation [51]. To simplify the Navier-Stokes equations, a systematic order of magnitude analysis was conducted to neglect some of the terms, which finally led to an analytical solution [52]. Although their article was mainly theoretical, the authors compared their theoretical work to previous experimental results.

One of the possible applications for the Tesla turbine is in the organic Rankine cycle in combination with solar systems or other low-grade energy sources. Since the available energy in these systems is limited, the flow rate would also be lower than that of a typical power cycle. In this specific case, the Tesla turbine could be an ideal component for generating electricity in the low flow rate application. In other research, a new model was developed to find some unique parameters, such as mechanical and isentropic efficiencies to analyze a solar Rankine cycle. Different assumptions were made to find the analytical solution, which allowed parameters like radial and tangential velocity to be presented in the form of analytical functions. With the ideal one-dimensional momentum equation, the author found that an isentropic efficiency of 75% can be achieved [53].

A number of studies were conducted, where Tesla turbines were modeled using ANSYS FLUENT®. In the first 2D model, the clearance between the nozzles and disks was not considered. Different numbers of nozzles (2, 4, or 6) and two inlet angles (10 and 15 degrees) were considered. The authors concluded that increasing the rotational speed will increase the efficiency. For the second model, the analysis was done on the 3-D model, which resulted in a lower efficiency [54].

In another study, both analytical and numerical analyses were conducted, and the researchers focused on the flow and momentum transfer inside the Tesla turbine under a laminar flow condition. Parabolic velocity variations and compressible flow was assumed.

Since the turbine experiences both radial and tangential stresses, the analysis was able to find the maximum rotational speed for the disks [55].

Romanian attempted to solve the Navier-Stokes equations using an integral solution scheme and developed a dimensionless perturbation series solution. All parameters were considered in the Navier-Stokes equation, which allowed the author to directly assess the importance of various parameters such as viscosity and pressure effects. Two different Tesla turbines (cm-scale and mm-scale turbines) were used. Since the torque of the system for a mm-scale turbine was too low, the "acceleration method" [56] was used to determine the torque. A simulation with ANSYS FLUENT® with a laminar flow assumption was also conducted [57].

One of the main challenges in analyzing Tesla turbines is to determine the flow regime. Based on the literature, no unique way exists for determining the flow regime in this system. Different researchers have defined different characteristic lengths to find a Reynolds number for the fluid; however, a complete instability analysis may be needed to find the range of Reynolds numbers in which transition of the flow regime will occur. As mentioned in the Handbook of Turbomachinery [58], the visco-geometric number can characterize the flow regime in the Tesla turbine [59]. This number is defined based on the known parameters of the system $\left(\frac{\widetilde{v_r} b^2}{\nu\, r}\right)$, where $\widetilde{v_r}$ is the relative velocity of the fluid in the radial direction, b is the distance between disks, and ν is the kinematic viscosity of the fluid. Nendl proposed that if the visco-geometric parameter is more than 10, then the fluid flow is turbulent, and if it is less than 10, the flow regime is laminar. Because decreasing the radius will decrease the area of the fluid flow and then dramatically increase the radial velocity, an increase in the Nendl number would be expected, which would eventually cause the fluid regime to become a turbulent flow.

Most of the previous research has been focused on one particular approach or assumption to determine the performance of Tesla turbines. Nevertheless, many testing conditions may not have been accurately related to the theoretical assumptions presented in the work. Therefore, an estimation of accuracy from different approaches and assumptions would be necessary to determine which approach is more accurate in predicting important parameters such as torque.

5.1.2 Objectives

The purpose of the present chapter is to compare different assumptions, mathematic models and computer simulation with experimental results from a Tesla turbine. We intend to find the simplest way to model a Tesla turbine with the highest accuracy. Also, it is intended to find the error associated with other models in order to add a correction factor to the models for the future use in the cycle analysis. The result of this endeavor could be used in the future modeling of a combined solar system where Tesla turbine could be one possible component for generating the power.

5.2 Mathematical modeling of Tesla turbine

As it was discussed in the literature review section, many researchers tried to model Tesla turbine to predict some of the main important parameters of the system. In this section, two main important models which were proposed by Carey [53] and Rice [47] are reviewed and a new parametric analysis on the torque is added to these model to compare the results with the experiment

5.2.1 Modified Carey's method

The model was developed by Carey [53], relying on the same basic assumptions, though further simplifications were not done to derive all the equations in the dimensionless form. In addition, a new equation is added to this model to calculate torque. A cylindrical coordinate is chosen to model the Tesla turbine (Figure 5.3). The assumptions listed below are made to simplify the equations:

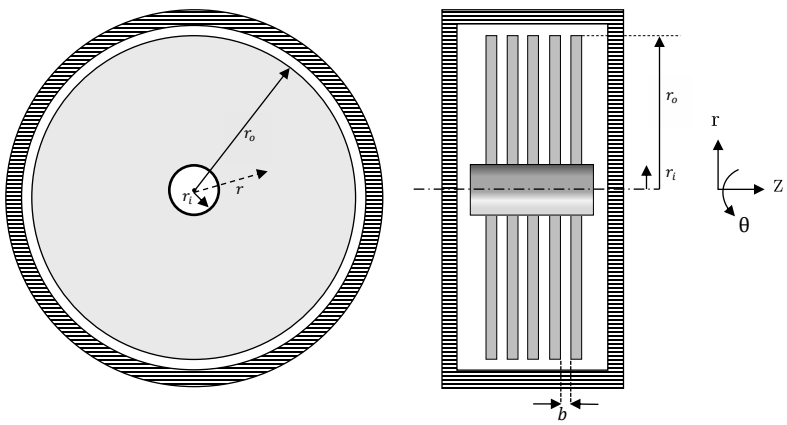

Figure 5.3. Schematic view of the turbine with the defined axis direction

1. The axisymmetric condition is assumed for the analysis, so that all of the derivative terms with respect to θ will disappear in the NS equations.
2. Due to the small gap between the disks, the velocity and pressure gradient in the Z direction is assumed to be negligible. The only velocity terms in the NS equations are v_r (radial velocity) and v_θ (tangential velocity).
3. The fluid (air) is assumed to be inviscid, so the viscosity term on the right-hand side of NS is neglected. Only the shear stresses on the disk surfaces are assumed to be effective and are used in the NS equation as body force.

4. Mass flow rate in the system is constant, and there is no leakage in the system.

Using the assumptions mentioned above, the simplified version of NS equations becomes

$$\frac{1}{r}\frac{\partial(rv_r)}{\partial r} = 0 \tag{5.1}$$

$$v_r\frac{\partial v_r}{\partial r} - \frac{v_\theta^2}{r} = -\frac{1}{\rho}\left(\frac{\partial P}{\partial r}\right) + f_r \tag{5.2}$$

$$v_r\left(\frac{\partial v_\theta}{\partial r}\right) + \frac{v_r v_\theta}{r} = f_\theta \tag{5.3}$$

Using conservation of mass, the following equation can be used to find the radial velocity (v_r)

$$2\pi r v_r b\rho = \dot{m} \Longrightarrow |v_r| = \frac{\dot{m}}{2\pi r b\rho} \tag{5.4}$$

Where b is the distance between two adjacent plates in the system, and ρ is the density of the fluid. Since the velocity vector is in the negative r axis direction, it can be defined in the form of:

$$\overrightarrow{v_r} = -\frac{\dot{m}}{2\pi r b\rho}\,\hat{r} \tag{5.5}$$

As b is much smaller than the radius of the plates, the system can be approximated with a parallel channel that has a fluid flow inside. To describe the friction in the NS equation, the wall shear stress acting on the fluid element is used. The θ direction component of the shear force is given by the following equation:

$$F_\theta = \tau_w A_w \tag{5.6}$$

Since all forces in NS equations are in the form of volumetric force, F_θ must be divided by the volume of the fluid in the channel to obtain the volumetric shear force:

$$f_\theta = \frac{F_\theta}{\rho \mathrm{V}_f} = \frac{\tau_w A_w}{\rho \mathrm{V}_f} = 4\frac{\tau_w}{\rho D_h} \qquad 5.7$$

Where V_f is the volume of the fluid between two plates, A_w is the wetted area between the plates, and D_h is the hydraulic diameter, which is defined as:

$$D_h = \frac{4\mathrm{V}_f}{A_w} = \frac{4 \times \pi \times (r_o^2 - r_i^2) \times b}{2 \times \pi \times (r_o^2 - r_i^2)} = 2b \qquad 5.8$$

Now, with the one-dimensional channel flow assumption, the shear stress on the wall can be evaluated as:

$$\tau_w = \frac{1}{2}\rho f \widetilde{v_\theta}^2 \qquad 5.9$$

In this equation, f is the friction factor. It should be noted that $\widetilde{v_\theta}$ is the velocity of the fluid relative to the rotating disk in θ direction ($\widetilde{v_\theta} = v_\theta - r\Omega\,, r\Omega = U$). As mentioned before, one-dimensional assumption is made here, so the velocity in θ direction is used in the equation above. For the friction factor between two parallel channels, if we assume the flow is laminar and fully developed, the following equation can be used to find the friction factor:

$$f = \frac{8\tau_w}{\rho V^2} = \frac{24}{Re} \qquad 5.10$$

In the above equation, the Reynolds number is equal to $Re = \frac{\rho \widetilde{v_\theta} D_h}{\mu}$. Equations 5.7, 5.9 and 5.10 can be combined to find the final expression for the volumetric shear force acting on a rotating disk

$$f_\theta = \frac{4\tau_w}{\rho D_h} = \frac{4(\frac{1}{2}\rho f \widetilde{v_\theta}^2)}{\rho D_h} = \frac{\frac{48}{Re}\,\widetilde{v_\theta}^2}{D_h} = \frac{48\mu\,\widetilde{v_\theta}}{\rho D_h^2} \qquad 5.11$$

Now, the volumetric shear force can be plugged into the NS equation (equation 5.3). It should be noted that since the friction force acts in the opposite direction, a negative sign is placed into the NS equation. Also, since it was assumed that there is no gradient in the fluid velocity in the θ and z direction, equation 5.3 can be replaced with the following differential equation.

$$v_r\left(\frac{dv_\theta}{dr}\right) + \frac{v_r v_\theta}{r} = -\frac{48\mu\,\widetilde{v_\theta}}{\rho D_h^2} \qquad 5.12$$

Substituting v_r in equation 5.12 with equation 5.4, the above equation becomes

$$\frac{dv_\theta}{dr} - \left(\frac{24\pi\mu r}{b\dot{m}} - \frac{1}{r}\right) + \frac{24\pi\mu r^2 \mu\Omega}{b\dot{m}} = 0 \qquad 5.13$$

And the proper boundary conditions for equation 5.13 is

$$at\ r = r_o\ , v_\theta = V_o \qquad 5.14$$

where V_o is the fluid velocity at $r = r_o$. Since we intend to use a Tesla turbine to drive an electrical generator, the available torque is a parameter of interest. To find an expression for the torque, we can start from equation 5.11; however, f_θ in this equation is in volumetric form and must be converted to the force on the surface of the elements

$$F_\theta = \frac{48\mu\widetilde{v_\theta}}{\rho D_h^2}\rho brdrd\theta \Rightarrow F_\theta = \frac{12\mu\widetilde{v_\theta}}{b}rdrd\theta \qquad 5.15$$

then, the torque can be calculated from the following equation:

$$\mathbf{T} = \int_{r_i}^{r_o}\int_0^{2\pi}\frac{12\mu(v_\theta - r\times\Omega)}{b}r^2drd\theta \qquad 5.16$$

Now, if we substitute the velocity profile that was found from equation 5.13 into equation 5.16, the torque on one disk can be calculated.

5.2.2 Rice's method

In this approach, the friction factor remains unknown and will be set manually based on the roughness of the surface or the fluid flow regime. The variable friction factor will turn the equations into a more complicated version of NS equations. It must be mentioned that all other assumptions are still the same as the first approach. To derive the NS equation, it is necessary to find the shear stress as a function of friction factor and velocity as stated below:

$$\tau = \frac{f\rho}{8}[(v_\theta - r\Omega)^2 + v_r^2] \qquad 5.17$$

Equation 5.21 can be multiplied by the surface area of the elements to find the shear force

$$f = \frac{2f\rho}{8}[(v_\theta - r\Omega)^2 + v_r^2]rd\theta dr \qquad 5.18$$

In the next step, since equation 5.18 represents the total shear force, we need to find the force component in the θ direction. The force component in the θ direction acting on the elements would be:

$$f = \frac{f\rho(v_\theta - r\Omega)}{4}\sqrt{[(v_\theta - r\Omega)^2 + v_r^2]}\, r d\theta dr \qquad 5.19$$

Now, the shear force found from equation 5.19 can be substituted into equation 5.3 so the final differential equation of motion for the system would be [47]

$$\frac{dv_\theta}{dr} + \frac{v_\theta}{r} = \frac{f\pi r\rho(v_\theta - r\Omega)}{2\dot{m}}\sqrt{(v_\theta - r\Omega)^2 + \frac{\dot{m}^2}{4\pi^2 r^2 b^2 \rho^2}} \qquad 5.20$$

The torque can be calculated by finding the force that is applied on the element of the fluid in the system:

$$\mathbf{T} = \int_{r_i}^{r_o}\int_0^{2\pi}\frac{f\rho}{4}\sqrt{[(v - r\Omega)^2 + v_r^2]}(v_\theta - r\Omega)r^2 dr d\theta \qquad 5.21$$

Substituting radial velocity from equation 5.5 into the above equation, the final expression for calculating the torque will be:

$$\mathbf{T} = \int_{r_i}^{r_o}\int_0^{2\pi}\frac{f\rho}{4}\sqrt{\left[(v - r\Omega)^2 + \left(-\frac{\dot{m}}{2\pi r b\rho}\right)^2\right]} \times (v_\theta - r\Omega)r^2 dr d\theta \qquad 5.22$$

5.3 CFD Simulation

To assess accuracy of theoretical solutions, CFD simulation is used to account for factors such as roughness of the disks and the flow regime in the analysis. Two different models were investigated using COMSOL®. First, we investigated a 3D model of one disk, as shown in Fig. 5.4 and we assumed that the flow will rotate one disc and will continue its way

toward the next disc and this process will continue until the fluid leaves the system. The 3D model is able to demonstrate the fluid flow on disk without having extra simplification like axisymmetric assumption, but it cannot model the mixture of the fluid in the exhaust holes between the disks.

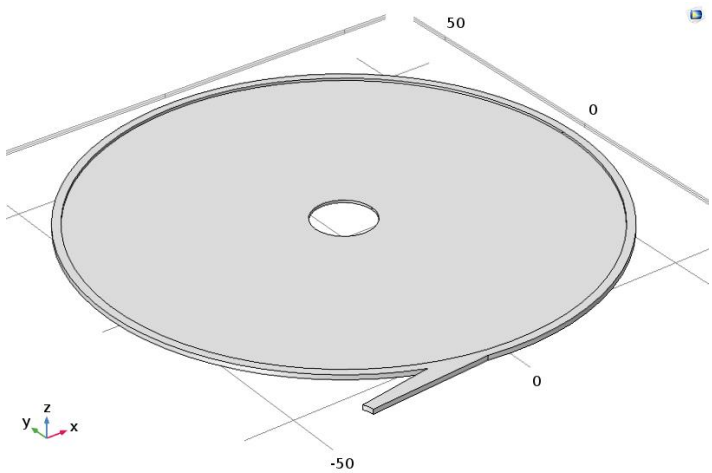

Figure 5.4. A 3D model showing inlet nozzle

Therefore, a 2D axisymmetric simulation is needed to consider the fluid interaction and mixture in the exhaust holes and between the disks. The benefit of using this simulation is that it simulates the whole system with the exhaust hole. Moreover, the simulation time is significantly less than the 3D simulation of the complete model [60]. More than 10 different configurations have been analyzed and simulated to find the best 2D model to describe the system. The most accurate models compare to the experiment are chosen, and the results are presented in this chapter. It must be noted that the size of the exhaust hole is constant in the real system; however, in the real system there are six 10 mm exhaust holes evenly distributed in a circular pattern around the shaft while in the 2D axisymmetric model these holes will be replaced by one hole at the center, so a conversion is made so that the hole in

the 2D axisymmetric model will have the same surface area as the six exhaust holes in the real system. The 2D model with different parts' names are shown below in Table 5.2.

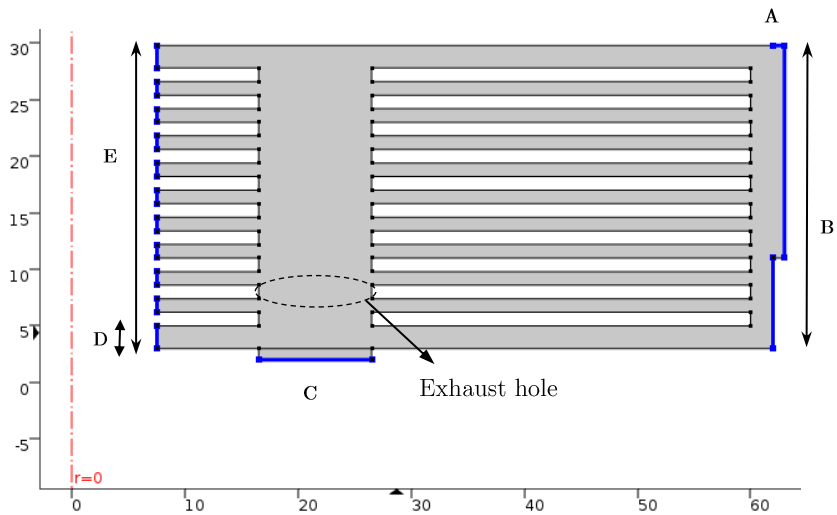

Figure 5.5. 2D simulation geometry

The most accurate models to predict the torque with their specification are listed in the table 5.2. In this Table on Model column, the first letter indicates the inlet, the second one shows the outlet, the third letter shows if there is an exhaust hole or not (Y: Yes, N: No), and the diameter of the exhaust hole is shown by the last number.

Table 5.2. List of 2D axisymmetric models and their specifications. To show different models on one figure, we will name each model in the form of "INLET-OUTLET- HAS EXHAUST HOLE OR NOT (YES/NO)- SIZE OF EXHAUST HOLE."

Model	Inlet	Outlet	Exhaust	Exhaust size [mm]
AC-Y-4	A	C	Yes	4
AC-Y-10	A	C	Yes	10
BE-N	B	E	No	-
AD-Y-4	A	D	Yes	4
AD-Y-10	A	D	Yes	10

5.4 Experimental setup

Since for Tesla turbine is not commercially available, to verify the accuracy of the CFD simulation and theoretical models with a real system, a Tesla turbine was built and tested. A detail specification of the Tesla turbine is listed in the Table 2:

Table 5.3. Specification of the turbine

Outer diameter of the disks	**0.12 [m]**	Inner diameter of the disks	**0.015 [m]**
Number of exhaust holes	**6**	Diameter of the Exhaust holes	**10 [mm]**
Disk thickness	**1.2 [mm]**	Disk gap	**1.2 [mm]**
Number of disks	**10**	Distance between disk tip and housing	**2 [mm]**

In order to build the turbine, a decision has been made to use the simple CD as a rotating disk. The benefit of using CD was that it was perfectly balanced and cheap for the initial tests. Total number of six exhaust holes have been drilled on the CDs. The main challenge in making the holes was that by using a simple drill, the temperature has been increased, so the CD was melted and was not suitable for using in the system. To fix this problem, wood drill was used to make circular holes in the CD.

In order to have a fix distance between the disks, a washer was designed and fabricated by using the water jet from the aluminum plate to make sure that the disks are placed in the right position.

The disks were connected to a 10 mm shaft made from 1055 carbon steel which was purchased from McMaster-Carr. The shaft was fixed into four single row ball bearings which was purchased from McMaster-Carr. Finally, the whole rotating system was placed in the housing made from acrylic sheet.

For the measurement system, different instruments have been used to measure the rotational speed, pressure and the flow rate of the system. In order to measure the rotational speed, an optical encoder has been implemented. Also, to connect the encoder to the computer and record data, an Arduino was used to convert the position into the rotational speed. Vertical mount variable-area flow-meter purchased from McMaster-Carr was implemented to measure air flow rate. Finally, to run the system, a compressor was needed to provide high pressure air for testing the system. Since during the test condensed water was entered the turbine which may have an effect on the performance of the system, a filter dryer was purchased and connected to the line to prevent having a condensed water in the pipe line. Figure below shows the schematic view of the test set up:

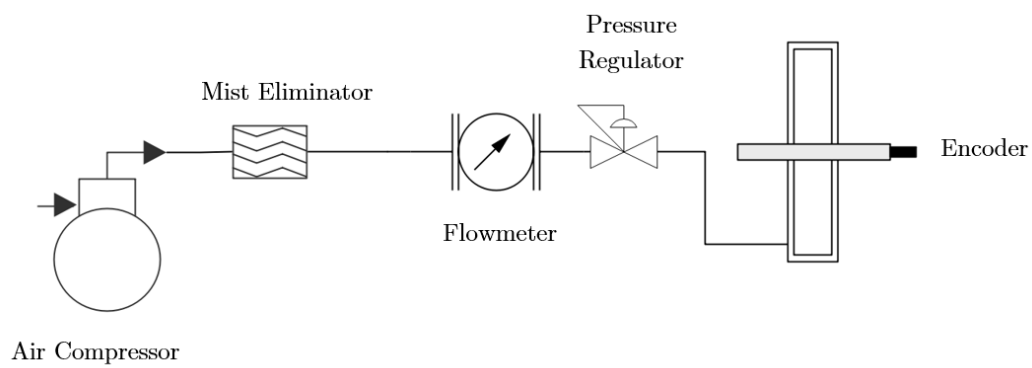

Figure 5.6. Schematic view of the experimental set up

Picture of different components are shown in the figure below

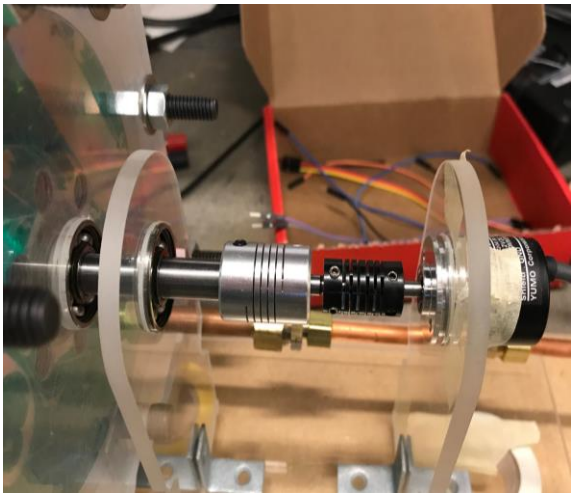

(a)

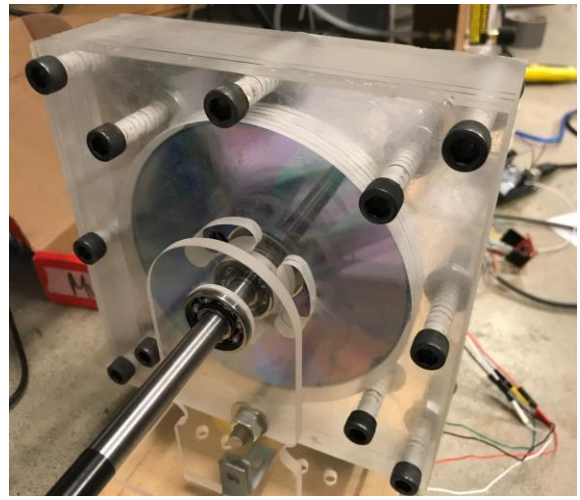

(b)

(c)

(d)

Figure 5.7. Different parts of the experimental set-up: (a) Close view of the encoder, couplings and ball bearing (b) Close picture of the housing shows the exhaust holes (c) Housing and connecting bolts (d) Picture of air compressor water filter

(a)

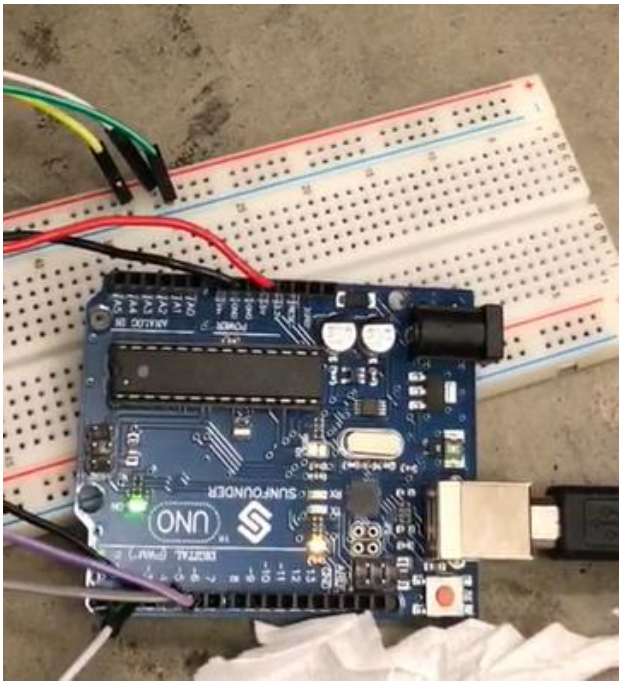

(b)

(c)

Figure 5.8. Different parts of the experimental set-up: (a) Compressor (b) Arduino to read data from encoder (c) Flowmeter

5.5 Torque measurement

There are different methods for measuring the torque in the rotating system such as using dynamometer, using floated turbine idea or connecting a generator to the turbine; however, since in this experiment the flow rate is low, the torque is not high enough to be measure by these common methods. For this reason, a decision has been made to use "acceleration method" which was proved to work for the low flow rate system [56]. The idea behind this method is based on the Newton's second law. The torque in the rotating system can be found form the following equation

$$\mathbf{T} = I\alpha \qquad \mathbf{5.23}$$

In equation 5.23, I is moment of inertia for the whole rotating system and α is angular acceleration which can be found numerically from the angular velocity. The important fact is that two different types of toque will influence the performance of the system. The first toque is due to the fluid flow which goes into the system and will turn the turbine, while the friction is the other type of the torque. Whenever, these two torques will be equal, the system will reach steady state and the acceleration of the rotor is zero. The strategy to measure the friction torque is to run the turbine and wait untill the system reaches steady operation and then the inlet flow will be closed untill the rotor stops. When the inlet valve will be closed the only torque acting on the rotor is the friction torque. If we assume that the friction torque at the same speed is equal in acceleration and deceleration phase, following equations can be written for the system at known rotational speed

$$\mathbf{T}_{inlet-flow} - \mathbf{T}_{friction} = I\alpha_{acceleration} \quad \mathbf{5.24}$$

$$-\mathbf{T}_{friction} = I\alpha_{deceleration} \quad \mathbf{5.25}$$

If now we combine equation 5.24 and 5.25, we will end up with the following equation

$$\mathbf{T}_{inlet-flow} = I\alpha_{acceleration} - I\alpha_{deceleration} \quad \mathbf{5.26}$$

Since $\alpha_{deceleration}$ is a negative number, equation 5.26 can be rewritten in the following form

$$\mathbf{T}_{inlet-flow} = I\alpha_{acceleration} + I|\alpha_{deceleration}| \quad \mathbf{5.27}$$

In the experiment, the rotational speed was found from an optical encoder coupled to the shaft. Moment of inertia of the parts were estimated by geometric shape and using a CAD software (SolidWorks®) as presented in Table 5.4:

Table 5.4. Moment of inertia for all rotating components

Components	Moment of inertia $[\mathbf{gr.mm^2}]$	Number
Main shaft	1529.09	1
Base shaft for disks	466.07	1
spacer	142.79	9
Disks	13750.21	10
Total	**140782.37**	-

5.6 Results

The system was tested at two different flow rates. Also, during the tests, it was kept running for more than 1 minute to reach steady state before closing the inlet valve. The velocity variation for 2.2 and 2.4 SCFM are shown in the following graphs.

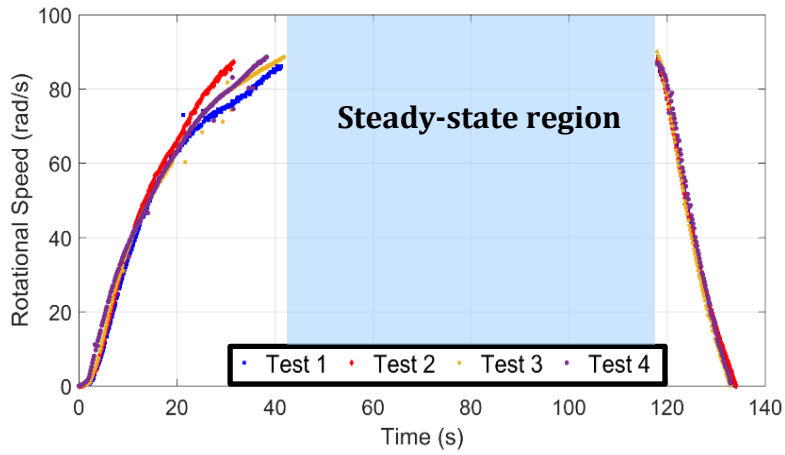

Figure 5.9. Rotational speed of the rotor for 2.2 SCFM flow rate.

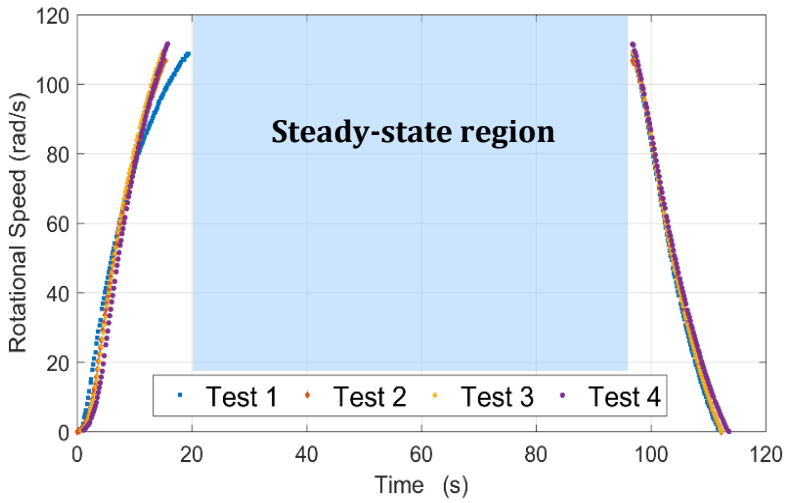

Figure 5.10. Rotational speed of the rotor for 2.4 SCFM flow rate

As it is clear from figure 5.8 and 5.9, the acceleration part has a lower slope in comparison with deceleration phase. Also, from figure 5.10 and 5.11, which are the zoomed view of Figs. 5.7 and 5.8, it is clear that all the tests have approximately the same slope and the steady-state rotational speed for 2.2 SCFM and 2.4 SCFM varies between 85 to 90 rad/s and 110 to 115 rad/s respectively.

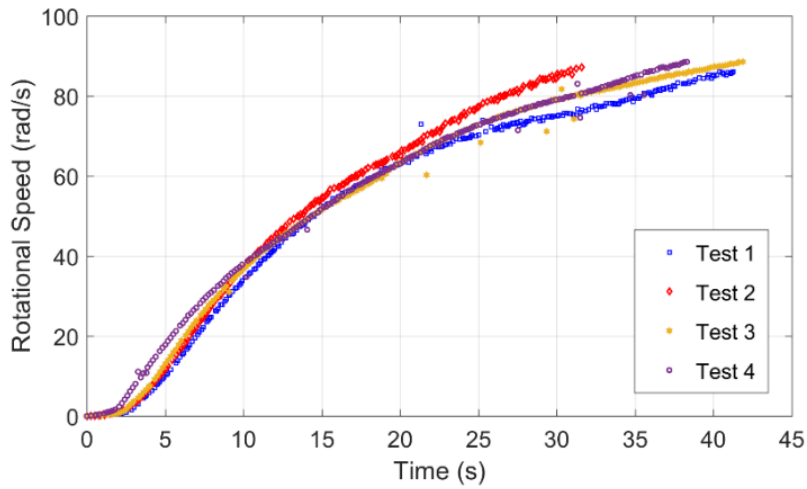

Figure 5.11. Zoomed view of the acceleration part of rotational speed graph for 2.2 SCFM

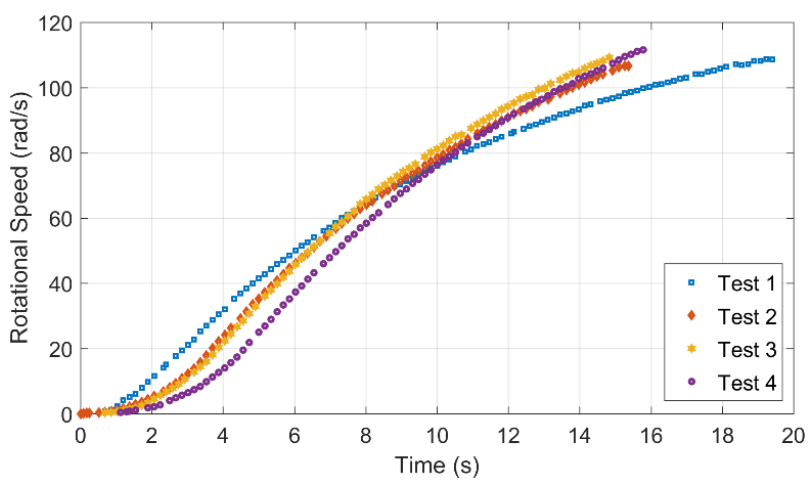

Figure 5.12. Zoomed view of the acceleration part of rotational speed graph for 2.4 SCFM

A 3rd or 4th order polynomials are fitted to the data and the derivative of the functions are found on the points with the same rotational speed. Using equation 5.27, the torque for the different tests for 2.2 SCFM flow rate is represented below

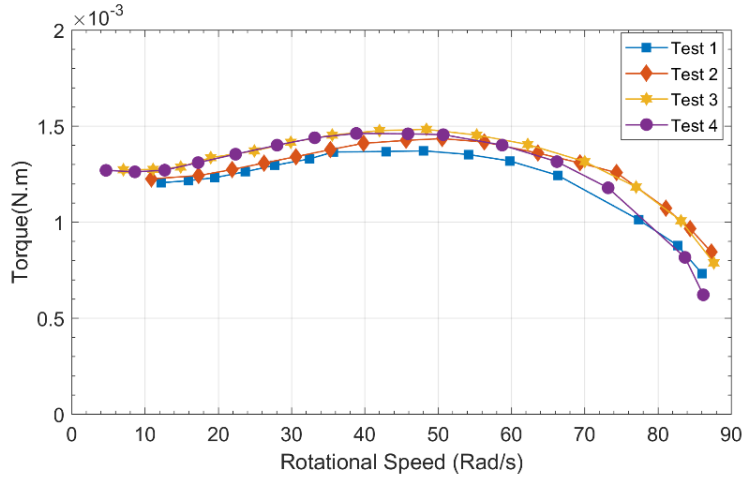

Figure 5.13. Torque-speed graph for 2.2 SCFM flow rate

The uncertainty analysis is conducted on all the tests (Appendix A) and the results for test 4, as an example, are shown in figure 5.13.

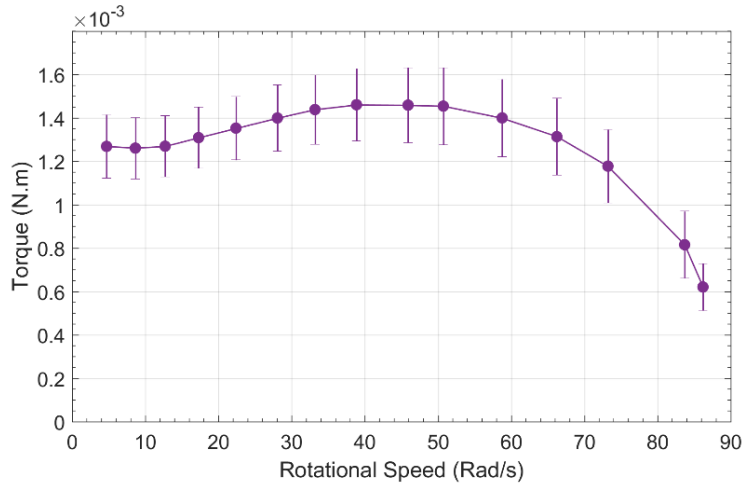

Figure 5.14. Torque-speed graph with uncertainty bar for the 4th test with 2.2 SCFM

The torque-speed graph for the test with 2.4 SCFM flow rate is depicted below. As it is clear the system reaches to its maximum torque in 62 rad/s and then the torque will decrease until it reaches to steady-state.

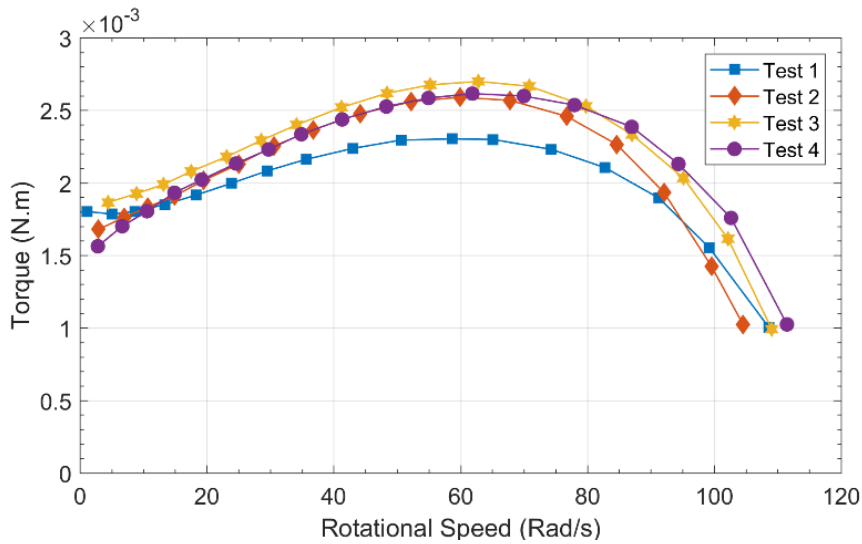

Figure 5.15. Torque-speed graph for 2.4 SCFM flow rate

The uncertainty bars for the data from test 2, as an example, are shown in Figure 5.15

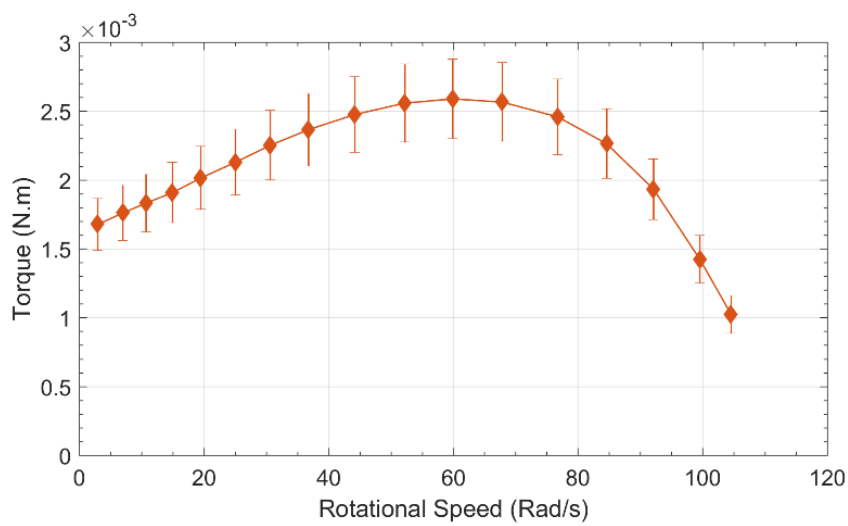

Figure 5.16. Torque-speed graph with uncertainty bar for the 2nd test with 2.4 SCFM

The torque from the mathematical modeling and simulations are calculated and the result are listed in the table below. It must be mentioned that the error in this table is defined in the following form:

$$Error = \frac{\left|\mathbf{T}_{exp.} - \mathbf{T}\right|}{\mathbf{T}_{exp.}} \qquad 5.28$$

Table 5.5. Results for the torque for 2.2 SCFM

		Torque (N.m)	Error±Uncertainty (%)
	Experiment	$(7.5 \pm 0.95) \times 10^{-4}$	-
Mathematical modeling	First Approach	3.38×10^{-4}	55±6
	Second Approach	3.36×10^{-4}	55±6
2D Simulation	AC-Y-4	4.72×10^{-4}	37±8
	AC-Y-10	4.97×10^{-4}	33±8
	AD-Y-4	4.64×10^{-4}	40±8
	AD-Y-10	4.89×10^{-4}	35±8
	BE-N	4.72×10^{-4}	37±8
	3D Simulation	4.49×10^{-4}	40±8

Also, the error for the torque measurement for 2.4 SCFM flow rate is listed in the table below

Table 5.6. Results for the torque for 2.4 SCFM

		Torque (N.m)	Error ±Uncertainty (%)
	Experiment	$(10 \pm 0.16) \times 10^{-4}$	-
Mathematical modeling	First Approach	5.66×10^{-4}	43±0.4
	Second Approach	5.46×10^{-4}	68±0.4
2D Simulation	AC-Y-4	6.55×10^{-4}	34±1
	AC-Y-10	7.97×10^{-4}	20±1
	AD-Y-4	7.42×10^{-4}	25±1
	AD-Y-10	7.84×10^{-4}	22±1
	BE-N	6.50×10^{-4}	35±1
	3D Simulation	6.95×10^{-4}	30±1

Table 5.5 and 5.6 indicate that the AC-Y-10 model has the best accuracy to predict the torque and consequently the power of the system. One possible reason for this improvement is the inclusion of the exhaust hole in the simulation. Also, it was observed that by increasing the rotational speed, the error has decreased from 33% to 20% error. Because of the assumptions which were made in the first and the second mathematical approaches, the error associated with them is still high and may contribute to significantly high error in the future calculations; however, these models are simple and easy to work with and can be used to obtain a first order of estimation. As it was discussed before, 2D axisymmetric model can demonstrate the vortexes and the fluid mixture in the exhaust hole. Figure 5.16 shows the streamline contours for AC-Y-10 model with the vortexes between the disk and holes.

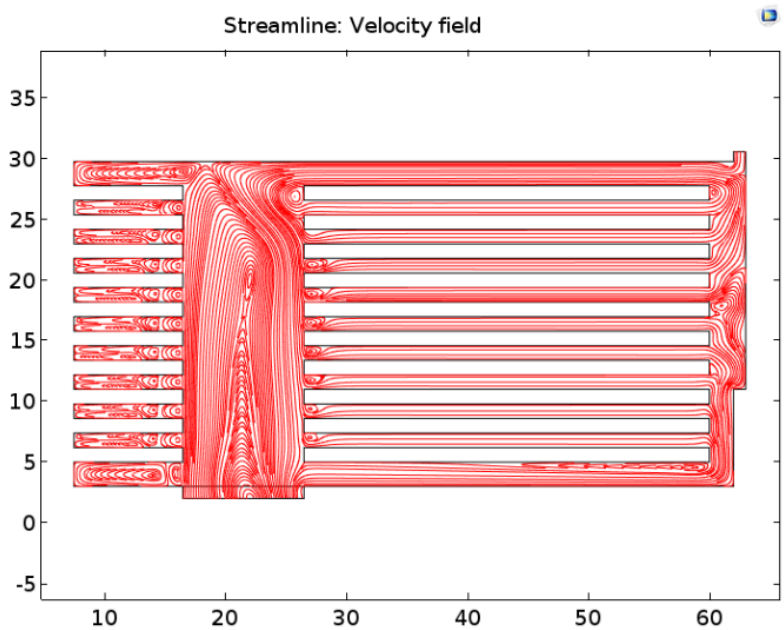

Figure 5.17. The streamline contour for the 2D simulation for AC-Y-10 model with 2.2 SCFM flow rate

In this part, to complete the cycle and predict the output power for this project, we decided to use the first approach (Modified Carey's method) with the correction factor found from the above results, as it can provide the write answer in a short time and it is prefect to be used for feasibility study.

5.7 Output power of the cycle

Now, with choosing the proper method to model the turbine, the amount of power which can be generated from the cycle can be determined. The table shown below is demonstrating the proper value for the properties of the working fluid in the cycle.

Table 5.7. Properties of the working fluid and turbine for the power analysis of the cycle

Fluid property at turbine inlet			
μ (Viscosity)	1.253×10^{-5} $[kg/(m.s)]$	$\dot{m}$ (Mass Flowrate)	0.003 $[kg/s]$
ρ (Density)	44.65 $[kg/m^3]$	P (Pressure)	800 $[kPa]$
Turbine properties			
N	9000 $[RPM]$	r_o (outer radius)	9 $[cm]$
b	1 $[mm]$		
Fluid property at pump inlet			
ΔP	550 kPa	ρ	1297 [kg/m^3]

It must be mentioned that for the mentioned pressure and mass flowrate, based on the literature review [53], the rotational speed was determined to be about 9000 RPM. This number is used here in the analysis of the turbine. The following figure shows the variation of the force acting on one disk of the turbine:

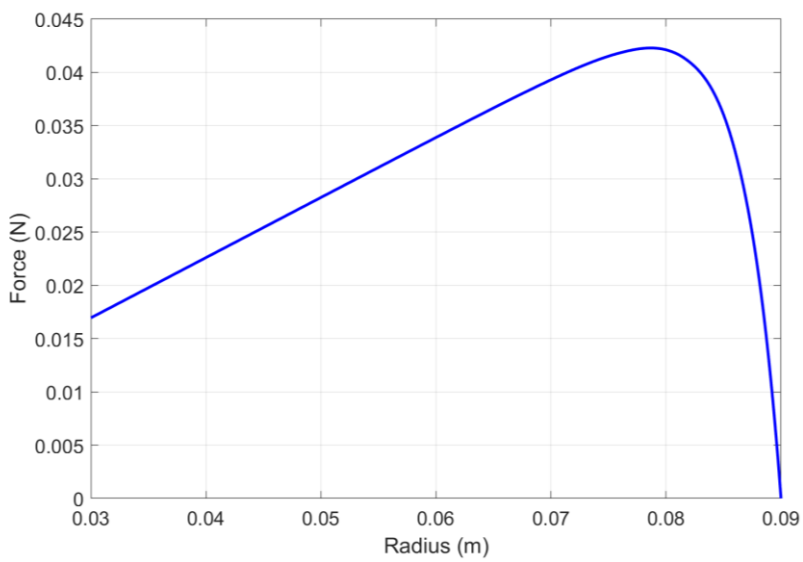

Figure 5.18. Variation of the force acting on one disk as a function of radius

Now, by integrating the force over the radius from the above figure, the total torque acting on one disk can be calculated. The final torque for one disk would be 0.0019 N.m. Now, to find the power generated by the turbine, the following equation can be used:

$$P = \mathbf{T} \times \omega \qquad \textbf{5.29}$$

Using the above equation, the total power for 10 disks would be equal to 17.5 W. As it was discussed before, the results of the first approach may include error and divergence from the real torque which we have for the system, so by using table 5.5 and 5.6, we can consider 1.4 as a correction factor for the results. Thus, the final power which can be achieved by using the Tesla turbine in this cycle would be about 24.5 W. This power is the output of the system from the turbine; however, we must also consider the power which was used by pump to increase the pressure. To determine the power which is needed for the pump, we can use the following equation:

$$P_{pump} = \dot{m} \times 1/\rho \times (\Delta P) \qquad \textbf{5.30}$$

where $\dot{m}$ is the total mass flowrate, ρ is the density and ΔP is the changing in the pressure of the fluid. Table 5.7 can be used to find all the above parameters. Substituting these parameters into equation 5.30, the input power for the pump would be 1.27 W, thus the net power which can be obtained from the turbine would be about 23.2 W. Thus, in a case that the radiation is enough, and the temperature is increased to the designed temperature, we expect that the system can increase the power by 23 Watt. Now, considering 80% efficiency for the generator, the final value for the output of the system is 18.4 Watt.

Chapter 6: Conclusion and Future Work

This work assesses a hybrid solar PV panel with Tesla turbine as an expander, focusing on three main aspects: the working fluid, solar panel cooling, and the turbine modeling.

For the working fluid, different fluids were investigated, and based on the parameters from Chapter 2, R245-fa was determined to be the best option. This fluid was analyzed in the Rankine cycle to find the optimal properties with regards to the fluid pressure, temperature, and flowrate.

In the proposed system, the PV panel works like a boiler in a Rankine cycle. A complete analysis of the PV panel was carried out. First, based on the method developed by Duffie and Beckman [28], important parameters like temperature distribution and heat transfer were calculated for the panel. A new algorithm was then developed to design the cooling system for the panel. This allowed for a prediction of the proper number of tubes and the distances between tubes in a short time. This method was also investigated by a CFD model to determine its accuracy. In addition, to check the results of the algorithm, real data from an experiment in Egypt was used. The CFD results showed that the maximum divergance from the desired temperature for the cooling system would be about 1.7 ℃. The small difference between the desired temperature and the actual temperature illustrated that the algorithm was sufficiently accurate to be used for designing the cooling system. Finally, the results of the CFD simulation were used to predict the improvement in panel's efficiency using the cooling system. Thus, using the cooling system for the conditions in Egypt was concluded to increase the performance of the panel. Nevertheless, the improvement could still change during the day with changing temperatures and radiation.

At the point of highest radiation, an additional 50 Watt of power could be generated for a 2x1 m^2 panel.

The Tesla turbine was selected for use in the Rankine cycle. A simple Tesla turbine was built and different tests were conducted on the turbine. Moreover, the measured torque from the acceleration method was compared to the typical modeling method of the turbine and the accuracies of each method were determined. The results were used in modeling the turbine in the cycle. Figure 6.1 demonstrates the extra power that can be added to a 2x1 m^2 PV panel using a cooling and power system:

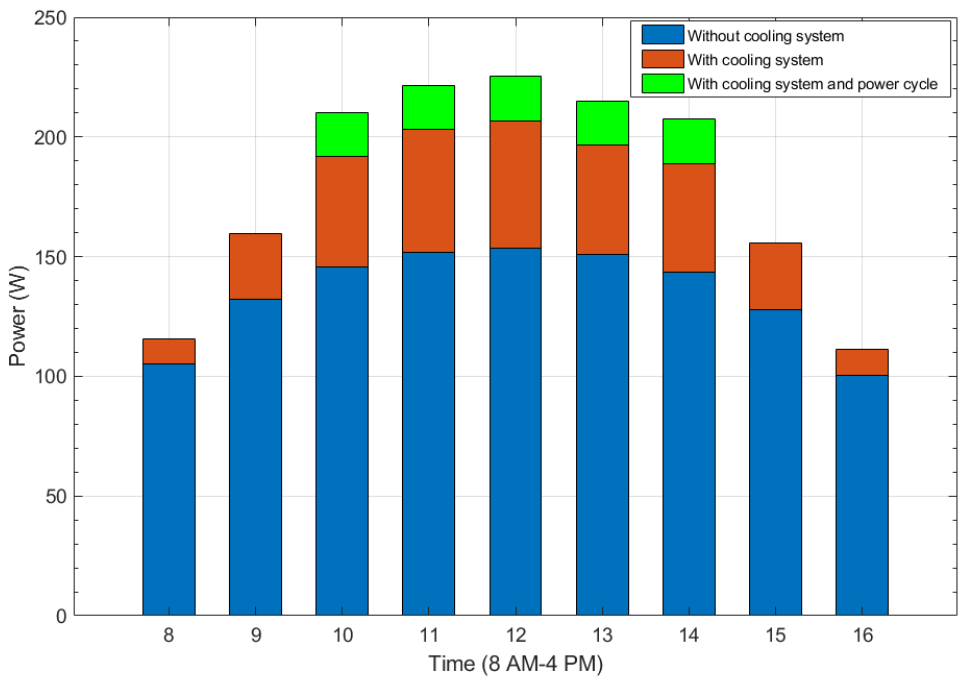

Figure 6.1. Comparison of the improvements in power generation in one panel from different methods

From Figure 6.1, the power cycle can add more power to the system only from 10:00 to 14:00 hours. This is explained by the fact that the solar radiation is sufficiently high at

these times to increase the temperature of the working fluid to the desired temperature. For example, at 12:00 hours, 153 Watts of power can be generated from one panel. By using a cooling system, since the temperature will drop, the efficiency of the panel will increase, and an extra 53 Watts of power can be retrieved from the panel. By adding a generator and completing the power cycle, an additional 18.4 Watts of power can be added to the system (equal to a 12% improvement).

6.1 Limitations and Future Directions

As discussed in Chapter 4, the algorithm that was developed to design the cooling system had an acceptable accuracy, though it could still be more accurate if a two-phase flow analysis was added to it. The following steps are recommended to modify the algorithm:

- Conduct an experiment with boiling R-245-fa in the copper tube to find out the different boiling regions, such as sub-cooled flow boiling, saturated flow boiling (including bubbly, slug, annular, and mist phases).
- Conduct an experiment with boiling R-245-fa in a tilted copper tube to find out the $G_{s,f}$ (surface-liquid combination factor).

By determining the transitions in the flow regime and finding $G_{s,f}$, other correlations [61] can be used to determine the convective heat transfer coefficient. Further, an experiment can be conducted with the real solar panel and cooling tubes to check the accuracy of the analytical and CFD simulations.

Currently, the algorithm mentioned in this thesis is based on having straight tubes for cooling. Other configurations (i.e., serpentine cooling tubes) could also be used for cooling

the panels, which would obviously increase the pressure drop along the tubes while keeping the temperature more uniform, in comparison to the straight configuration.

In this research, a Tesla turbine was built and tested, and its performance were accurately determined. To analyze the cycle more accurately and evaluate the performance of the Tesla turbine, other experiments with higher flowrates could be conducted on a complete test set-up to determine the effect of fluctuating flow, caused by fluctuations in solar radiation.

Bibliography

[1] H. Tyagi, A. K. Agarwal, P. R. Chakraborty, and S. Powar, *Applications of solar energy.* .

[2] N. Kannan and D. Vakeesan, "Solar energy for future world: - A review," *Renew. Sustain. Energy Rev.*, vol. 62, pp. 1092–1105, 2016.

[3] Solargis, "solar resource maps and GIS data for 180+ countries." [Online]. Available: https://solargis.com/maps-and-gis-data/download/world/.

[4] IEA, "Energy Technology Perspectives 2017," p. 443, 2017.

[5] R. M. Swanson, "Developments in Silicon Solar Cells," *2007 IEEE Int. Electron Devices Meet.*, pp. 359–362, 2007.

[6] G. N. Tiwari, R. K. Mishra, and S. C. Solanki, "Photovoltaic modules and their applications: A review on thermal modelling," *Appl. Energy*, vol. 88, no. 7, pp. 2287–2304, 2011.

[7] E. Radziemska, "The effect of temperature on the power drop in crystalline silicon solar cells," *Renew. Energy*, vol. 28, no. 1, pp. 1–12, 2003.

[8] H. M. S. Bahaidarah, A. A. B. Baloch, and P. Gandhidasan, "Uniform cooling of photovoltaic panels: A review," *Renew. Sustain. Energy Rev.*, vol. 57, pp. 1520–1544, 2016.

[9] PVeducation, Available:https://pveducation.org/pvcdrom/solar-cell-operation/effect-of-temperature

[10] G. N. Tiwari and Swapnil Dubey, G. N. Tiwari, and D. Swapnil, "Fundamentals of Photovoltaic Modules and their Applications," p. 423, 2010.

[11] A. Royne, C. J. Dey, and D. R. Mills, "Cooling of photovoltaic cells under concentrated illumination: A critical review," *Sol. Energy Mater. Sol. Cells*, vol. 86, no. 4, pp. 451–483, 2005.

[12] J. R. Edenburn, M. W., & Burns, "Shading analysis of a photovoltaic-cell string illuminated by a parabolic-trough concentrator," 1982.

[13] H. Baig, K. C. Heasman, and T. K. Mallick, "Non-uniform illumination in concentrating solar cells," *Renew. Sustain. Energy Rev.*, vol. 16, no. 8, pp. 5890–5909, 2012.

[14] B. Xiao and A. Faghri, "A three-dimensional thermal-fluid analysis of flat heat pipes," *Int. J. Heat Mass Transf.*, vol. 51, no. 11–12, pp. 3113–3126, 2008.

[15] Y. Xuan, Y. Hong, and Q. Li, "Investigation on transient behaviors of flat plate heat pipes," *Exp. Therm. Fluid Sci.*, vol. 28, no. 2–3, pp. 249–255, 2004.

[16] A. Akbarzadeh and T. Wadowski, "Heat pipe-based cooling systems for photovoltaic cells under concentrated solar radiation," *Appl. Therm. Eng.*, vol. 16, no. 1, pp. 81–87, 1996.

[17] C. R. Russell, "Optical concentrator and cooling system for photovoltaic cells," Patent 4,052,228, 1976.

[18] L. Liu, L. Zhu, Y. Wang, Q. Huang, Y. Sun, and Z. Yin, "Heat dissipation

performance of silicon solar cells by direct dielectric liquid immersion under intensified illuminations," *Sol. Energy*, vol. 85, no. 5, pp. 922–930, 2011.

[19] X. Han, Y. Wang, and L. Zhu, "Electrical and thermal performance of silicon concentrator solar cells immersed in dielectric liquids," *Appl. Energy*, vol. 88, no. 12, pp. 4481–4489, 2011.

[20] H. Xiang, Y. Wang, L. Zhu, X. Han, Y. Sun, and Z. Zhao, "3D numerical simulation on heat transfer performance of a cylindrical liquid immersion solar receiver," *Energy Convers. Manag.*, vol. 64, pp. 97–105, 2012.

[21] J. L. Xu, Y. H. Gan, D. C. Zhang, and X. H. Li, "Microscale heat transfer enhancement using thermal boundary layer redeveloping concept," *Int. J. Heat Mass Transf.*, vol. 48, no. 9, pp. 1662–1674, 2005.

[22] Y. Wang and G.-F. Ding, "Experimental investigation of heat transfer performance for a novel microchannel heat sink," *J. Micromechanics Microengineering*, vol. 18, no. 3, p. 35021, 2008.

[23] S. Agrawal and G. N. Tiwari, "Energy and exergy analysis of hybrid micro-channel photovoltaic thermal module," *Sol. Energy*, vol. 85, no. 2, pp. 356–370, 2011.

[24] R. Kumar and M. A. Rosen, "A critical review of photovoltaic-thermal solar collectors for air heating," *Appl. Energy*, vol. 88, no. 11, pp. 3603–3614, 2011.

[25] S. Nižetić, F. Grubišić- Čabo, I. Marinić-Kragić, and A. M. Papadopoulos, "Experimental and numerical investigation of a backside convective cooling

mechanism on photovoltaic panels," *Energy*, vol. 111, pp. 211–225, 2016.

[26] M. De Rosa, G. Romano, C. Rossi, F. Scarpa, and L. A. Tagliafico, "Dynamic thermal model for hybrid photovoltaic panels," *Energy Procedia*, vol. 81, pp. 345–353, 2015.

[27] C. Rossi, L. A. Tagliafico, F. Scarpa, and V. Bianco, "Experimental and numerical results from hybrid retrofitted photovoltaic panels," *Energy Convers. Manag.*, vol. 76, pp. 634–644, 2013.

[28] H. A. Hussein, A. H. Numan, and R. A. Abdulrahman, "Impproving the Hybrid Photovoltaic/ Thermal System Performance Using Water Cooling Technique and (Zn -H 2 O) Nanofluid," *Int. J. Photoenergy*, vol. 2017, no. 3, pp. 1–14, 2017.

[29] J. Freeman, K. Hellgardt, and C. N. Markides, "An assessment of solar-powered organic Rankine cycle systems for combined heating and power in UK domestic applications," *Appl. Energy*, vol. 138, pp. 605–620, 2015.

[30] Y. A. Cengel and M. A. Boles, *Thermodynamics: an engineering approach*, 7th ed. New York: McGraw-Hill, 2011.

[31] A. Groniewsky, G. Györke, and A. R. Imre, "Description of wet-to-dry transition in model ORC working fluids," *Appl. Therm. Eng.*, vol. 125, pp. 963–971, 2017.

[32] H. Chen, D. Y. Goswami, and E. K. Stefanakos, "A review of thermodynamic cycles and working fluids for the conversion of low-grade heat," *Renew. Sustain. Energy Rev.*, vol. 14, no. 9, pp. 3059–3067, 2010.

[33] Convertenergy, “Technical Specifications,” Canterbury, 2013.

[34] J. A. Duffie and W. A. Beckman, “Solar Engineering of Thermal Processes Solar Engineering,” p. 936, 2013.

[35] K. G. T. Hollands, T. E. Unny, G. D. Raithby, and L. Konicek, “Free Convective Heat Transfer Across Inclined Air Layers,” *J. Heat Transfer*, vol. 98, no. 2, p. 189, 1976.

[36] T. L. Bergman and A. S. Lavine, “Fundamentals of Heat and Mass Transfer,” 8th ed., John Wiley&Sons, Inc., 2017, pp. 476–494.

[37] H. D. Baehr; and K. Stephan, “Heat and Mass Transfer : Heat and Mass Transfer,” *Chem. age India*, vol. 30, no. 9, pp. 809–818, 1979.

[38] G. K. Batchelor, “Note On a Classic of Solutions of The Navier-Stokes Equations Representing Steady Rotationally-Symmetric Flow,” *Quart. Journ. Mech. Appl. Math.*, vol. IV, no. July 1950, 1951.

[39] H. Z. Hassan, “Performance evaluation of a continuous operation adsorption chiller powered by solar energy using silica gel and water as the working pair,” *Energies*, vol. 7, no. 10, pp. 6382–6400, 2014.

[40] S. J. Williamson, B. H. Stark, and J. D. Booker, “Low head pico hydro turbine selection using a multi-criteria analysis,” *Renew. Energy*, vol. 61, pp. 43–50, 2014.

[41] N. Tesla, “» N. Tesla.,” CA135174A, 1913.

[42] A. C. Hindmarsh, “Lawrence Livermore Laboratory,” *Energy*, no. February, pp. 1–6, 1979.

[43] A. Sun, "Field Fabrication of Solar-Thermal Powered Steam Turbines for Generation of Mechanical Power by," 2006.

[44] P. Lampart, K. Kosowski, M. Piwowarski, and L. Jędrzejewski, "Design analysis of Tesla micro-turbine operating on a low-boiling medium," *Polish Marit. Res.*, vol. 16, no. Special, pp. 28–33, 2009.

[45] V. G. Krishnan, "Design and Fabrication of cm-scale Tesla Turbines," 2015.

[46] K. Stewartson, "On the flow between two rotating coaxial discs," *Proc. Camb. Philol. Soc.*, vol. 49, no. July 1952, pp. 333–341, 1953.

[47] W. Rice, "An Analytical and Experimental Investigation of Multiple-Disk Turbines," *J. Eng. Power*, pp. 1–8, 1965.

[48] E. W. Beans, "Friction Turbine," *Solutions*, vol. 3, no. 1, pp. 131–134, 1966.

[49] B. E. Boyack and W. Rice, "Integral Method for Flow Between Corotating Disks," *J. Basic Eng.*, vol. 93, no. 3, p. 350, 1971.

[50] P. W. Garrison, D. W. Harvey, and I. Catton, "Laminar Compressible Flow Between Rotating Disks," *J. Fluids Eng.*, vol. 98, no. 2, pp. 382–389, 1976.

[51] M. Podergajs, "The Tesla Turbine Revisited," *Univ. Ljubljana*, pp. 1–15, 2011.

[52] S. Sengupta and A. Guha, "A theory of Tesla disc turbines," *Proc. Inst. Mech. Eng. Part A J. Power Energy*, vol. 226, no. 5, pp. 650–663, 2012.

[53] V. P. Carey, "Assessment of Tesla Turbine Performance for Small Scale Rankine

Combined Heat and Power Systems," *J. Eng. Gas Turbines Power*, vol. 132, no. 12, p. 122301, 2010.

[54] P. Lampart and Ł. Jędrzejewski, "Investigations of Aerodynamics of Tesla Bladeless Microturbines," *J. Theor. Appl. Mech.*, vol. 49, no. 2, pp. 477–499, 2011.

[55] C. Schosser, S. Lecheler, and M. Pfitzner, "Analytical and numerical solutions of the rotor flow in tesla turbines," *Period. Polytech. Mech. Eng.*, vol. 61, no. 1, pp. 12–22, 2017.

[56] G. P. Hoya and A. Guha, "The design of a test rig and study of the performance and efficiency of a Tesla disc turbine," *Proc. Inst. Mech. Eng. Part A J. Power Energy*, vol. 223, no. 4, pp. 451–465, 2009.

[57] V. D. Romanin, "Theory and Performance of Tesla Turbines," 2012.

[58] W. Rice, *Handbook of Turbomachinery*. New York, 2003.

[59] D. Nendl, "Dreidimensionale laminare instabilitäten bei ebenen wänden," *Angew. Math. Mech*, vol. 56, pp. 211–213, 1973.

[60] E. Lemma, R. T. Deam, D. Toncich, and R. Collins, "Characterisation of a small viscous flow turbine," *Exp. Therm. Fluid Sci.*, vol. 33, no. 1, pp. 96–105, 2008.

[61] S. G. Kandlikar, "Handbook of phase change: Boiling and condensation," Philadelphia, PA: Taylor & Francis., 1999.

[62] J. P. Holman and W. J. Gajda, *Experimental methods for engineers*, 4th ed. New York: McGraw-Hill, 1984.

Appendices

Appendix A (Uncertainty Analysis for Torque Measurements)

To determine the uncertainty associated with the torque measurement, we first need to determine the uncertainty of angle measurements by an encoder, which is said to be $0.0038\ [rad]$ by the company. Moreover, the rotational speed can be calculated from the following equation:

$$\Omega = \frac{\Delta\theta}{\Delta t} \tag{1}$$

where Ω is angular rotational speed, $\Delta\theta$ is angular displacement, and Δt is time interval. Therefore, the uncertainty for angular velocity is [62]:

$$\mathbf{U}_{\Omega} = \sqrt{\left(\frac{\mathbf{U}_{\Delta\theta}}{\Delta t}\right)^2 + \left(-\frac{\Delta\theta}{\Delta t^2}\mathbf{U}_{\Delta \mathrm{t}}\right)^2} \tag{2}$$

where $U_{\Delta\theta}$ is the uncertainty for angular displacement and can be calculated from the uncertainty of angle measurement and $U_{\Delta \mathrm{t}}$ is uncertainty associated with time measurement, which can be determined by calculating the variation of time intervals. The above equation may be rewritten in the following form:

$$\mathbf{U}_{\Omega} = \sqrt{\left(\frac{\sqrt{2}\mathbf{U}_{\theta}}{\Delta t}\right)^2 + \left(-\frac{\Omega}{\Delta \mathrm{t}}\mathbf{U}_{\Delta \mathrm{t}}\right)^2} \tag{3}$$

In addition, to calculate the torque, we can use following equation:

$$T = I \times \alpha \tag{4}$$

So, the uncertainty associated with the torque measurement will be:

$$\mathbf{U}_T = \sqrt{(\mathbf{U}_I \alpha)^2 + (\mathbf{U}_\alpha I)^2} \tag{5}$$

Assuming that the moment of inertia is calculated using CAD software, we can neglect the uncertainty for this parameter, so the above equation may be simplified to the following

$$\mathbf{U}_T = |\mathbf{U}_\alpha I| \tag{6}$$

In order to calculate the uncertainty of angular acceleration, we can use the following equation

$$\alpha = \frac{\Delta\Omega}{\Delta t} \tag{7}$$

So, the final equation for the uncertainty of angular acceleration would be:

$$\mathbf{U}_\alpha = \sqrt{\left(\frac{\sqrt{2}\mathbf{U}_\Omega}{\Delta t}\right)^2 + \left(-\frac{\alpha}{\Delta \mathrm{t}}\mathbf{U}_{\Delta \mathrm{t}}\right)^2} \tag{8}$$

Now, with the experimental data, we can calculate the uncertainty associated with the torque measurement by combining Eqs. (3) and (8).

Appendix B (The COMSOL® application)

As mentioned before, to make it easy for others to determine the temperature of the fluid and the surface of the PV panel without setting up the software, an application is built into the COMSOL Multiphysics. Figure B.1 shows the application and its different parts:

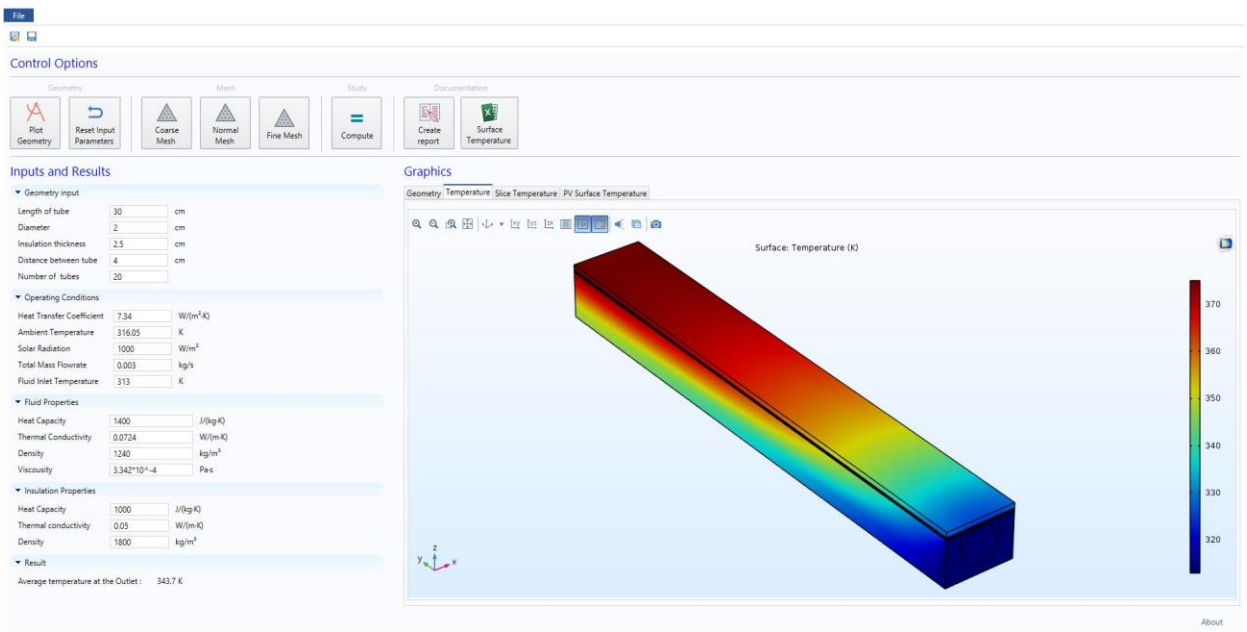

Figure B.1. View of the software interface

The main application consists of three important parts:

- Control Options
- Inputs and Results
- Graphics

B.1 Control Options

This section helps the user run the simulation. It is comprised of different buttons as shown in Figure B.2:

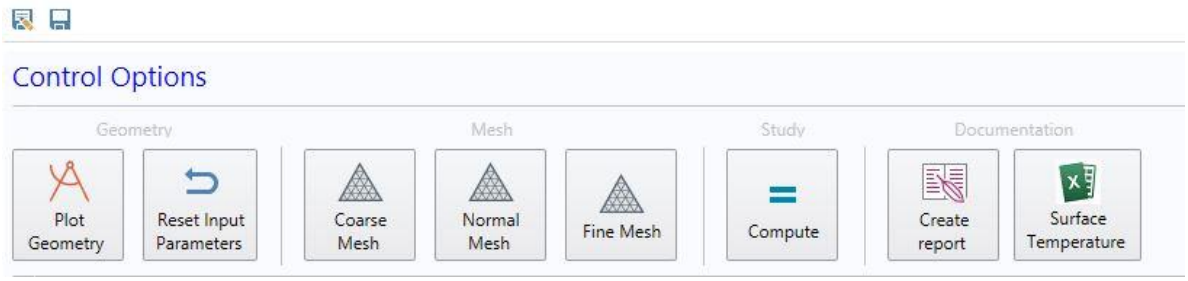

Figure B.2. View of the control option bar of the software

- **Plot Geometry**: This button updates the geometry.
- **Reset Input Parameters**: This button changes all parameters to their original value.
- **Coarse/Normal/Fine Mesh**: This button generates mesh with different quality. Originally, it is clear, and by choosing a coarse mesh, the size of the mesh is increased and the accuracy of the CFD results may decrease.
- **Compute**: To start the simulation, you click on this button.
- **Create Report**: This button will generate a Word file with all of the details of the simulation (i.e., parameters, activated studies, mesh, etc.).
- **Surface Temperature**: This button will generate an Excel file from the surface temperature of the PV panel.

B.2 Inputs and Results

This section includes all of the parameters for the working fluid, insulation, and tubes that can be controlled by the user as shown in Figure B.3:

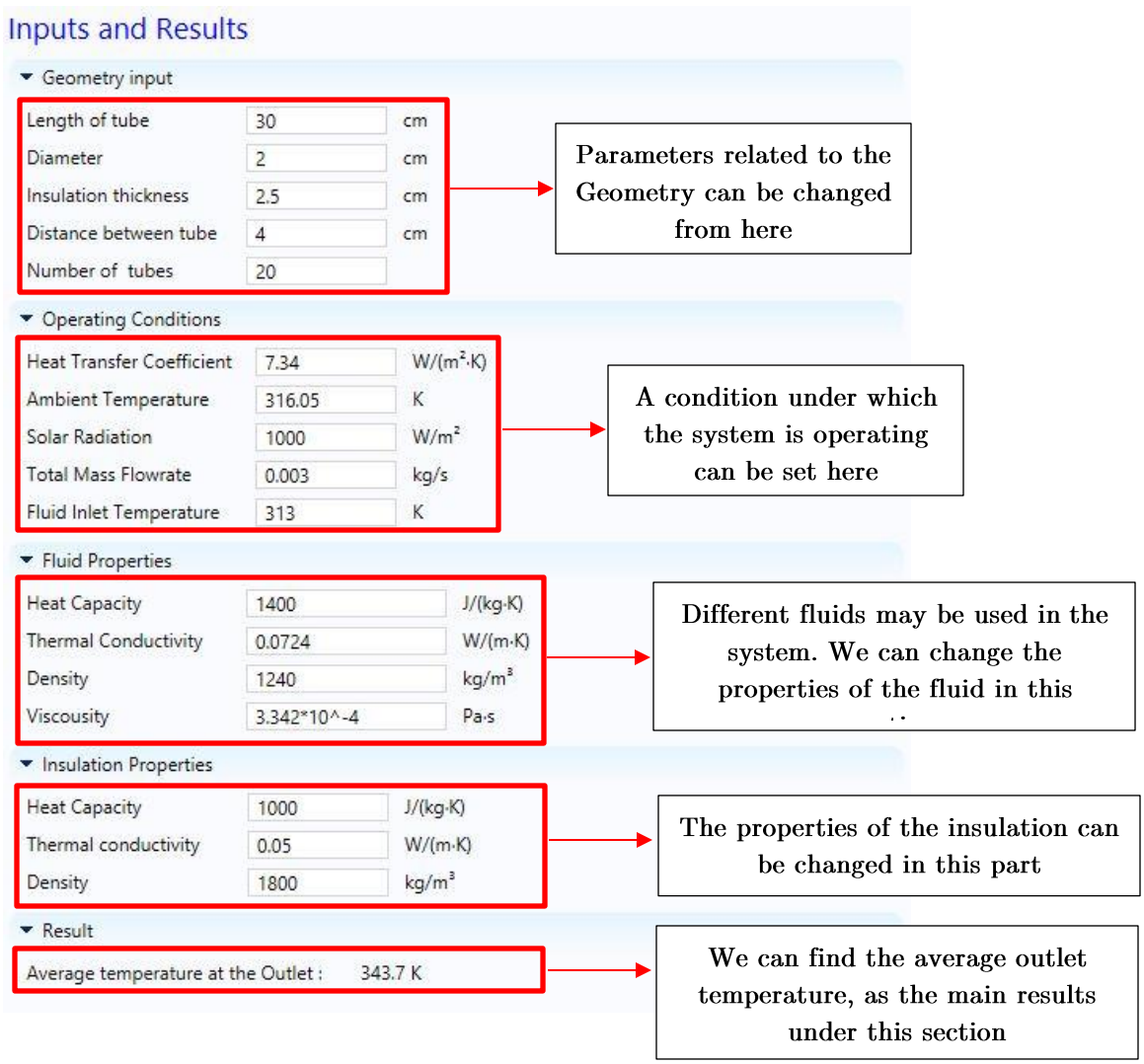

Figure B.3. View of the inputs and results sections of the software

B.3 Graphics

This part consists of four sections:

- **Geometry**: This tab shows the updated geometry and a view of the generated mesh.

- **Temperature**: When the simulation is done, the temperature profile of the tube and the insulation can be found under this tab.

- **Slice Temperature**: In this tab, five section views of the temperature profile are provided. This tab helps the user determine how the temperature profile of the fluid is changing as it flows through the tube.

- **PV Surface Temperature**: To determine the efficiency of the PV panel, it is necessary to have the surface temperature of the panel. In this tab, a 2-D graph of the surface temperature will be plotted.

A view of each tab is shown in Figures B.4 to B.7:

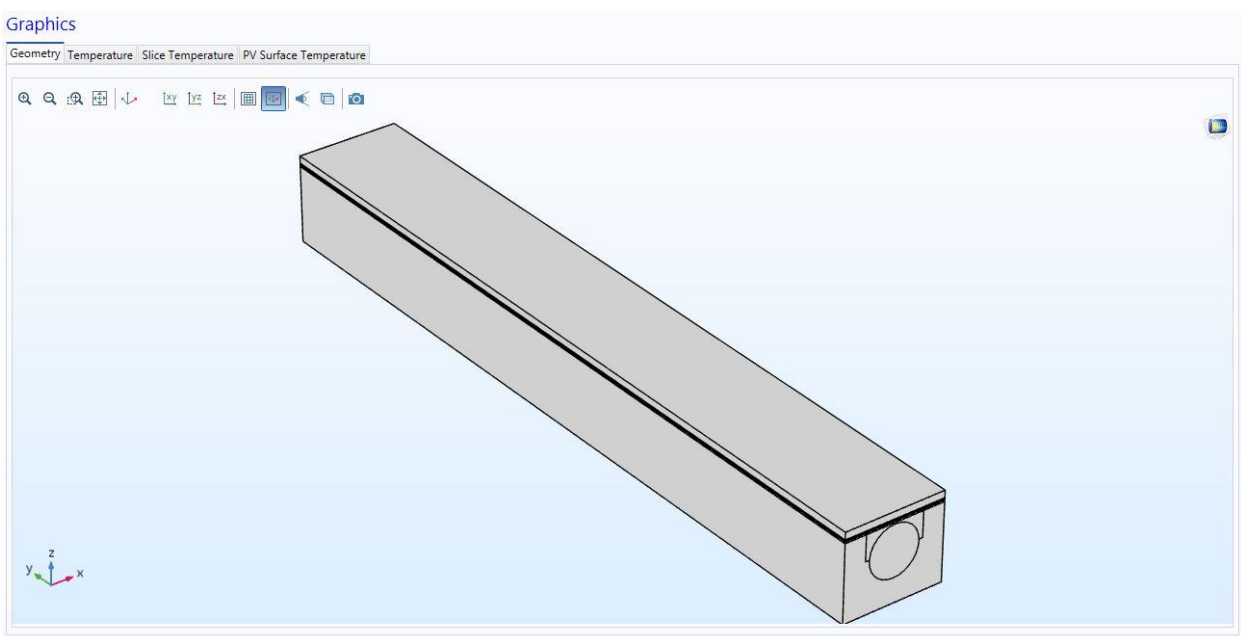

Figure B.4. Geometry tab in the graphics section of the software

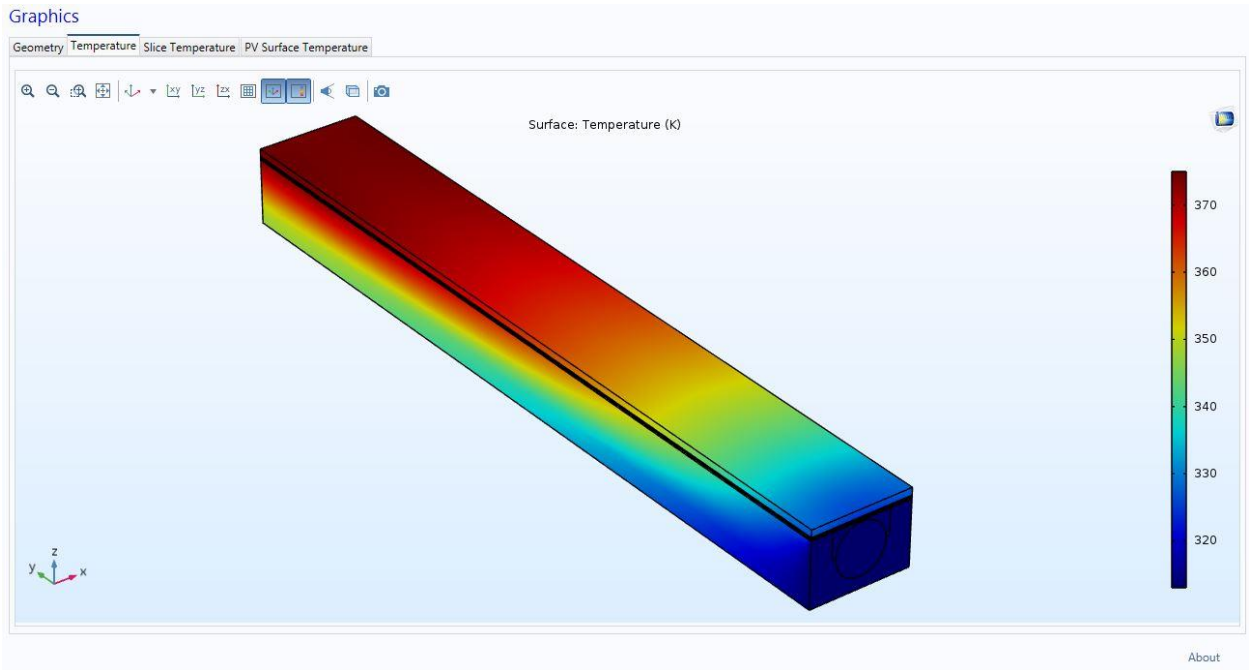

Figure B.5. Temperature tab in the graphics section of the software

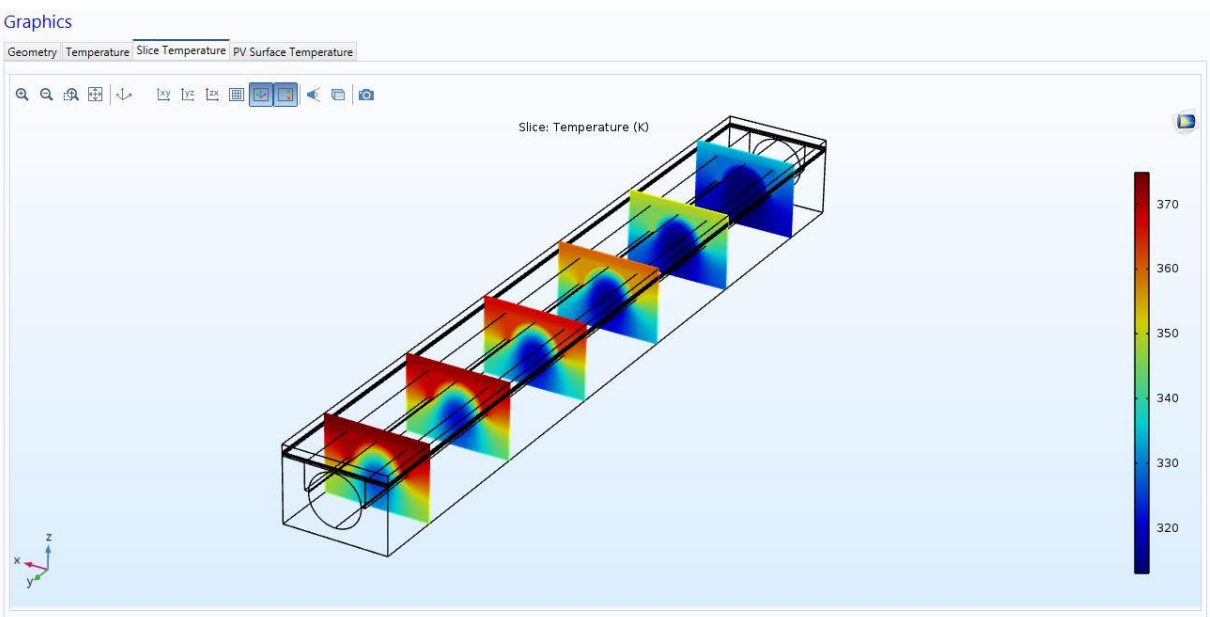

Figure B.6. Slice temperature tab in the graphics section of the software

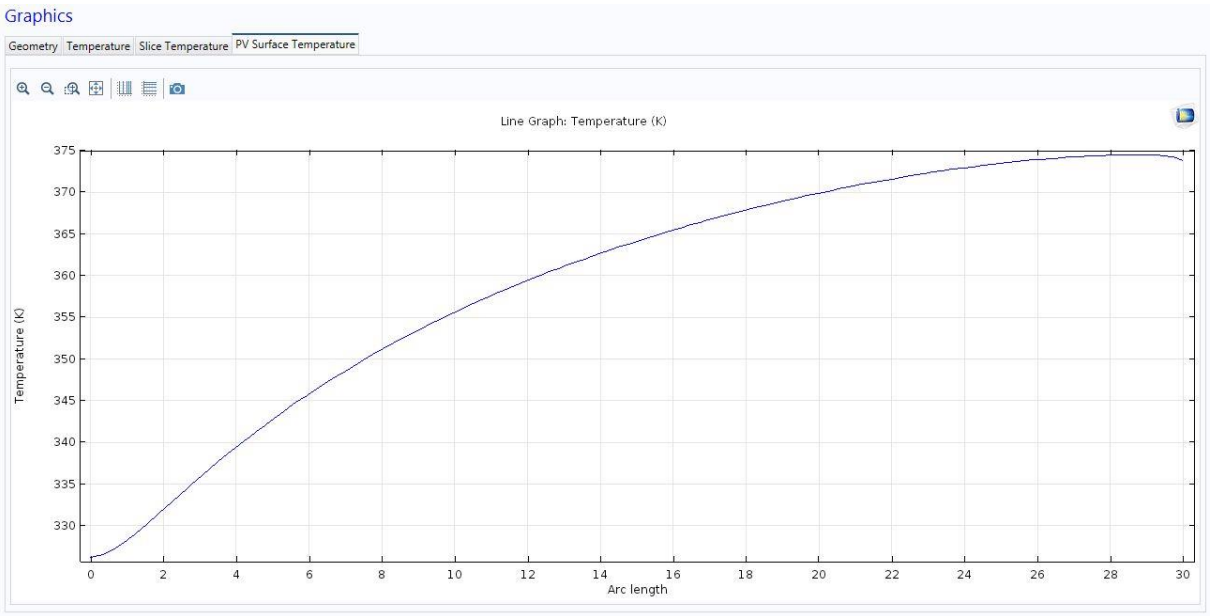

Figure B.7. Surface temperature tab in the graphics section of the software

Appendix C (Working fluids properties in the cycle)

As it was discussed in Chapter 3, different working fluids have been chosen to be analyzed for the cycle. For these working fluids, complete thermodynamic analysis of the cycle was done and the properties of the fluids in different working points were determined.

- Water

$T_c = 647.1$ [K] , $T_{Max} = 120$ [°C] , $P_{Max} = 198.5$ [kPa] , $T_{condenser} = 40$ [°C] , $P_{condenser} = 7.38$ [kPa]													
P_{23}[kPa]	T_{23-sat}[°C]	T_{max}[°C]	$\mathbf{h}_3 \left[\frac{kj}{kg}\right]$	$s_3 \left[\frac{kJ}{kg\ K}\right]$	$\mathbf{h}_4 \left[\frac{kj}{kg}\right]$	$\mathbf{h}_{4a} \left[\frac{kj}{kg}\right]$	$\mathbf{h}_1 \left[\frac{kj}{kg}\right]$	$s_1 \left[\frac{kJ}{kg\ K}\right]$	$s_2 \left[\frac{kJ}{kg\ K}\right]$	$\mathbf{h}_2 \left[\frac{kj}{kg}\right]$	$\Delta\mathbf{h}_{turbine} \left[\frac{kj}{kg}\right]$	$\dot{m} \left[\frac{kg}{s}\right]$	$Q_h[kW]$
120	104.8	120	2714	7.378	2299	2506.5	167	0.5723	0.5723	167.6	207.5	0.00024	0.6136
130	107.1	120	2713	7.339	2287	2500	167	0.5723	0.5723	167.6	213	0.00023	0.5975
140	109.3	120	2712	7.303	2275	2493.5	167	0.5723	0.5723	167.6	218.5	0.00023	0.5822
150	111.4	120	2711	7.269	2265	2488	167	0.5723	0.5723	167.6	223	0.00022	0.5703
160	113.3	120	2710	7.237	2255	2482.5	167	0.5723	0.5723	167.7	227.5	0.00022	0.5587
170	115.2	120	2709	7.207	2245	2477	167	0.5723	0.5723	167.7	232	0.00022	0.5477
180	116.9	120	2708	7.179	2236	2472	167	0.5723	0.5723	167.7	236	0.00021	0.5382
190	118.6	120	2707	7.152	2228	2467.5	167	0.5723	0.5723	167.7	239.5	0.00021	0.5301

- R-245-fa

$T_c = 427.2$[K] , $T_{Max} = 120$ [°C] , $P_{Max} = 1929$ [kPa] , $T_{condenser} = 40$ [°C] , $P_{condenser} = 249.6$ [kPa]													
P_{23}[kPa]	T_{23-sat}[°C]	T_{max}[°C]	$\mathbf{h}_3 \left[\frac{kj}{kg}\right]$	$s_3 \left[\frac{kJ}{kg\ K}\right]$	$\mathbf{h}_4 \left[\frac{kj}{kg}\right]$	$\mathbf{h}_{4a} \left[\frac{kj}{kg}\right]$	$\mathbf{h}_1 \left[\frac{kj}{kg}\right]$	$s_1 \left[\frac{kJ}{kg\ K}\right]$	$s_2 \left[\frac{kJ}{kg\ K}\right]$	$\mathbf{h}_2 \left[\frac{kj}{kg}\right]$	$\Delta\mathbf{h}_{turbine} \left[\frac{kj}{kg}\right]$	$\dot{m} \left[\frac{kg}{s}\right]$	$Q_h[kW]$
400	55.07	120	513.1	1.956	502.3	507.7	252.6	1.179	1.179	252.7	5.4	0.00926	2.4111
600	69.4	120	510.4	1.925	490.9	500.65	252.6	1.179	1.179	252.8	9.75	0.00513	1.3210
800	80.46	120	507.5	1.902	482.3	494.9	252.6	1.179	1.179	253	12.6	0.00397	1.0099
1000	89.61	120	504.5	1.882	475.1	489.8	252.6	1.179	1.179	253.1	14.7	0.00340	0.8551
1200	97.5	120	501.1	1.864	468.8	484.95	252.6	1.179	1.179	253.3	16.15	0.00310	0.7672
1400	104.5	120	497.3	1.847	462.8	480.05	252.6	1.179	1.179	253.5	17.25	0.00290	0.7067
1600	110.8	120	493.1	1.829	457	475.05	252.6	1.179	1.179	253.6	18.05	0.00277	0.6634
1800	116.5	120	488.1	1.812	451	469.55	252.6	1.179	1.179	253.8	18.55	0.00270	0.6315

- R-134-a

$T_c = 374.21$[K] , $T_{Max} = 95$ [°C] , $P_{Max} = 3594$ [kPa] , $T_{condenser} = 40$ [°C] , $P_{condenser} = 1017$ [kPa]													
P_{23}[kPa]	T_{23-sat}[°C]	T_{max}[°C]	$\mathbf{h}_3 \left[\frac{kj}{kg}\right]$	$s_3 \left[\frac{kJ}{kg\ K}\right]$	$\mathbf{h}_4 \left[\frac{kj}{kg}\right]$	$\mathbf{h}_{4a} \left[\frac{kj}{kg}\right]$	$\mathbf{h}_1 \left[\frac{kj}{kg}\right]$	$s_1 \left[\frac{kJ}{kg\ K}\right]$	$s_2 \left[\frac{kJ}{kg\ K}\right]$	$\mathbf{h}_2 \left[\frac{kj}{kg}\right]$	$\Delta\mathbf{h}_{turbine} \left[\frac{kj}{kg}\right]$	$\dot{m} \left[\frac{kg}{s}\right]$	$Q_h[kW]$
400	8.91	Temperature of the high-pressure line is less than the temperature of the condenser											
600	21.55												
800	31.31												
1000	39.37												
1200	46.29	95	327.4	1.069	323	325.2	108.3	0.3949	0.3949	108.4	2.2	0.02273	4.9773
1400	52.4	95	324.8	1.051	316.6	320.7	108.3	0.3949	0.3949	108.6	4.1	0.01220	2.6366
1600	57.88	95	322.2	1.035	310.8	316.5	108.3	0.3949	0.3949	108.8	5.7	0.00877	1.8719
1800	62.87	95	319.3	1.019	305.4	312.35	108.3	0.3949	0.3949	108.9	6.95	0.00719	1.5137
2000	67.45	95	316.3	1.004	300.3	308.3	108.3	0.3949	0.3949	109.1	8	0.00625	1.2950

- R-600

$T_c = 425.13$[K] , $T_{Max} = 120$ [°C] , $P_{Max} = 2212$ [kPa] , $T_{condenser} = 40$ [°C] , $P_{condenser} = 379.2$ [kPa]													
P_{23}[kPa]	T_{23-sat}[°C]	T_{max}[°C]	$\mathbf{h}_3 \left[\frac{kj}{kg}\right]$	$s_3 \left[\frac{kJ}{kg\ K}\right]$	$\mathbf{h}_4 \left[\frac{kj}{kg}\right]$	$\mathbf{h}_{4a} \left[\frac{kj}{kg}\right]$	$\mathbf{h}_1 \left[\frac{kj}{kg}\right]$	$s_1 \left[\frac{kJ}{kg\ K}\right]$	$s_2 \left[\frac{kJ}{kg\ K}\right]$	$\mathbf{h}_2 \left[\frac{kj}{kg}\right]$	$\Delta\mathbf{h}_{turbine} \left[\frac{kj}{kg}\right]$	$\dot{m} \left[\frac{kg}{s}\right]$	$Q_h[kW]$
600	57.43	120	798.6	2.815	774.8	786.7	296.5	1.328	1.328	296.9	11.9	0.00420	2.1080
800	69.45	120	793.5	2.764	755.8	774.65	296.5	1.328	1.328	297.2	18.85	0.00265	1.3164
1000	79.42	120	788	2.722	740.4	764.2	296.5	1.328	1.328	297.6	23.8	0.00210	1.0303
1200	88.01	120	782.2	2.685	727	754.6	296.5	1.328	1.328	297.9	27.6	0.00181	0.8774
1400	95.61	120	775.9	2.651	714.9	745.4	296.5	1.328	1.328	298.3	30.5	0.00164	0.7830
1600	102.4	120	769	2.618	703.5	736.25	296.5	1.328	1.328	298.7	32.75	0.00153	0.7180
1800	108.7	120	761.2	2.585	692.4	726.8	296.5	1.328	1.328	299	34.4	0.00145	0.6718
2000	114.4	120	752.3	2.552	681.1	716.7	296.5	1.328	1.328	299.4	35.6	0.00140	0.6361

- R-22

$T_c = 369.30$[K] , $T_{Max} = 85$ [°C] , $P_{Max} = 4037$ [kPa] , $T_{condenser} = 40$ [°C] , $P_{condenser} = 1534$ [kPa]													
P_{23}[kPa]	T_{23-sat}[°C]	T_{max}[°C]	$\mathbf{h}_3 \left[\frac{kj}{kg}\right]$	$s_3 \left[\frac{kJ}{kg\ K}\right]$	$\mathbf{h}_4 \left[\frac{kj}{kg}\right]$	$\mathbf{h}_{4a} \left[\frac{kj}{kg}\right]$	$\mathbf{h}_1 \left[\frac{kj}{kg}\right]$	$s_1 \left[\frac{kJ}{kg\ K}\right]$	$s_2 \left[\frac{kJ}{kg\ K}\right]$	$\mathbf{h}_2 \left[\frac{kj}{kg}\right]$	$\Delta\mathbf{h}_{turbine} \left[\frac{kj}{kg}\right]$	$\dot{m} \left[\frac{kg}{s}\right]$	$Q_h[kW]$
1800	46.69	85	453.2	1.796	448.6	450.9	249.8	1.167	1.167	250	2.3	0.02174	4.4174
2000	51.26	85	450.7	1.781	443.2	446.95	249.8	1.167	1.167	250.2	3.75	0.01333	2.6733
2200	55.5	85	448.1	1.766	438.2	443.15	249.8	1.167	1.167	250.4	4.95	0.01010	1.9970
2400	59.46	85	445.3	1.752	433.4	439.35	249.8	1.167	1.167	250.6	5.95	0.00840	1.6361
2600	63.19	85	442.4	1.738	428.8	435.6	249.8	1.167	1.167	250.7	6.8	0.00735	1.4096
2800	66.71	85	439.3	1.724	424.3	431.8	249.8	1.167	1.167	250.9	7.5	0.00667	1.2560
3000	70.04	85	435.9	1.709	419.7	427.8	249.8	1.167	1.167	251.1	8.1	0.00617	1.1407
3200	73.21	85	432.2	1.695	415.1	423.65	249.8	1.167	1.167	251.3	8.55	0.00585	1.0579

- Ethanol

$T_c = 513.8$[K] , $T_{Max} = 120$ [°C] , $P_{Max} = 428.6$ [kPa] , $T_{condenser} = 40$ [°C] , $P_{condenser} = 17.89$ [kPa]													
P_{23}[kPa]	T_{23-sat}[°C]	T_{max}[°C]	$\mathbf{h}_3 \left[\frac{kj}{kg}\right]$	$s_3 \left[\frac{kJ}{kg\ K}\right]$	$\mathbf{h}_4 \left[\frac{kj}{kg}\right]$	$\mathbf{h}_{4a} \left[\frac{kj}{kg}\right]$	$\mathbf{h}_1 \left[\frac{kj}{kg}\right]$	$s_1 \left[\frac{kJ}{kg\ K}\right]$	$s_2 \left[\frac{kJ}{kg\ K}\right]$	$\mathbf{h}_2 \left[\frac{kj}{kg}\right]$	$\Delta\mathbf{h}_{turbine} \left[\frac{kj}{kg}\right]$	$\dot{m} \left[\frac{kg}{s}\right]$	$Q_h[kW]$
50	61.42	120	1188	3.789	1119	1153.5	147.7	0.6971	0.6971	147.7	34.5	0.00145	1.5077
100	77.94	120	1185	3.658	1075	1130	147.7	0.6971	0.6971	147.8	55	0.00091	0.9429
150	88.54	120	1182	3.578	1050	1116	147.7	0.6971	0.6971	147.9	66	0.00076	0.7834
200	96.54	120	1179	3.521	1031	1105	147.7	0.6971	0.6971	147.9	74	0.00068	0.6967
250	103.1	120	1176	3.474	1017	1096.5	147.7	0.6971	0.6971	148	79.5	0.00063	0.6465
300	108.6	120	1173	3.435	1005	1089	147.7	0.6971	0.6971	148.1	84	0.00060	0.6101
350	113.4	120	1170	3.401	994.1	1082.05	147.7	0.6971	0.6971	152.2	87.95	0.00057	0.5786
400	117.7	120	1167	3.371	984.6	1075.8	147.7	0.6971	0.6971	148.2	91.2	0.00055	0.5586

- R-32

$T_c = 351.26$[K] , $T_{Max} = 70$ [°C] , $P_{Max} = 4877$ [kPa] , $T_{condenser} = 40$ [°C] , $P_{condenser} = 2478$ [kPa]													
P_{23}[kPa]	T_{23-sat}[°C]	T_{max}[°C]	$\mathbf{h}_3 \left[\frac{kj}{kg}\right]$	$s_3 [\frac{kJ}{kg\ K}]$	$\mathbf{h}_4 \left[\frac{kj}{kg}\right]$	$\mathbf{h}_{4a} \left[\frac{kj}{kg}\right]$	$\mathbf{h}_1 \left[\frac{kj}{kg}\right]$	$s_1 [\frac{kJ}{kg\ K}]$	$s_2 [\frac{kJ}{kg\ K}]$	$\mathbf{h}_2 \left[\frac{kj}{kg}\right]$	$\Delta\mathbf{h}_{turbine} \left[\frac{kj}{kg}\right]$	$\dot{m} \left[\frac{kg}{s}\right]$	$Q_h [kW]$
2600	41.98	70	557	2.139	554.9	555.95	275.6	1.252	1.252	275.7	1.05	0.04762	13.3952
2800	45.08	70	552.8	2.117	547.7	550.25	275.6	1.252	1.252	276	2.55	0.01961	5.4275
3000	48.02	70	548.3	2.096	540.6	544.45	275.6	1.252	1.252	276.2	3.85	0.01299	3.5338
3200	50.81	70	543.7	2.075	533.7	538.7	275.6	1.252	1.252	276.4	5	0.01000	2.6730
3400	53.47	70	538.7	2.054	526.8	532.75	275.6	1.252	1.252	276.6	5.95	0.00840	2.2025
3600	56.01	70	533.5	2.032	519.9	526.7	275.6	1.252	1.252	276.9	6.8	0.00735	1.8868
3800	58.44	70	527.8	2.01	512.9	520.35	275.6	1.252	1.252	277.1	7.45	0.00671	1.6826
4000	60.77	70	521.6	1.987	505.7	513.65	275.6	1.252	1.252	277.3	7.95	0.00629	1.5365

- R-152-a

$T_c = 386.41$[K] , $T_{Max} = 100$ [°C] , $P_{Max} = 3511$ [kPa] , $T_{condenser} = 40$ [°C] , $P_{condenser} = 910.3$ [kPa]													
P_{23}[kPa]	T_{23-sat}[°C]	T_{max}[°C]	$\mathbf{h}_3 \left[\frac{kj}{kg}\right]$	$s_3 [\frac{kJ}{kg\ K}]$	$\mathbf{h}_4 \left[\frac{kj}{kg}\right]$	$\mathbf{h}_{4a} \left[\frac{kj}{kg}\right]$	$\mathbf{h}_1 \left[\frac{kj}{kg}\right]$	$s_1 [\frac{kJ}{kg\ K}]$	$s_2 [\frac{kJ}{kg\ K}]$	$\mathbf{h}_2 \left[\frac{kj}{kg}\right]$	$\Delta\mathbf{h}_{turbine} \left[\frac{kj}{kg}\right]$	$\dot{m} \left[\frac{kg}{s}\right]$	$Q_h [kW]$
1200	50.72	100	606.6	2.262	595.2	600.9	271.7	1.242	1.242	272.1	5.7	0.00877	2.9342
1400	57.03	100	602.7	2.234	585.5	594.1	271.7	1.242	1.242	272.3	8.6	0.00581	1.9209
1600	62.7	100	598.7	2.209	576.8	587.75	271.7	1.242	1.242	272.5	10.95	0.00457	1.4895
1800	67.85	100	594.5	2.186	568.7	581.6	271.7	1.242	1.242	272.8	12.9	0.00388	1.2469
2000	72.6	100	590	2.163	561.1	575.55	271.7	1.242	1.242	273	14.45	0.00346	1.0969
2200	76.99	100	585.2	2.141	553.8	569.5	271.7	1.242	1.242	273.2	15.7	0.00318	0.9936
2400	81.1	100	580.1	2.119	546.6	563.35	271.7	1.242	1.242	273.5	16.75	0.00299	0.9152
2600	84.94	100	574.6	2.097	539.5	557.05	271.7	1.242	1.242	273.7	17.55	0.00285	0.8573
2800	88.57	100	568.4	2.074	532.3	550.35	271.7	1.242	1.242	273.9	18.05	0.00277	0.8158